Contact-Based Assembly of Nano-scale Structures:

Synthesis of Mechanics and Tools of Nanomanipulation

BY

CHRISTOPHER ANDREW PELZMANN
B.S., University of Colorado at Boulder, Boulder, Colarado, 2006

THESIS

Submitted as partial fulfillment of the requirements
for the degree of Doctor of Philosophy in Mechanical Engineering
in the Graduate College of the
University of Illinois at Chicago, 2013

Chicago, Illinois

Defense Committee:

Professor Laxman Saggere, Chair and Advisor
Professor Ahmed Shabana
Professor Thomas Royston
Professor Carmen Lilley
Dr. Michael Brown
Professor Michael Stroscio, Electrical and Computer Engineering

This thesis is dedicated to my loving wife and greatest friend, Debbie.

ACKNOWLEDGEMENTS

The support and guidance I have received throughout this journey has been humbling and inspiring. I would like to express my profound gratitude to all of those who have aided me in my pursuit of this work both personally and professionally. First, I would like to thank my wife, Debra. Her intelligence, strength, and balance have been an incredible driving influence in my growth through the past eight and a half years. Over this time I have regained my confidence in myself and greatly expanded the horizons of what I thought possible. She has been especially supportive and patient during my time in graduate studies and for that I will be forever thankful.

Second, I would like to thank my advisor, Professor Laxman Saggere for this incredible opportunity. I had thought little of pursing my education to this level but through his continued support, guidance, and trust I have experienced an inspiring level of intellectual work that will forever shape my professional career. His passion for and deep understanding of the sub-millimeter scale realm has introduced me to an exciting world of possibilities and given me the confidence and tools necessary to continue my exploration of it. I would also like to thank him for his time and patience in teaching me the finer arts of technical writing. I am continually amazed by the clarity and impact of his writing and I only hope to emulate it in my future career. To him I extend my heartfelt gratitude.

I would also like to thank my committee members—Professor Ahmed Shabana, Professor Thomas J. Royston, Professor Carmen Lilley, Professor Michael Brown, and Professor Michael Strosico—for their time both in and out of class, their advice, and their support.

Third, I would like to thank all of my friends, classmates and labmates who have given life to my graduate experience at UIC. Within the Microsystems and Devices Lab, I would like to thank Dr. Sandeep Krishnan, Brian Kunzer, Marina Domokhovsky, Shushi Kabu, Sasidar Madugula, and Bhava

Chakka. To Sandeep I owe a special debt of gratitude for encouraging my growth in engineering, science and philosophy. Likewise, I would like to thank Brian and Sasi for their limitless enthusiasm and passion for debate. Outside of the lab I would like to thank Harish Kanchi, Jon Komperda, and Ian Gould for their friendship, countless coffee breaks, and lively discussions.

Fourth, I would like to thank my mentor through the American Society of Mechanical Engineers, Joel Leifer. His personal and professional wisdom and advice have helped me mature as a student and prepare me for my career.

Fifth, I would like to thank my family for their constant encouragement and support. They are the foundation on which I began my pursuit of science and engineering and have remained an immense source of inspiration.

Finally, I would like to thank the National Science Foundation (NSF) for financially supporting this work through the Nanomanufacturing Program, Grant Number 0800741.

Table of Contents

List of Figures

List of Tables

1 INTRODUCTION

Construction of new useful nanoscopic structures and mechanisms—such as nano-electromechanical systems (NEMS)—requires advanced nano-fabrication tools and techniques. Emerging NEMS devices potentially involve complex, asymmetric, three-dimensional arrangements of nano-scale elements, which are beyond the capabilities of currently available "top-down" and "bottom-up" manufacturing methods. Mechanical assembly of nano-scale objects via "contact-based" manipulation has the potential to fill the void between these currently available methods and as such may prove fundamental in the advancement of nanomanufacturing. Fabrication of advanced nanoscopic structures and mechanism by means of mechanical manipulation is currently limited due to an insufficient understanding of nano-scale multibody systems. This includes uncertainty regarding the response of individual nano-scale bodies and multi-link chains to externally applied forces. Expanding the understanding of these behaviors may enable the design and operation of advanced nanomanipulation tools as well as the assemblies they produce.

Toward these ends, this thesis work investigates the kinematics and mechanics of manipulation and the feasibility of mechanically assembling nano-scale structures, viz. multi-walled carbon nanotubes. This work is accomplished in three parts through: (1) investigation, design, and fabrication of tools for dexterous manipulation of micro-/nano-scale components; (2) construction and execution of experiential procedures designed to demonstrate the unique kinematic and kinetic constraints present in multibody systems comprised of nano-scale structures; and (3) development of a model that formulates the observed behavior in a manner suitable for multibody dynamic simulation. The following sections present the background and motivation; the research issues, including literature review; the objectives and proposed strategies of this research; and the organization of the remainder of the thesis.

1.1 Background and Motivation

The directed assembly of micro- and nano-scale objects through mechanical "contact-based" manipulation represents a promising means to manufacture unique structures and devices. Substantial interest has been given to this manufacturing method in recent years because of its potential to enable a broad range of applications from science and engineering to health and medicine [1, 2]. This is due to its ability to construct complex spatial products from disparate materials currently incapable of being produced using other micro-/nano-fabrication techniques. In contrast, mature manufacturing methods used at these scales are predominantly restricted in both the geometry of the products they create and the material with which they are produced. These mature methods are separated into two categories: "top-down" and "bottom-up" fabrication techniques. Top-down methods generally refer to those which add or remove bulk material. Many of these have been inherited from the integrated circuit (IC) industry and include lithography, imprinting, and chemical etching for use at both the micro- and nano-scale. "Bottom-up" strategies are assembly-based techniques where the constituent parts are combined at the molecular scale. These techniques include methods such as self-assembly, dip-pen lithography, and directed self-assembly [2]. Contact-based manufacturing methods are poised to fill the gap between these two strategies through the physical manipulation and assembly of the micro-/nano-scale parts created by either top-down or bottom-up techniques. This method promises considerable advantage when the parts to be assembled are made from different materials, involve incompatible fabrication processes, or are to be arranged in complex three-dimensional shapes [1, 2].

Contact-based assembly, however, has yet to fully achieve this capability due to current limitations in the manufacturing approach. One major limitation is the difficultly encountered in combining the dexterous functionality required for robust manipulation with the scalability required for mass production. State-of-the-art manipulation and assembly systems such as nano-robotic manipulators [3–6], coordinating micro-scale probes [7, 8], and precision articulated robotic arms [9, 10] have demonstrated the ability to handle micro- and nano-scale parts. However, the degree of dexterity achieved by these systems is accomplished through (1) exploiting the large range of motion and degrees of freedom offered by macro-scale positioners, (2) the intuitive control of a human operator, or (3) combining both macro-scale mechanics and human intuition for controlled manipulation.

Scalable manipulation systems—referring to the ability to fabricate miniaturized hands [11] or 'factories-on-a-chip'—capable of *dexterously* assembling micro-/nano-scale parts appear to require the use of *dynamic* robotic grasps. Dexterity regarding robotic systems can be thought of as the ability of a manipulator to achieve arbitrary positions and orientations (*poses*) of an object in its grasp while being constrained within the workspace [12]. Dexterity is often achieved by allowing the grasp of the object to change dynamically during manipulation to avoid constraints. As the scale of the system is reduced, dexterity becomes an increasingly important ability in addressing the physical and operational constraints. This can be illustrated by imagining the dynamic nature of the human grasp while tying a knot using small-diameter yarn. In this scenario, a bulk of the manipulation is performed by the fingers moving relative to the palm. A static grasp, in contrast, fixes the kinematic relationships between the end-effectors and object and subsequently requires additional, external manipulators to perform the task. While this can often accomplish the same task, imagine the difficulty and workspace necessary to tie the same knots while only using one's shoulders, elbows and wrists. The mechanics of the grasp may be simpler but the required system is much larger. In contrast, controlled dexterous manipulation may enable smaller systems but involves greater complexity in the grasp. Hence, a thorough understanding of the contact between the end-effectors and the object is required. This is where many of the limitations lie in micro-/nano-scale manipulation because of the complications imposed by stiction at the contacting interface caused by nano-scale interactions.

1.1.1 Attractive forces at the micro-/nano-scale

The study of micro-scale physics and how the associated forces alter the behavior of sub-millimeter-scale solids has had a great effect on the field of contact-based manipulation. As outlined in [13], volumetric forces such as gravity have far less influence on the behavior of objects as opposed to surface forces, such as capillary, electrostatic, or the weak intermolecular forces. This reversal in the practical importance of each force has been termed the "scaling effect" and has been investigated with respect to various material parameters [14]. Regarding contact-based manipulation, the dominant phenomena of interest deal with the mating interface between components, specifically the adhesive and frictional effects of contact. Both adhesion and friction, caused by the weak intermolecular forces (van der Waals interactions), is of the greatest concern because of its ubiquitous influence [13]. Adhesion of micro- and nano-scale parts has been shown to be a function of material properties, bulk geometry, and surface roughness. In micro-manipulation it has been treated using three basic methods: (1) by direct calculation of the van der Waals attraction between parts in contact [13, 15–21], (2) by various elastic deformation models for both smooth [22–35] and rough surfaces [36–38], and (3) by a combination therein for a rough adhesive surface with van der Waals attraction [39]. For nano-manipulation of objects, investigations have used numeric simulations to show that the continuum-based elastic deformation models also appear to hold for structures such as carbon nanotubes [40]. Friction has been studied to a lesser extent for both micro-scale [41–46] and nano-scale [47–53] objects in contact as well. Together, these works represent a large effort toward understanding the sub-millimeter-scale physics of solids in contact.

1.1.2 Micro-/nano-manipulation Tools

In parallel, numerous investigations have addressed the novel instrumentation requirements posed by contact-based micro-/nano-assembly operations. This has resulted in a diverse set of state-of-the-art manipulation tools that span a range from the relatively large, complex, and dexterous, to the compact, simple, yet kinematically limited systems. Notable examples of these systems include those based on the atomic force microscope (AFM) [54–58] and its derivative, the nano-robotic-manipulator (NRM) [3–6, 59]. The AFM has been used effectively to mechanically push and arrange nano-scale objects such as nano-particles over various surfaces by using the AFM tip in contact mode. The NRM systems have improved upon the AFM model by using multiple AFM tips mounted on independent positioning stages. These utilize up to 16 DOF and have demonstrated the successful manipulation and characterization of carbon nanotubes as well as their assemblies [5]. Others using NRMs have also expanded the programmable functionality of such systems to achieve automated assembly of pyramids built from microspheres [6]. These systems rely on macro-scale actuation schemes to achieve their dexterity, circumventing the need for investigating the mechanics of a robust micro-/nano-scale grasp model. Additional examples of contact-based manipulation include positioning stages [60–66], micro-grippers and nano-tweezers [67–75], and integrated devices involving aspects of both positioners and grippers [7–10, 76–80]. More recently, researchers in the Microsystems and Devices Laboratory at UIC have developed an advanced concept wherein coordinating end-effectors with multiple DOF are located on a single chip [81–84]. This system has been shown to be capable of performing various micro-assembly operations on-chip, including grasp, rotate, move, and release tasks involving multiple work-pieces. Subsequently, a device based on this concept of on-chip assembly using multiple fingers was reported by other researchers pursuing a similar line of investigation [85]. In all, a great deal of progress has been made toward developing the hardware necessary to perform micro-/nano-scale assembly operations.

1.1.3 Assembly and Joining of Carbon Nanotubes

Both an understanding of the fundamental mechanics and the tools of manipulation are critical for achieving the potentially useful applications of micro-/nano-assembly. For MEMS and NEMS in particular, the bonding of carbon nanotubes to each other and disparate structures has shown particular promise in applications requiring part joining [86–88] and interconnects between electrodes for sensing and actuation [89–91]. Initial results concerning these applications have been achieved through (1) simple adhesion of carbon nanotubes [3, 4, 90, 91], (2) junction soldering via electron-beam induced deposition [4, 5, 89–97], and thermal annealing [92, 98], (3) mechanochemical bonding [4, 5], and (4) current induced Joule heating [86, 88, 99]. These methods could foreseeably be used to assemble a range of complex products involving nano-scale patterns and/or components, including: compliant nano-scale devices (multi-bar mechanisms), nano-fluidics systems (ports and pipes), nano-electrical elements (square-loop solenoids, electrodes for electrochemical double-layer (ECDL) capacitors), nano-structures (parallel chord trusses), nano-textiles, and bio-mimetic architecture (cellular models). Conceptual images of such systems are offered in Figure 1.1. Synthesizing micro-/nano-scale physics with contact-based manipulation and assembly systems in a more systematic manner may allow for the construction of such intricate products and their novel applications. To do so, however, the mechanics of adhesion that exist between nano-scale structures and/or a nano-scale structure and the manipulators must be addressed first.

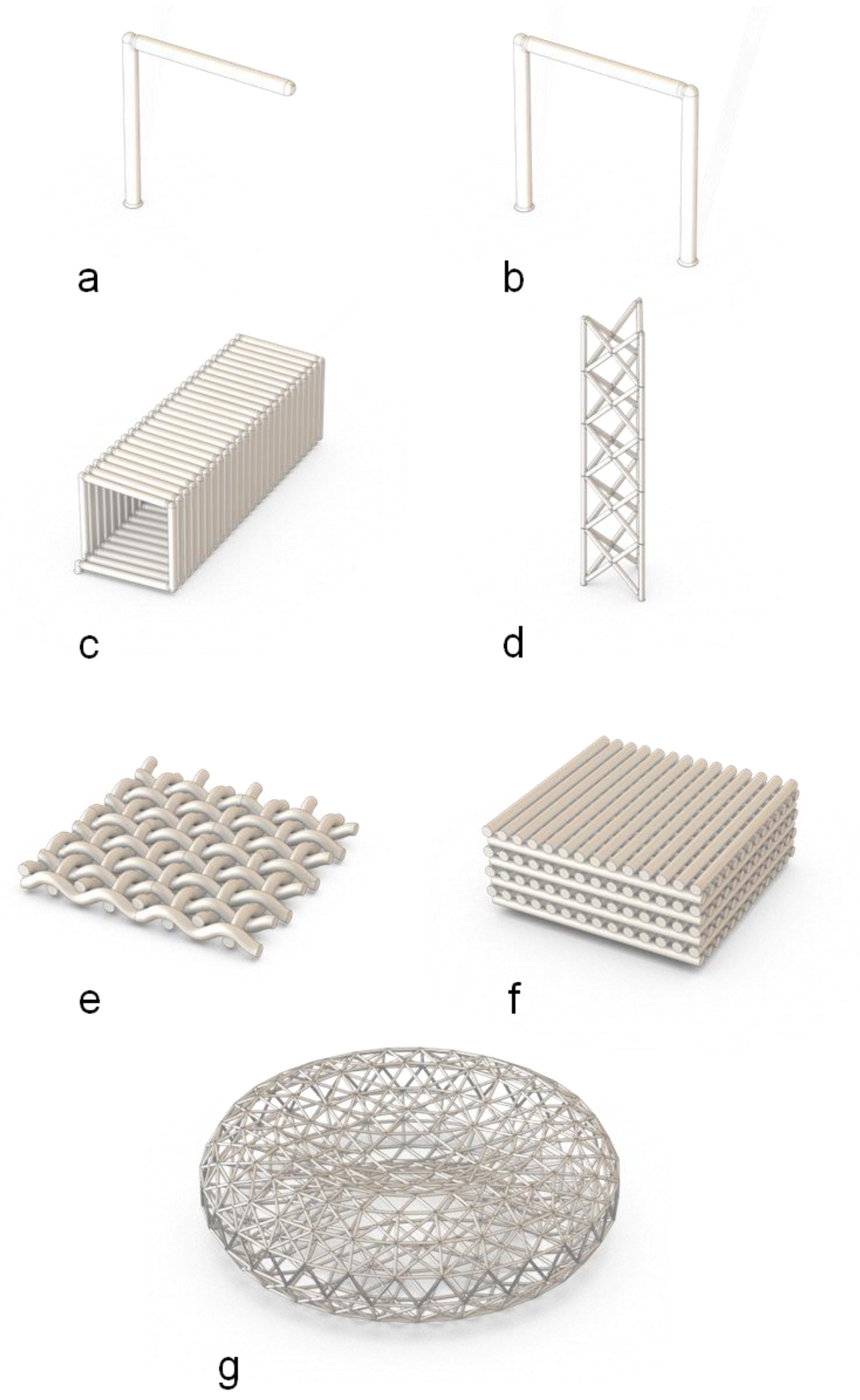

Figure 1.1: Conceptual images of possible structures and mechanism manufacturable with contact manipulation and welding: a) kinematic pair, b) four-bar mechanism, c) square-loop solenoid, d) parallel cord truss, e) woven textiles, f) electrode for an ECDL capacitor, g) scale model of a red blood cell's surface (Ø = 60 nm for all CNT segments shown).

1.2 Research Issues

Addressing the limitations of current contact-based micro/nanofabrication from the perspective of the mechanics involved in a dexterous grasp has yet to be achieved. A majority of research into the hardware used for manipulation only considers the dominant nano-scale forces with respect to object capture and release, while relying on remote macro-scale actuation schemes to supply the dexterity. This hinders both the current ability to manipulate nano-scale objects and the future ability to design the required tools. Although a few methods for joint/welding carbon nanotubes have been presented in literature, a clear understanding of the mechanical qualities of the "joint" is currently lacking, including the available kinematic motion between bodies and potential energy dissipative effects.Such an understanding of the joint formed between two carbon nanotubes could be critical in enabling the assembly-based manufacture of nano-scale machines and structures such as those illustrated in Figure 1.1. The primary research issues that pertain to the study of a joint between two carbon nanotubes as well as to a manipulator's end-effector include: (1) to what extent can conventional continuum mechanics be used to model the mechanics of nanoscopic structures? (2) what are the kinematic and kinetic interactions of most interest between objects in dexterous manipulation—either to one-another or the manipulator? and (3) how can such information be modeled so as to advance the abilities of contact nanomanipulation? A thorough understanding of mechanical manipulation at the nano-scale may include answers to these questions.

1.3 Objectives and Approach

To address the issues discusses in the previous section, this research has broadly explored the mechanics and kinematics of contact-based nano-manipulation. Specifically, the aims of this work are:

Specific Aim 1: To observe and measure the structural properties of MWCNTs for use in contact nano-manipulation. This includes creating the means by which to visualize and manipulate MWCNTs as well as investigating the extent to which conventional continuum mechanics can be used to model the observed behavior.

Specific Aim 2: To observe and measure the adhesion between nano-scale components and its effect on the motion of bodies when constrained within mechanical grasps and assemblies. This includes understanding the limits of the attractive force between adhered bodies and the available degrees-of-freedom (DOF) while bodies remain in contact.

Specific Aim 3: To validate the findings of specific aims 1 and 2 by constructing a mathematical model capable of capturing aspects of the interactions observed.

Toward these ends, three approaches are used. First, a custom nanomanipulation system is designed and constructed, capable of visualizing and dexterously positioning MWCNTs. This is used to methodically apply forces and moments to MWCNTs in various configurations for the purposes of measuring the resulting deflection and comparing the results with equivalent macro-scale arrangements. Second, the manipulation system is used to dexterously position MWCNTs into kinematic assemblies. These assemblies are used to investigate the adhesive contact by applying forces and moments to the arrangement and observing the deflection of the constituent links. Third, the observations are formulated into a multibody expression for the MWCNT system. This is to determine the preliminary accuracy of the expressions by comparing the model to the experimental results. These approaches aim to contribute tools and mechanical theory for use in advancing the field of contact nanomanipulation.

1.4 Thesis Organization

The remainder of this thesis is organized into four parts. Chapter 2 discusses the design and fabrication of a novel system for nanomanipulation. This includes a review of the current state-of-the-art micro-/nano-manipulation systems, considerations in the design of dexterous nano-scale mechanical grasps, and system specifications. Chapter 3 employs the system in the execution of three sets of experiments. The first set examines the structural stiffness of a sample of MWCNT, their elastic modulus, and the applicability of continuum mechanics in describing the bending of these structures. The second set of experiments arranges the MWCNTs into kinematic pairs and uses the structural characteristics determined in Experiment Set 1 to measure the kinematic and kinetic behavior of the adhesive joint. The joint is then subjected to localized heating to investigate methods of strengthening MWCNT assemblies. The third set of experiments arranges three MWCNTs into a double-rocker four-bar mechanism with welded joints to demonstrate and measure the operation of a nano-mechanical assembly. Chapter 4 draws from the kinematic and kinetic observations gathered in Chapters 2 and 3 to formulate a multibody expression for the system. A general expression is explored for encompassing the breadth of observed behavior while a simplified, specific expression is solved for and compared with the experimental results. Chapter 5 summarizes the findings and discusses the results with regards to the specific aims of this work.

2 EXPERIMENTAL SET-UP

Addressing the research aims of this work requires the ability to observe and manipulate nano-scale structures. This includes the ability to visualize the position and motion of system components as well as the ability to apply controlled forces and displacements to them. Numerous microscopic- and nanoscopic-scale manipulation systems and components have been reported in literature featuring a broad range of capabilities [1, 6, 8, 9, 13, 15, 22, 60, 61, 68, 70, 72, 74, 80–85, 88, 100–108]. None, however, meet the operational specifications and constraints required for this work. Consequently, a customized nanomanipulation system is designed and fabricated to facilitate this research. This chapter covers the development and construction processes for this system and includes the design and fabrication, performance overview, and remarks on the system capabilities.

2.1 Design and Fabrication

Mechanical manipulation systems for use with nano-scale structures generally consist of four primary components or subsystems: the structures to be manipulated, the observation system, the manipulation tools, and the environmental control system. This categorization allows systematic consideration of the objects to be manipulated, how the manipulation is to be observed, how it is to be manipulated, and how control over the manipulation environment is ensured. Through careful consideration of the research objectives and operational constraints, this design process has resulted in a dexterous nano-manipulation system consisting of two independent, coordinating nano-scale probes operating in a controlled environment at ambient pressure for use with large diameter, vertically aligned carbon nanotubes, and visualized using a traditional optical microscope. A schematic of the system can be found in Fig. 2.1 and includes: two three-degrees-of-freedom (DOF) linear positioning systems (manipulators), objective lens of the optical system, the focal plane of the microscope, a reflective background used to visualize the nano-structures, and an array of MWCNTs. The selection, design, and fabrication of each component are discussed in the following sections with regards to the four primary nano-manipulation subsystems.

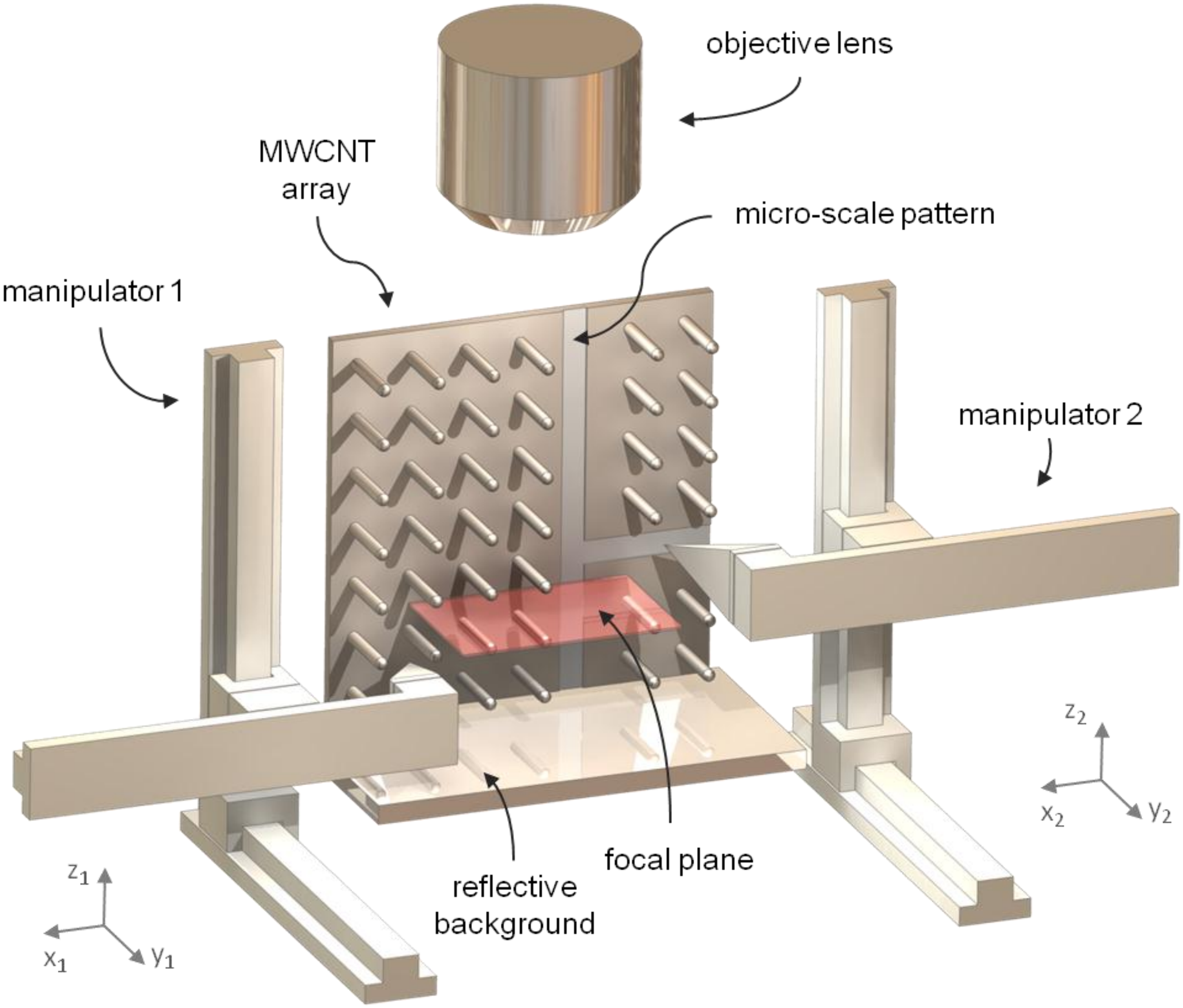

Figure 2.1: A schematic of the contact nanomanufacturing system used throughout this work

2.1.1 Nano-Scale Components

A wide variety of nano-scale components are available for nano-manipulation including nanotubes (NT), nanowires (NW), nanorods (NR), nanofibers (NF), and nano particles (NP). Concerted effort has been directed toward researching these components due to their notable structural, mechanical, chemical, and/or electrical properties. In particular, carbon nanotubes (CNTs) have demonstrated exceptional tensile strength, electrical conductivity, structural aspect ratio, and surface functionalization. This has led to the proposal of CNTs as ideal components for various advanced nano-scale structures and mechanisms as reviewed in [109].

In addition to their potential applications, carbon nanotubes exhibit features that are particularly beneficial to the study of nano-manipulation, including their cylindrically symmetric shape, electrical conductivity, range of dimensions, and ordered arrangement during fabrication. Structures with cylindrical symmetry aid in nano-manipulation because they can feature dimensions in the axial direction that are much larger than those in the radial direction while maintaining nano-scale behavior. This increases both their ease of manipulation—by offering more potential points of contact—and ease of observation—by increasing the surface area. Likewise, electrical conductivity is useful in confirming mechanical contact with the CNT as well as in delivering controlled electrical heating to specific regions of its structure. Electrical conductivity is also critical for certain methods of observation such as scanning electron microscopy (SEM) where charge collects on the structures being observed and must be dissipated. Similarly beneficial, the relative dimensional control of CNTs during fabrication allows the size of the structure to conform to the positional and observational limits of the nano-manipulation system. The fabrication method also dictates the arrangement in which the CNTs are grown and can range from chaotic to relatively ordered. Considering both the potential future applications of CNTs along with their beneficial characteristics regarding mechanical manipulation, CNTs are chosen as the nano-scale components for use throughout this research. In particular, large diameter (100-500 nm), high aspect ratio (> 1:20), conductive, and well-ordered CNTs are sought. Meeting these specifications requires consideration of the CNT form and fabrication method.

Carbon nanotubes exist in a variety of forms featuring specific structural and electrical properties. Single walled CNTs (SWCNTs) are the simplest form and consist of a hollow cylinder whose wall is composed of a single continuous layer of graphene. Two distinct electrical types of SWCNTs exist—metallic and semiconducting—and are distinguished by the arrangement of the carbon atoms along the axis of the cylinder, referred to as the tube's chirality [110]. Multi-Walled Carbon Nanotubes (MWCNTs) feature walls with multiple graphitic layers. In the ideal MWCNT, the basal graphene planes are parallel to the central axis of the tube and appear as a collection of concentric SWCNTs. In the stacked-cone arrangement (also known as bamboo structure), the basal graphene planes are not parallel to the central axis and appear as a collection of concentric cones; forming tubes that feature larger hollow interior cavities relative to parallel-walled MWCNTs [111]. Both arrangements of MWCNTs—parallel and stacked-cone—exhibit metallic behavior. While the precise demarcation between stacked-cone MWCNTs and carbon NF is not well defined, cylindrical structures primarily composed of ordered graphene walls that encompass central voids will be considered MWCNTs in this work. Using this definition and considering current fabrication limitations, electrically conductive CNTs with diameters on the order of hundreds of nanometers and lengths greater than 10 μm are predominately stacked-cone MWCNTs.

Various fabrication methods for CNTs exist—arc discharge, laser vaporization, chemical vapor deposition (CVD) —which influences the internal structure and relative arrangement of the CNTs produced. The material quality of individual tubes can vary considerably between production methods as well as within a single sample. Potential defects range from the easily noticeable errors such as curved or kinked structures to the more minute errors such as gaps or impurities in the lattice itself. These deviations from the ideal CNT structure can be mitigated to a degree though not yet robustly controlled [109]. The relative arrangement of the CNTs produced is another important consideration. While methods such as arc discharge can produce high quality material, the resulting CNTs are arranged in a disordered, soot-like grouping colloquially referred to as a 'rats-nest' where mechanically isolating single CNTs from the group, if possible, is difficult. Methods such as plasma enhanced CVD (PECVD) are capable of producing relatively ordered arrangements of CNTs with each tube individually isolated and oriented perpendicular to the substrate. This perpendicular arrangement is referred to as vertical alignment. To achieve well-spaced (> 1 μm separation) vertically aligned MWCNTs suitable for this investigation, PECVD is chosen as the fabrication method.

Fabrication of the MWCNTs used in this work is performed commercially by NanoLab Inc. Each sample consists of a sparse array of stacked-cone MWCNTs grown atop a chromium-on-stainless-steel substrate via PECVD. The array covers an area of approximately 15 mm by 15 mm with a site density of 10^6 CNT/cm^2, an average outer diameter of 250 nm, and an average length of 11 μm. This offers a potentially large number of CNTs to experiment with, wide clearance between each tube to insure isolation, and dimensions that will aid in both observation and manipulation. A series of three images are presented in Figure 2.2 depicting the samples fabricated for this work using three different methods of visualization: transmission electron microscopy (TEM), scanning electron microscopy (SEM), and optical microscopy using the experimental system created for this work.

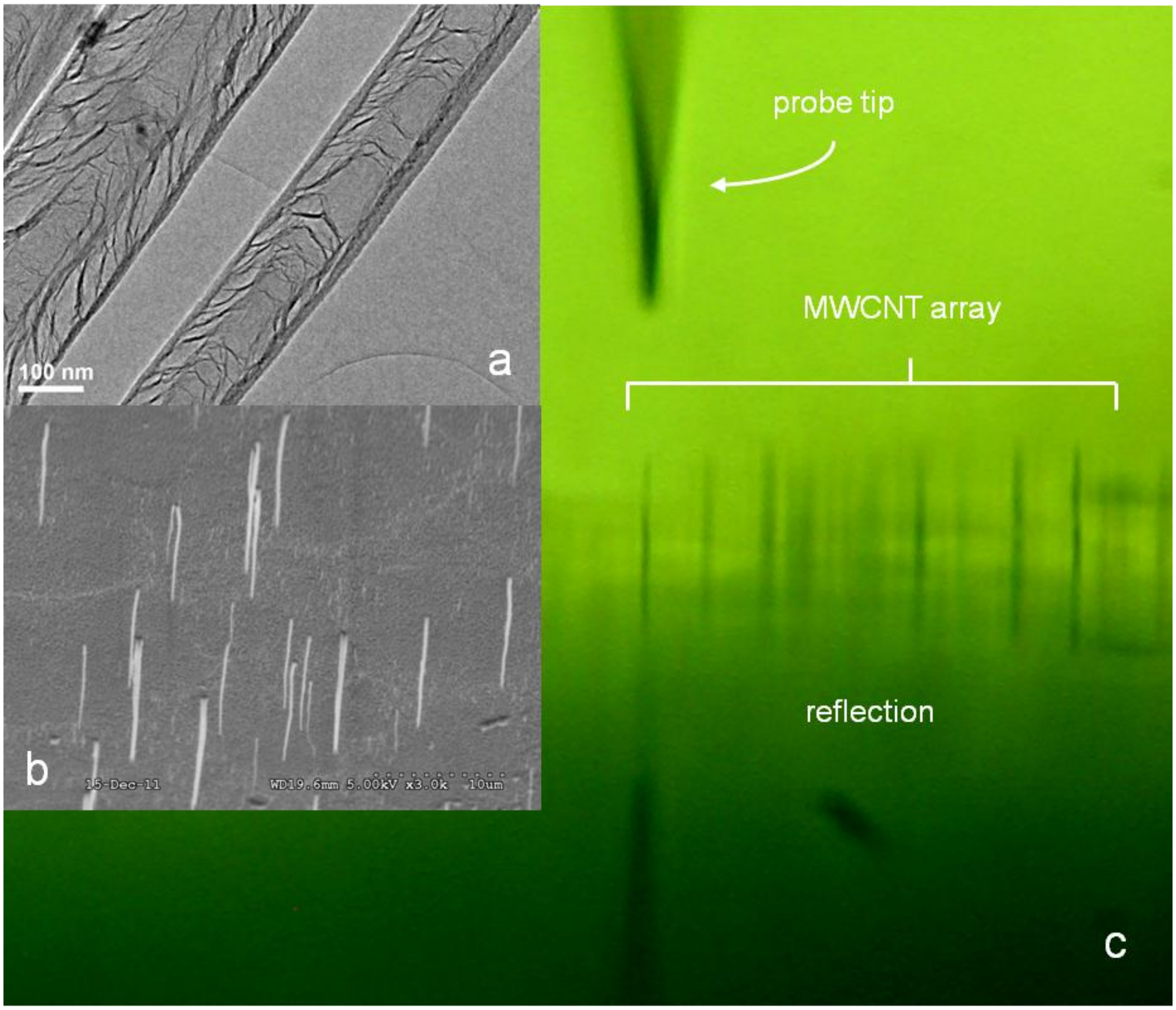

Figure 2.2: TEM, SEM, and optical images of the MWCNT array used in this work where a) is the TEM image at x430k magnification, b) is the SEM image at x3.0k magnification, and c) is the optical image at x40 magnification (with a micro-probe captured in the frame)

2.1.2 Optical Visualization Tool for Nanostructures

Tools for visualizing submicron scale structures often drive the design constraints of nanomanipulation systems due to their high cost, extreme operating environments, and the small available volume in which manipulation equipment can be placed. Scanning electron microscopes (SEM), transmission electron microscopes (TEM), and atomic force microscopes (AFM) are the predominate visualization methods used in nanomanipulation [5, 31, 54, 59, 88, 93, 105, 112]. These methods can provide high resolution imaging of the nano-scale structures but almost exclusively require the workspace to be housed in a vacuum chamber. These chambers are often too small to fit a system of macroscopic scale positioners and the environment requires the positioners to be vacuum compatible. Each of these constraints adds additional cost to the overall system. Since the aim of this work is to study the kinematics and mechanics of nano-manipulation, greater flexibility is desired in the design of the manipulation tools. Hence, a novel optical visualization technique is explored to allow for this broader manipulator design.

Reports of the optical visualization of objects smaller than the diffraction limit of light have been given previously in literature. This includes the visualization of sheets of graphene (multiple and single layers) [113, 114] and carbon nanotube bundles as small as 1-5 nm in height [115]. These works rely on an interference contrast between the sample and the supporting surface and therefore were performed with the material lying atop the substrate. The work reported here relies on a similar interference contrast; however the samples are suspended 10 - 1250 μm above a diffusely-reflective metallic surface, allowing the nanostructures to be manipulated freely for the purpose of experimentation. The reflective surface is placed normal to the path of the incident light and perpendicular to the substrate on which the MWCNTs are grown, giving a 'side view' of the structures as indicated in Figure 2.1. This method has been used to successfully visualize and manipulate freestanding CNTs with a minimum feature size as small as 100 nm.

The system consists of a Mitutoyo optical compound microscope (×1–×2 continuously variable) with an M Plan Apo 20 (×20, NA 0.42) and a M Plan Apo 50 (×50, NA 0.55) objectives and coaxial light source. The thin edge of a 0.25 mm thick sheet of stainless steel is used as the diffusely-reflective surface in the background of the image while the light source is a SCHOTT ACE I with an EJA 21V150W bulb (white light). A Nikon DXM1200 digital camera captures the image for analysis using Metamorph 6.3 software with frame exposure times of 200–500 ms. With the microscope at ×2, the camera offers a resolution of 0.168 μm/pixel and 0.066 μm/pixel with the ×20 and ×50 objectives respectively. Three images of the same array are shown in Figure 2.2, where image *c* is captured using the apparatus described above for comparison. It is also interesting to note that the contrast gradient of the optical image inverts in this set-up between the magnifications of ×40 (as shown in Fig. 2.2*c*) and ×100 (as shown in experimental images presented in Chapter 3). At the highest magnification, it is the MWCNT that appears lightest while the background is dark. This optical system allows for a broader range in the design of the manipulation tools in terms of both size and environmental compatibility.

2.1.3 Manipulation Tools

Existing tools and strategies for micro and nano-scale manipulation encompass a wide breath of approaches as surveyed in [1]. To better address the research objectives of this work and describe the design approach used herein, a categorization method is adopted where tools are classified with respect to the number, type, and kinematic independence of the contacting surfaces used during manipulation. This is to aid in determining how many end-effects are necessary to fully control the pose of a nano object, what shape or form the end-effectors should take, and how many degrees of freedom each end-effector should have. Auxiliary tools, such a electrical sources are also discussed regarding their role in aiding manipulation.

The contact type defines the manner and degree to which a structure's position can be mechanically controlled via the end-effector of a manipulation system. As such, understanding the behavior of surface contact is a critical consideration in nano-manipulation. At the submillimeter scale, this interaction is complicated by the dominance of surface forces, which are capable of exerting strong attractive and/or repulsive influences between the interacting bodies [13]. This interaction differs greatly from contact between macroscopic scale bodies due to the differing rates at which inter-body forces scale with length. Investigating this effect has been codified into scaling laws [116] which provide a useful guide regarding the relative dominance of forces at various length scales. Generally, as the characteristic dimensions of a body decrease the effects of volumetric forces (e.g. gravity) become negligible relative to surface forces (e.g. capillarity, electrostatic, and weak intermolecular forces). Although the effect of many surface forces can be altered or negated through modifying material and/or environmental characteristics [13, 15, 22] the effect of weak intermolecular forces remain ubiquitous [13]. It is the attractive behavior of these weak intermolecular forces—also referred to as Van der Waals interactions—that will be considered in this work, and result in adhesive contact between the end-effectors and components of nano-manipulation systems.

Adhesive contact at the nano-scale is similar to planar frictional contact at the macro-scale. That is because most bodies naturally adhere together due to surface energy. This energy works to deform the region of contact so as to minimize the total energy of both bodies [32, 117–119]. The resulting contact area, even for bodies with initially curved surfaces, can be approximated as a plane. In addition, this surface naturally resists any change in the contact area due to the associated change in energy required for such motion. This results in a restorative force resisting any change in orientation between the two bodies. Using the terminology of macroscopic scale robotics, this single contact is the nano-scale equivalent of a macro-scale multi-contact force closure grasp [120]. As such, a nanomanipulation system is capable of stably grasping a nano-scale structure with the use of only one end-effector.

In practice, a single probe with the degrees of freedom, range, and resolution of motion necessary to execute general nanomanipulation tasks is rarely used. Instead, multiple end-effectors with reduced individual capabilities are often employed to achieve the same task while occupying a smaller volume. Since multiple end-effectors will be considered in this design, the kinematic independence of the surfaces used to control the pose of nano-objects is also an important metric in classifying manipulation systems. A grasp can be identified as either static or dynamic when describing the relationship of the end-effector(s) to the component. Static grasps exist when the kinematic relation between the end-effectors and the component remain unchanged during the manipulation and assembly operations. This is the case with positioners and grippers [8, 9, 60, 61, 68, 70, 72, 75, 102, 103, 105, 106, 108]. Dynamic grasps exist when this kinematic relationship changes during operation, such as with tweezers, multi-probe, and multifinger systems [6, 7, 80–85, 88, 107]. The number of adhesive contacts dictates the number of degrees of freedom each end-effector must have to achieve full dexterity. It follows that for two adhesive contacts with a nano-object, each contact must be capable of at least three independent DOF in order to fully control the position and orientation of the object in the workspace.

Two independent end-effectors, both capable of three linear DOF, is chosen as the manipulator arrangement for this study.. Each DOF is supplied by a New Focus 8301 Pico Motor (step size ≤ 30 nm, range 12.7 mm) installed in a New Focus 9066-COM-E-M closed loop control stage (CL step size = 80 nm) which when assembled occupies approximately 22 by 50 by 96 mm^3. The MWCNT array is attached vertically to a three DOF manual positioning stage (Melles Griot) placed within the mutual workspace of both end-effectors. A solid model and image of the positioning system is shown in Figure 2.3 with select macro-scale components from Figure 2.1 identified.

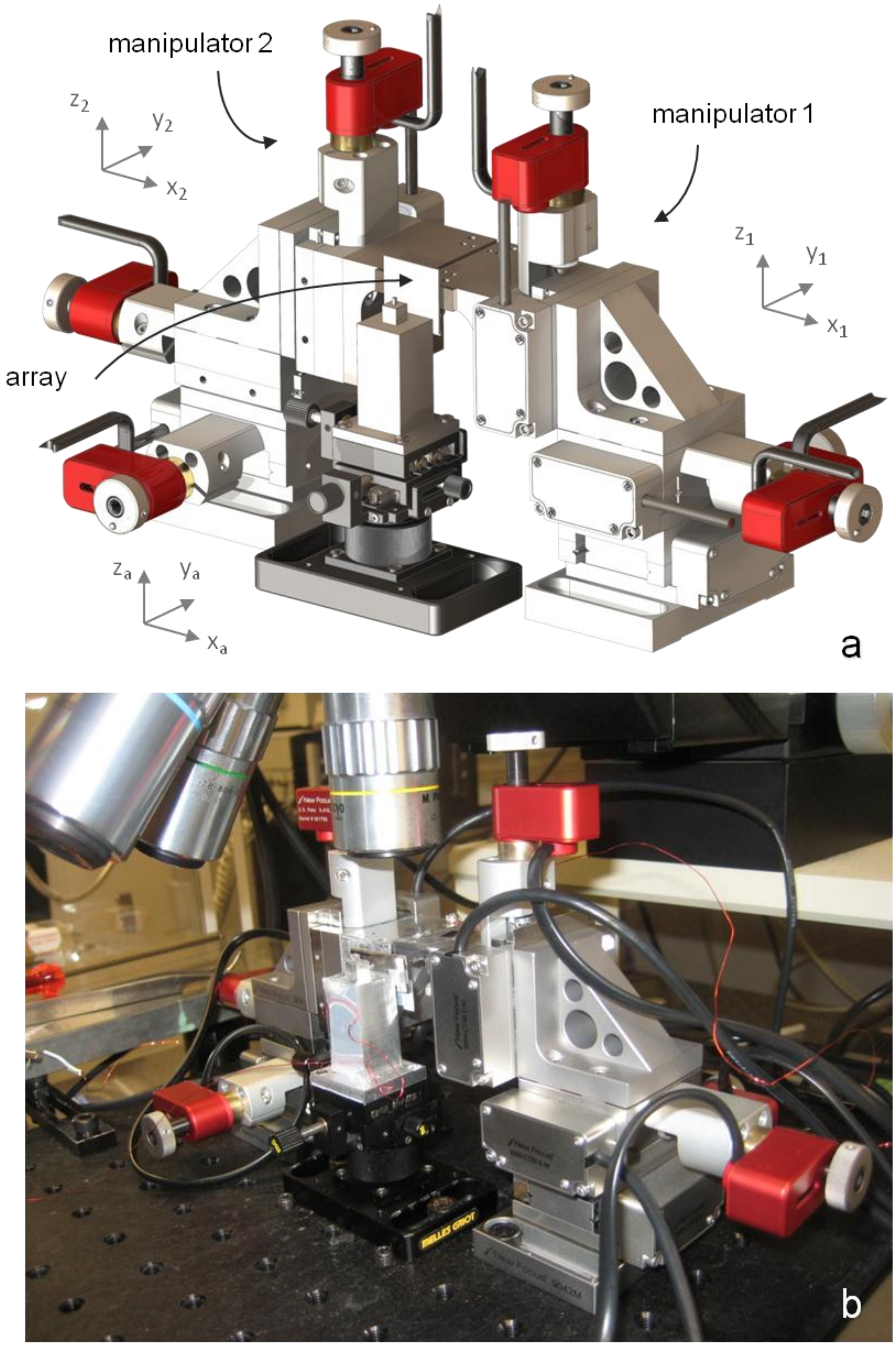

Figure 2.3: The mechanical manipulation hardware shown both as a) a schematic representation and b) a photo with select macro-scale components

Each manipulator is designed to carry a variety of end-effectors to address the requirements of a range of experiments. Two probe types are chosen for this work: a low-stiffness, tip-less probe (Arrow TL1Au) for use as nano-Newton *force sensor*, and a fine tip probe (ATEC-CONTAu) for *dexterous nano-manipulation*. The stiffness, k, of the tip-less probe shown in Figure 2.4 *a.1* and *a.2* is measured in the lab to be 3.05 ± 0.07 mN/m. The procedure used to determine the stiffness is described in Chapter 3. To work most effectively as a force sensor, the tip is mounted on the positioning stages such that the length of the cantilever is parallel to the MWCNTs as-grown on the substrate. In contrast, the fine tip probe(s) is mounted such that the cantilever is nearly parallel to the substrate surface as shown in Figure 2.4 *b.1*, giving increased stiffness perpendicular to the MWCNTs.

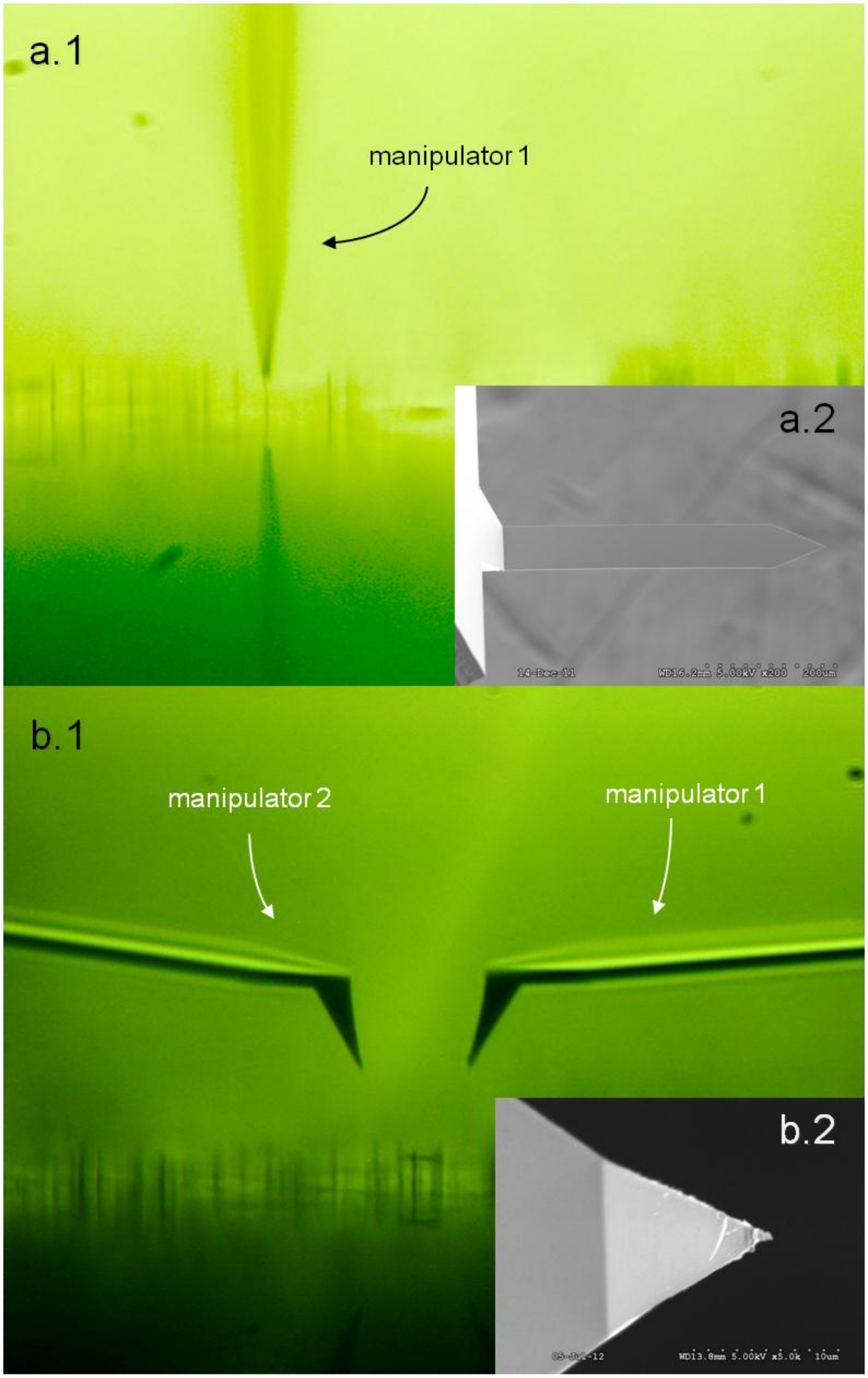

Figure 2.4: The two types of end-effectors used throughout this work: a) a Arrow TL1Au tip-less probe for use as a force sensor, and b) two fine-tip ATEC-CONTAu for use in dexterous manipulation

Electrical sourcing and measuring tools are also included in the system to compliment the mechanical manipulators. Sourcing and measuring the electrical values across various components in this system is performed using a Keithly 2611A current-voltage sourcemeter and serves two primary purposes: allowing high resolution position measurements, and direct Joule heating of CNT samples. While the optical method employed here is capable of visualizing sub-micron scale structures and their relative motion, absolute position between objects is difficult to detect with the required accuracy. This is overcome using a continuity-check method where an electric potential (3.5V, 100 nA limit) is applied between the micro-cantilevers (gold coated) and the MWCNT/substrate (metallic CNT/Cr-on-stainless-steel). Contact is determined within the positioning resolution of the stage by detecting when the sourcemeter imposes the current limit. No detectable damage is rendered to the CNTs using this method because the current limit, and associated power dissipation, is orders of magnitude lower that that used to demonstrate nano welding [88]. Heating of the CNT samples to the point of welding and cutting is the second primary role of the electrical sourcemeter. Following [88], the probes are capable of welding, cutting, trimming, and vaporizing specific CNTs by varying the current limit and maximum electric potential placed across the components. This electrical subsystem allows the end-effector to more accurately manipulate the nano-structures as well as modify them for assembly purposes.

To ensure that the system is capable of manipulating the same nano-structure across various experiments, a method for locating specific MWCNTs in the array is devised. Repeatedly locating the probe tips relative to specific MWCNTs is achieved by marking the substrate with a network of micro-scale patterns. To create these patterns, a simple blade (X-acto, #11) is attached to a positioner and dragged across the surface of the substrate. This results in well defined, linear 20 µm wide voids (paths) within the MWCNT array. The location of each tube is reached by noting its position relative to the intersections of these paths as illustrated in Figure 2.1 and demonstrated in Figure 2.5. This provides the freedom to remove the MWCNT array from the nanomanipulation system for imagining under an SEM while still allowing the array to be replaced and additional experiments to be performed on the same MWCNTs.

Figure 2.5: Pattern of markings cut into the array for use in locating specific MWCNTs over multiple experiments

Control of both the mechanical and electrical manipulation tools is centralized in a custom LabVIEW virtual instrument (VI). The VI has direct control over the position of each stage, the voltage and current limits, as well as the components across which the potential is applied and its direction (i.e. $^{+}$probe 1 $\rightarrow$ $^{-}$probe 2, $^{+}$probe 1 $\rightarrow$ $^{-}$substrate; $^{+}$probe 2 $\rightarrow$ $^{-}$substrate, etc.). The position of the stages can be controlled either by directly entering the displacement/destination for each stage numerically or by controlling multiple DOF of each stage simultaneously using a commercial gaming controller (Microsoft XBOX

360). The command scheme for the gaming controller is shown in Figure 2.6. This system allows for the intuitive remote control of the nanomanipulation operations from outside of the environmental chamber.

Figure 2.6: Mapping of the commercial gaming controller (XBOX 360) commands to the motions of the manipulation system.

2.1.4 Environmental Control

Three categories of surface interactions dominate at the nanoscopic scale—electrostatic, capillarity, and van der Waals—of which only van der Waals is considered in this work. This is chosen because both electrostatic and capillary interactions can be negated through material choice and environmental control while van der Waals interactions cannot. Hence, it is the primary interaction that must be understood to enable advanced contact nano-assembly systems. To insure that van der Waals interactions are the only nano-scale surface forces present during manipulation and to protect the experimental workspace from external disturbances, the entire apparatus is isolated from the environment, as is shown in Figure 2.7. This isolation system consists of two subsystems: mechanical vibration isolation and particle/capillary/electrostatic isolation.

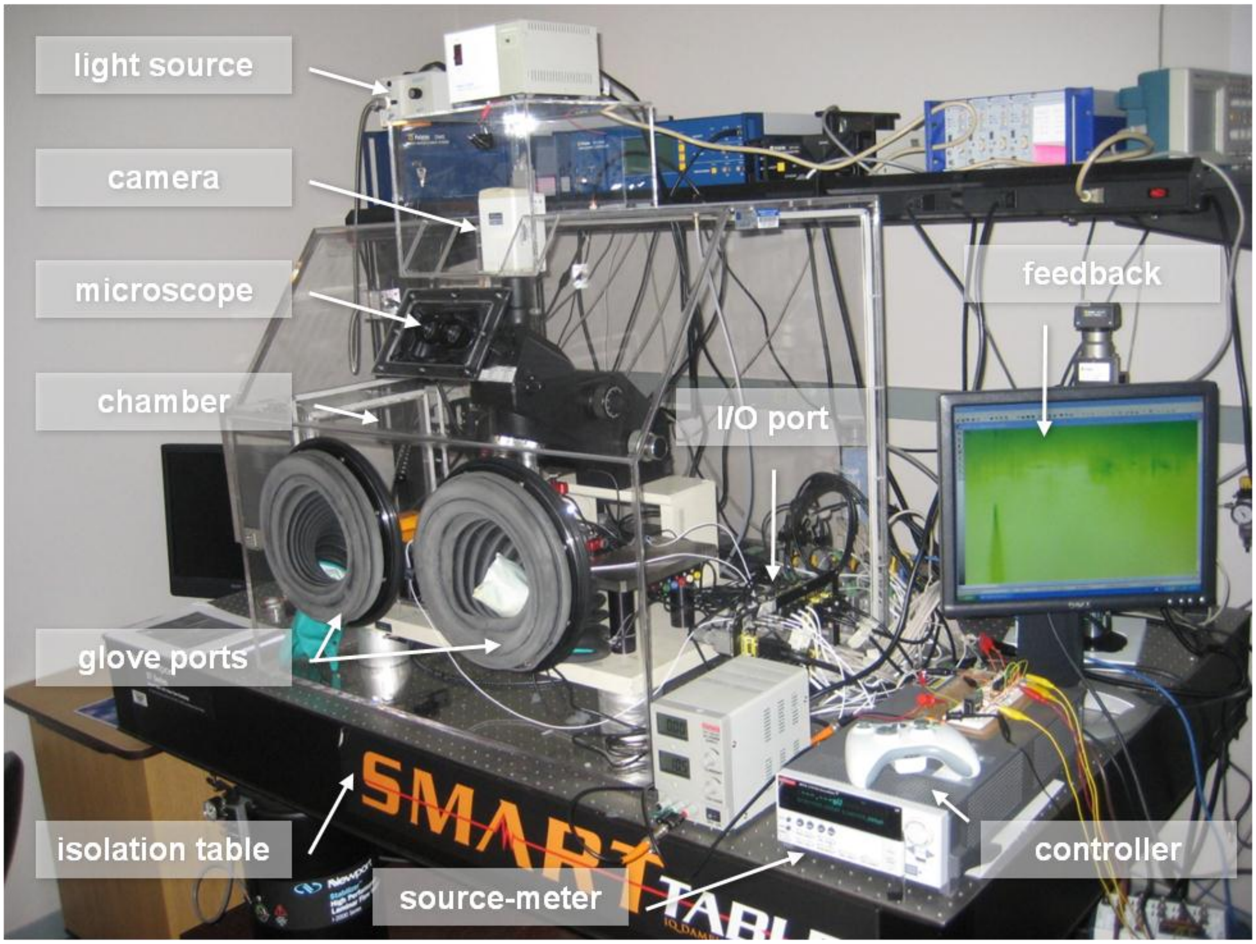

Figure 2.7: Picture of the complete nanomanufacturing set-up

Mechanical isolation from external vibrations is accomplished through the use of a Newport SmartTable optical table. The table is mounted on top of four I-2000 series pneumatic isolators controlled by an ST-200 SmartTable controller. It has a workspace of 1.2 by 1.8 m^2 with over 3400 M6 mounting holes spaced on a 25 mm grid. With the active damping of the isolators and the structural damping offered by the table, the system is capable of compensating for all noticeable external vibrations.

While mechanical isolation systems are commercially available, environmental isolation systems—that meet the necessary geometric and feature requirements—are not. Hence, a custom probe station is designed and fabricated for this work. The environmental system requirements include five primary specifications: the ability to (1) maintain low (< %5) relative humidity, (2) aid in minimizing buildup of electrostatic charge on critical components, (3) allow manual and remote optical feedback of the workspace, (4) allow operator access to the system components, and (5) allow multiple external analog and digital electrical connections to components.

To meet these requirements the Terra Universal 1540-00 Semiconductor Probe Station Mini-Environment is chosen as the base assembly for the environmental isolation chamber (EIC). It is capable of maintaining <10% relative humidity using nitrogen as the working gas; holding 25 Pa positive pressure; particle control with Class 100 conditions; static neutralization in under 30 sec for 0.1-1 kV; airlock pass-through access; glove ports; microscope bellows to allow access to the eye-piece outside of the chamber; and removable rear wall and side panel for equipment access. In addition, the probe station is altered to meet the remaining specifications as shown in Figure 2.8 by: adding a cupola on the top of the chamber to accommodate the microscope's digital camera, adding an array of electrical input/output (I/O) ports to the side access panel, and adding mounting flanges on the chamber wall to allow fiber optic illumination of the workspace.

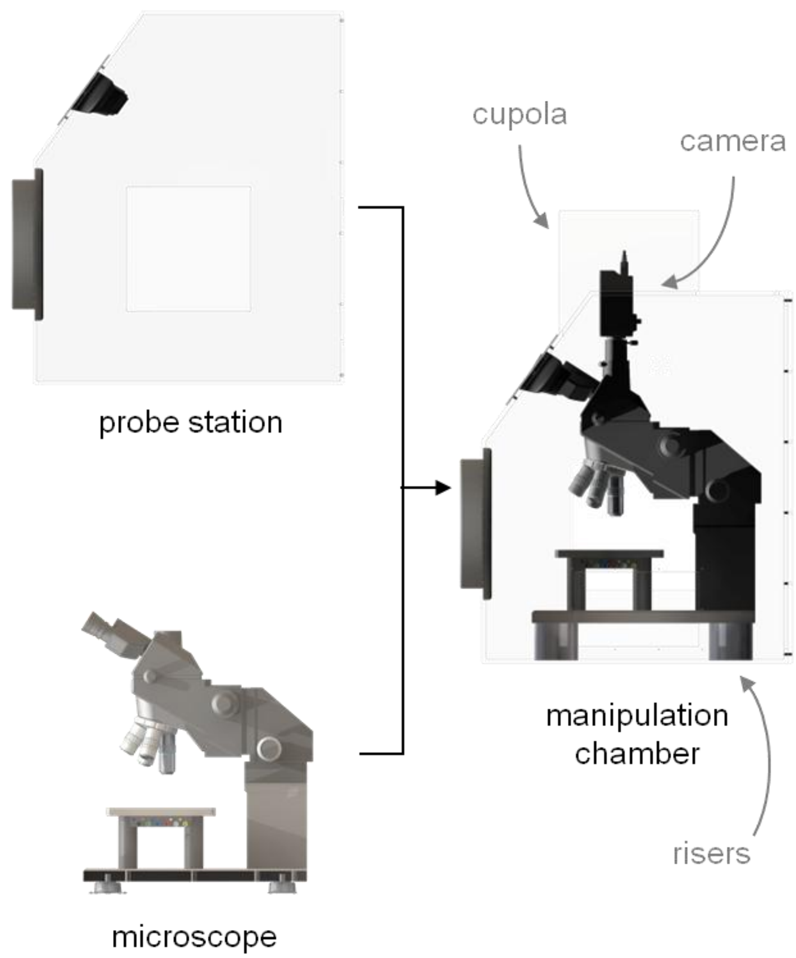

Figure 2.8: Various modifications made to commercial probe station for use as a manipulation chamber

The electrical I/O panel is fabricated from the access panel mounted on the right side of the chamber. At minimum sixteen ports are needed to operate all of the system features. These include one for the digital camera, twelve for the positioning system, and three for the electrical system. The layout of the panel is given in Figure 2.9*a* and shows how the ports are grouped by function. Both the digital-camera port and the positioning-stage ports are constructed from D-SUB mini-gender changers produced by Emerson Network Power. These are male-male (mfr. # 30-9536) and female-female (mfr. # 30-9537) connectors. For the digital-camera port, three connectors are attached in series (m-m, f-f, m-m) with one m-m connector positioned on the inner side of the panel. The positioning-stage ports communicate between the optical encoders and the closed-loop control system and are formed from two connectors in series (m-m, f-f). The remaining six ports for the positioning system control the Pico Motors. Each port is formed from two vertical angle through-hole mount RJ22 jacks from Tyco Electronics (mft. #5520257-2). The eight remaining ports on the panel are LEMO push-pull coaxial connectors (RAD.00.250.NTM). Three of these ports are used to provide analog electrical connection to the probe on manipulator 1, the probe on manipulator 2, and the substrate carrying the MWCNT array. The additional analog ports are to accommodate future experimental setups. After assembly, each port is sealed using thermoplastic to minimize airflow.

The optical fiber input mount is fastened to the left side of the chamber. It consists of two custom ports with set-screws as shown in Figure 2.9*b* and is used to align the fiber-optic cables that deliver light from its source through the chamber wall and to the microscope. To maintain the chamber's pneumatic integrity, the fiber optic cables do not pass through the chamber wall; rather they are simply aligned on either side of it. This preserves the seal with minimal loss of illumination in the transfer.

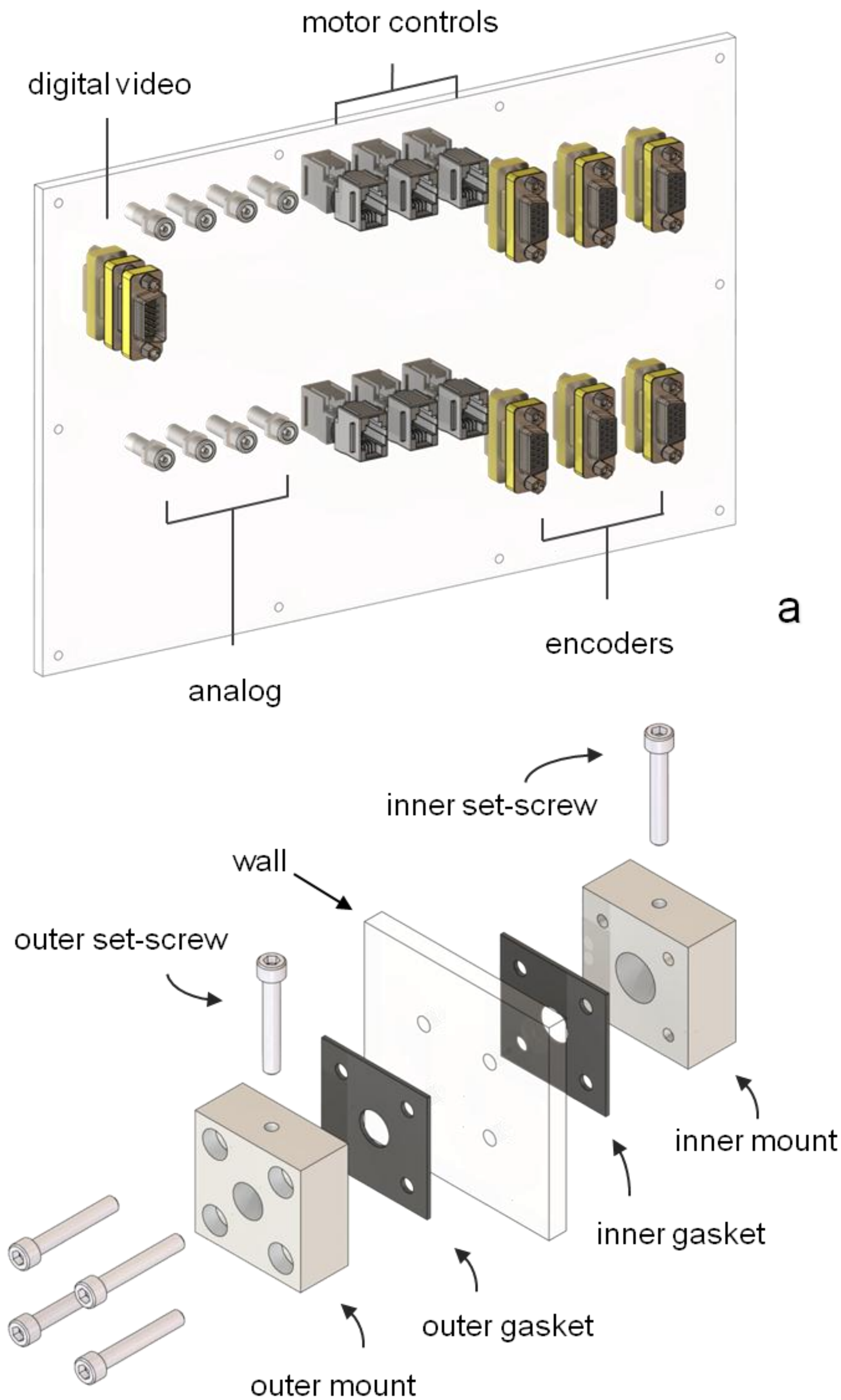

Figure 2.9: Chamber ports: a) electrical I/O panel, b) fiber optic input

In addition to the chamber modifications, support hardware is necessary to ensure that the capillary and electrostatic effects are negated. Capillary attraction is caused by liquid bridges that form between solid bodies where the liquid has condensed onto system components from water vapor present in the air. Quantifying the magnitude of this attraction is difficult when the liquid's meniscus radius drops below 2 nm. This is due to the fact that the continuum assumptions used to derive the equations are no longer valid below this threshold [121]. The threshold corresponds to a relative humidity of approximately 54%. While the equations may no longer be valid below this value, the exact extent of the remaining attraction is still unknown. Therefore, the system is designed to be capable of maintaining <5% relative humidity so that capillary effect, if any, can be experimentally determined.

Humidity is controlled by purging the chamber with high purity (99.9%) nitrogen for the purpose of negating capillarity. The nitrogen is first passed through a Drierite 26800 desiccant column before being directed into the chamber. Two gas ports are present on the top of the chamber as shown in Figure 2.10.; both SMC push-in pneumatic fittings to NTP 1/8" connectors. One is used to deliver the nitrogen to the chamber while the other is used to purge the humid air from it. A plastic tube is extended from the outlet port to the bottom of the chamber so as to allow the humid air to exit the chamber first during purging. This is because at normal temperature and pressure, the driest air is still denser than pure nitrogen. That is, the density of air ranges from $1.1936 < \rho < 1.2041$ kg/m^3 for relative humidity from $0\% < RH < 100\%$ while nitrogen maintains a density of 1.145 kg/m^3. An EXTECH hand-held relative humidity/temperature meter kit (mfr. # RH305) is used inside the chamber to determine when the desired RH has been reached. Its relative humidity sensor has a range of 0 to 100% with an accuracy of +/- 3%. Using this hardware the RH can be maintained throughout the nanomanipulation experiments.

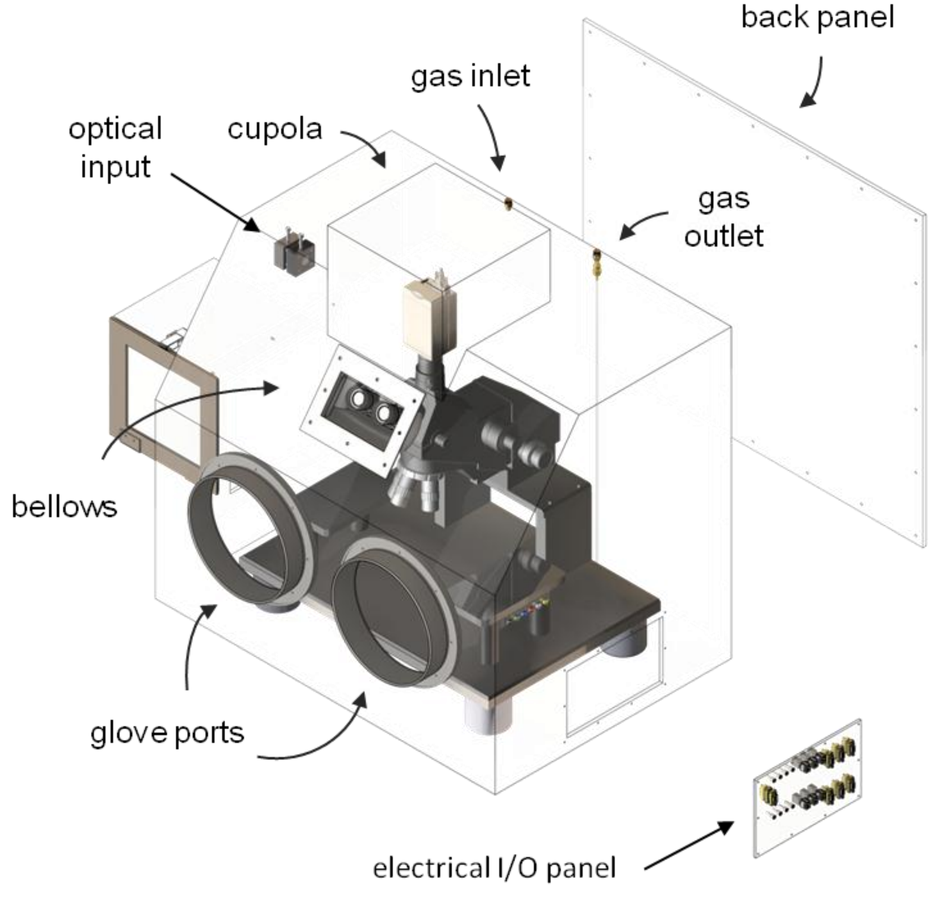

Figure 2.10: Environmental isolation chamber for contact nanoscopic manipulation

Electrostatic dissipation is achieved both actively by the components used during manipulation and by supplying ions to the chamber. Since the probes, substrate, and nano-scale structures are all electrically conductive, they naturally direct any charge built up from triboelectrification away from the workspace. To ensure no charges have collected on any equipment within the chamber between experiments, a Milty Zerostat anti-static hand gun is discharged inside the chamber prior to each experiment. Together, the capillary and electrostatic control processes facilitate the investigation of van der Waals interactions' role in the mechanics and kinematics of nanomanipulation. As a whole, the environmental isolation chamber provides sufficient protection of the workspace while maintaining the functionality of the system components.

2.2 System Specifications

To review the capabilities of this system, a condensed list of performance specifications is offered:

Visualization Method:	optical microscopy, white light; minimum distance per pixel, 0.066 μm/pix; minimum manipulated object dimension, 100 nm
Manipulation Surfaces:	"Probe 1", 1 surface, 3 DOF; "Probe 2", 1 surface, 3 DOF; "Substrate", 1 surface, kinematic ground
Positioners:	New Focus 8301 Pico Motors, step size, < 30 nm; New Focus 9066-COM-E-M, close-loop resolution, 80 nm
Force sensor:	Arrow TL1Au, $k = 3.05 \pm 0.07$ mN/m
Fine end-effector:	ATEC-CONTAu
Sourcemeter:	Keithly 2611A, contact detection, 3.5 V with 100 nA limit
Software Control:	LabVIEW, entered numerically or with gaming controller
Humidity Control:	nitrogen gas (99.9% pure), EXTECH RH305 sensor
Electrostatic Control:	electrically conductive components, Milty Zerostat anti-static gun

2.3 Remarks

The system presented in this chapter represents a dexterous nano-manipulation tool capable of grasping and manipulating nano-scale structures in near ambient conditions using optical microscopy. While the actuation of each probe still relies on macro-scale components, the setup is designed to investigate and address the issues currently present in the pursuit of miniaturized, dexterous, nanomanufacturing systems. Specific system capabilities include: the ability to repeatedly find a single MWCNT within an array, the ability to apply and measure force to nano-scale structures, and the ability measure and control electric potential to system components. Advancements in the understanding of dynamic adhesive grasps at the nano-scale are enabled through the use of this system toward the goal of achieving repeatable, automated, contact assembly of nano-structures and mechanisms.

3 MECHANICS AND KINEMATICS OF NANOMANIPULATION: EXPERIMENT

Contact nanomanipulation inherently involves applying mechanical loads to a nano-scale structure by a manipulator so as to affect its position and orientation. It follows that understanding how the nano-structure reacts to loading is of fundamental interest so as to control the manipulation process. Control, therefore requires an accurate model of a nano-structure's kinematic and kinetic behavior when grasped by a manipulation system. Currently, precise automated control of nanomanipulation processes is limited by a minimal understanding of these behaviors. Of specific interest is an understanding of the mechanical bending of nanoscopic components, such as MWCNTs, and the applicability of continuum mechanics in modeling the deflection. Additionally, an understanding of the mechanics of adhesion and how it alters the available techniques for applying loads to MWCNTs is of interest.

To address these limitations, a series of experiments are reported in this chapter, designed to investigate both the bending of individual MWCNTs and the adhesive constraints formed between MWCNTs and other structures. This is achieved through the use of calibrated micro- and nano-scale cantilevers which apply controlled displacements to MWCNT structures and mechanisms with the aim of measuring the forces associated with bending and adhesion. Three sets of experiments are constructed around this approach: (1) isolated MWCNT cantilevers are subjected to a controlled deflection to measure the bending stiffness and demonstrate simple adhesion; (2) pairs of MWCNTs, assembled into an open chain, are subjected to a controlled displacement to observe the static and dynamic response of the constraining joint between them; (3) three MWCNTs, assembled into a closed chain, are subjected to a controlled displacement to observe the behavior of a multi-adhesive joint mechanism.

Each experimental set builds upon the knowledge gathered from the previous experiment. By investigating a single isolated structure, its mechanical stiffness and material properties can be estimated using a calibrated micro-scale cantilever as a force sensor. This not only measures the structural characteristics of individual MWCNTs but it also allows the MWCNT to be used as a nano-scale calibrated force sensor for subsequent experiments. Next, by observing the deflection of flexible links in a nano-kinematic pair, an estimation of the contact mechanics between the structures can be made. Here, the elastic and inelastic behavior of the adhesive joint is measured by observing its ability to bend the calibrated MWCNT links. Finally, this knowledge is expanded to investigate the elastic behavior of a multi-link, multiple-adhesive-joint MWCNT mechanism by observing the deflection of the calibrated MWCNT links and comparing the behavior of the joints as group to those individually observed previously. The understanding gathered from these experiments regarding the mechanics and kinematics of nanomanipulation may enable the advancement of dexterous manipulation for the purposes of nano-assembly. These experiments and their findings are reported in the following five sections: experimental principles and background, investigation of isolated nano-structures, investigation of nano kinematic pairs, investigation of a nano four-bar mechanism, and discussion and conclusions.

3.1 Experimental Principles and Background

Measuring the deflection of a beam subjected to an applied load is a simple, reliable method used in the study of structural and material properties. This approach is used throughout this work to study the mechanics and kinematics of nanomanipulation. Here, the forces and displacements are of the nanonewton and nanometer scale. To measure the forces present when deflecting nanoscopic structures, micro- and nano-scale cantilevers are calibrated for use as force sensors. The use of a calibrated cantilever to investigate the properties of an unknown beam—and in this study, the joint between multiple beams—is complicated at the nano-scale by adhesion. Therefore, a brief overview of adhesion and its implications in nanomanipulation is given to further support the experimental design.

3.1.1 Adhesion

Adhesive contact refers to the propensity of solid bodies to stick together without the aid of chemical binding agents (i.e. dry adhesion). This is caused by weak intermolecular forces (van der Waals interactions) working to deform bodies in contact so as to minimize the total energy of the system. Three primary descriptions of adhesive contact are reported in literature: Johnson-Kendall-Roberts (JKR) [32], Maugis-Dugdale (M-D) [117], and Derjaguin-Muller-Toporov (DMT) [118]. These models are complimentary and exist on a continuum as described by Tabor [119]. This continuum is defined by the ratio of the surface energies to the reduced elastic modulus when considering particles of the same size. The JKR model is applicable for relatively soft bodies with high surface energy while the reverse is true for use of the DMT model, and M-D occupies the transition in-between [33]. These models describe the total area of contact between nano-scale bodies in addition to the force necessary to separate them as illustrated in Figure 3.1. Here r is the radial position along the contact plane, R is the radius of the particle, a is the contact radius, c is the radius of influence beyond a for the DMT model, δ is the depth of penetration, and $P(r)$ is the pressure distribution between the two bodies as a function of the radius.

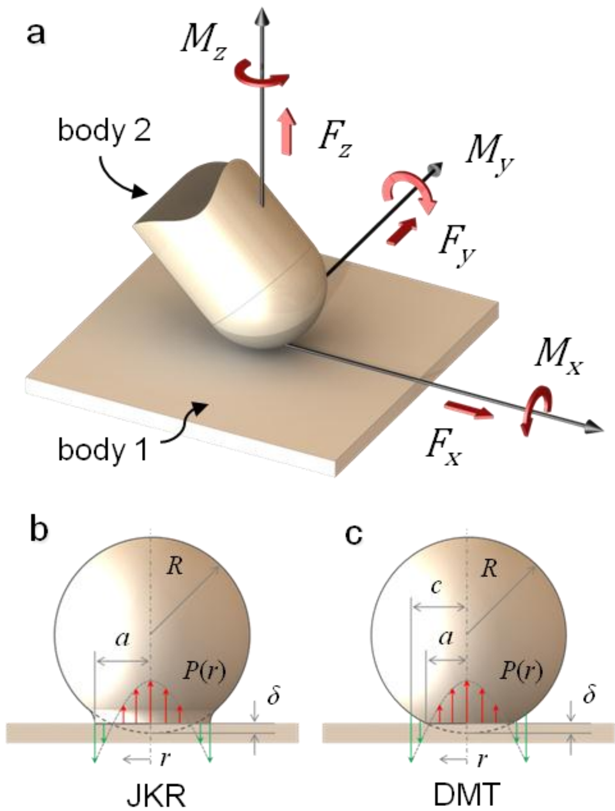

Figure 3.1: Adhesion contact between two bodies where a) shows an adhesive contact's resistance to applied forces along and about each axis, b) shows a diagram of the JKR model for adhesion, and c) shows the DMT model for adhesion

Adhesive contact has important implications for nanomanipulation; primarily the contact's ability to naturally resist motion due to externally applied forces as illustrated in Figure 3.1*a*. This is because it is energetically favorable for the bodies to resist a change in the contact area. However, this resistance is finite and—beyond a specific threshold—inelastic relative motion between the bodies is possible with respect to all six spatial degrees of freedom. Understanding this dual behavior is necessary for dexterous nanomanipulation because the kinematic orientation between end-effectors and parts must change when implementing a dynamic grasp. In addition, the operation of nano-scale mechanisms constructed with such a system must also account for both regions of behavior; that is, the region where elastic stiction dominates and the region where inelastic slipping occurs.

3.1.2 Adhesive Joint

Mechanically, the relationship between two nano-scale bodies in contact can be described as a kinematic pair and can be classified based on the available relative motion, the mechanical constraint, and the nature of contact. This kinematic relationship represents a unique nano-scale 'joint'. While within the elastic regime, the available relative motion between bodies constrained by this joint includes: limited *rolling* along the surface, *turning,* about the contact area, and *displacement* both perpendicular and normal to the contact. While within the inelastic regime, the available relative motion includes a greater degree of *rolling* and *turning* in addition to *slipping/sliding* along each surface and *complete separation* of the contact. In practice, during nanomanipulation where grasping and releasing operations are required, this means that the joint does not reduce the degrees of freedom available to the links relative to one another. As such, the nature of the constraint is *nonholonomic*. For the purposes of planar nanomanipulation where contact is maintained, the joint still allows relative motion between the two bodies along the x and y directions and about the z axis. Once inelastic motion occurs the final relative position of the two bodies is path dependent, resulting in a hysteretic behavior regarding the location of the contact point. This is therefore a nonlinear, non-conservative, nonholonomic constraint. For MWCNTs it forms both a *higher pair*, in that the contact can move along the axis of each tube, and an *unclosed pair* in that contact is maintained by van der Waals interactions. For the experiments presented in this chapter, this formulation of the joint may be used to analyze the contact between the MWCNT and the micro-cantilever, as well as between multiple MWCNTs assembled into a kinematic chain. Many critical aspect of this joint can be illustrated by considering two nano-scale cylinders in contact.

MWCNT Kinematic Pairs: Observing multiple nanoscopic cylinders in contact presents an excellent opportunity to describe the nature of this nano-scale joint. Consider two flexible CNTs oriented perpendicularly to each another as illustrated in Figure 3.2 with one tube rigidly fixed to the substrate. When a system of forces is applied to tube 1 along the axis of tube 2, a resistive force present at the contact interface counteracts the system (*a.1*). This contact force can continue to resist inelastic motion up to a specific threshold and can result in observable deflection in tube 1 (*a.2*). Beyond this threshold, slipping and/or rolling can occur as the contact's equilibrium point translates a distance δs along the axis of tube 2. A similar pattern of events is evident when the system of forces applies a couple to tube 1 (*b.1*). As the couple is applied a resistive moment is present at the contact interface resulting in a deflection of tube 2 (*b.2*). Past the resistive threshold the relative orientation between the bodies begins to twist by $\delta\theta$ (*b.3*). Once the applied forces are removed after inelastic motion is induced, the relative position and orientation of the tubes does not return to the initial configuration; demonstrating the positional hysteresis previously described. By applying a controlled system of forces or displacements to tube 1, the thresholds between elastic (stiction) and inelastic (sliption) motion can be determined when the structural stiffness of tube 2 is known. This is the basic approach to experimental design employed in this chapter's second set of experiments.

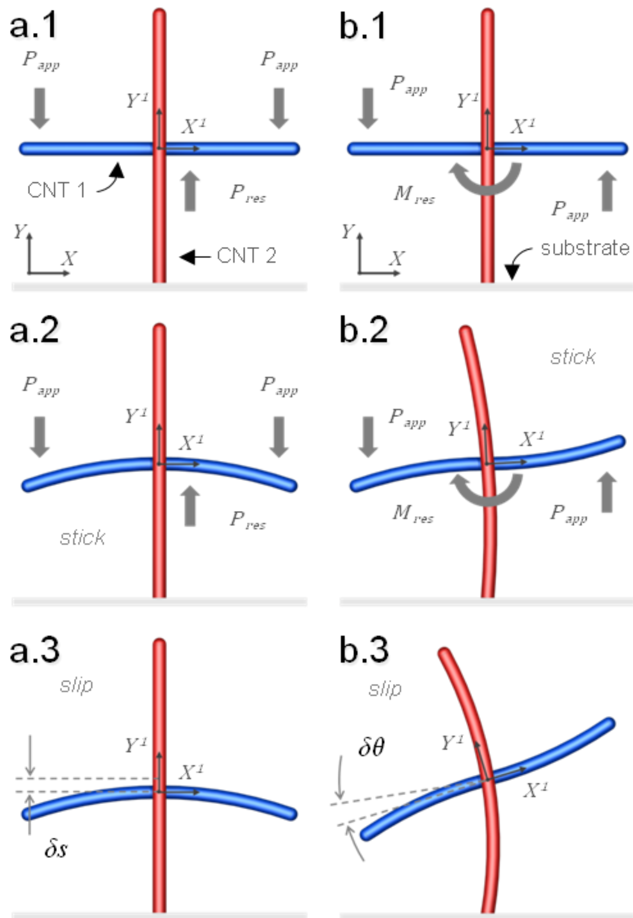

Figure 3.2: An illustration of the kinematics of a nanoscopic joint responding to a) an applied force and b) an applied couple

Contact Area: In applying this approach, it is also important to consider how the contact area changes as the relative orientation of the nanoscopic structures varies. It is the energetic favorability of this change that either resists or permits relative motion and defines the maximum force with which the joint can resist inelastic movement. This agrees with the observation that sub-millimeter-scale 'friction' differs in behavior from macro-scale friction in that it depends on the area of contact [116]. By applying adhesive contact theory to cylindrical geometries, the shape of the contact area can be shown to vary between a circle (for perpendicularly oriented bodies) and an approximate rectangle (for parallel bodies) as illustrated in Figure 3.3. Under special circumstances, the contact area between the cylinders can remain nearly constant if the over-lapping length in Figure 3.3*d* is small such that only the rounded ends of the rectangular contact area are present. However in general, this means that the nano-joint between cylindrical bodies can elastically resist larger applied forces and moments the closer the orientation is to parallel. Understanding how the position and orientation of bodies affect the behavior of a nano joint is required to predict the kinematic and kinetic behavior of these multibody nano systems.

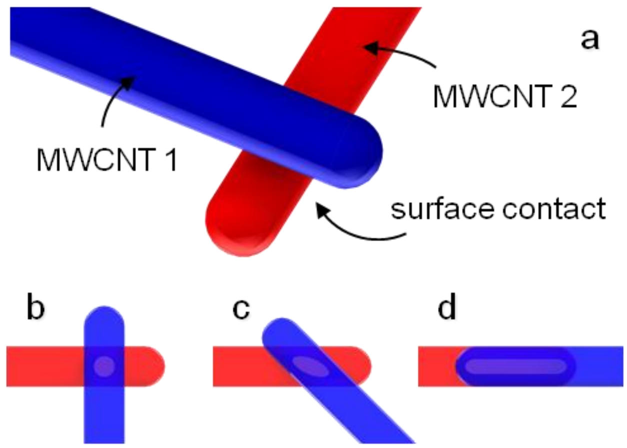

Figure 3.3: An illustration of the variable contact areas based on the orientation of the bodies where a) shows the relative spatial location of the bodies, b) shows circular contact area, c) shows the elliptical contact area, and d) shows the rectangular area

3.1.3 Experimental Overview

Applying the approach described in this section enables an understanding of not only the interaction between nano-scale structures being manipulated, but also between the structures and the end-effectors; ultimately facilitating the advancement of dynamic nano-scale grasps. Three experimental sets are presented in the following sections, designed to pursue this understanding. The first investigates the mechanical stiffness of select MWCNTs from the sample described in Chapter 2. These calibrated tubes are then used in the second investigation to determine the nano-joint's threshold between the stick and slip regions. This investigation also explores means by which to alter the joint's threshold. Finally, the last investigation studies the ability to transmit an applied force through multiple nano-joints within a nanoscopic mechanism. This represents the first steps toward a systematic understanding of nanoscopic multibody dynamics for use in automated dexterous nanomanipulation and assembly.

Prior to reporting these results, it is important to explain the method used for determining the measurement errors in each experimental group. The method follows that of [122] where δx_{total} is the total uncertainty in the measurement and is a function of δx_{random} and $\delta x_{\text{systemic}}$. Here δx_{random} refers to the statistical distribution of the results while $\delta x_{\text{systemic}}$ refers to the propagation of the measurement uncertainty in each piece of equipment throughout any analytical calculations performed. The values of δx_{random} and $\delta x_{\text{systemic}}$ are combined in quadrature to yield δx_{total}.

3.2 Experiment 1: Isolated Nano-Structures

The first experimental set seeks to determine the mechanical response of nanoscopic structures to applied forces. This is accomplished by observing the deflection, δ, of a MWCNT cantilever subject to a distributed load, P, applied near its free end by a calibrated micro-scale cantilever. From this, the structural stiffness, k, as well as an estimate for the elastic modulus, E, can be calculated using Equation (3.1). These tests also demonstrate how nano-scale adhesion alters the mechanical loading configuration of the beam bending experiment by changing the boundary conditions. This allows the maximum separation or pull-off force, P_{adh}, between the MWCNT and the end-effector to be measured using the same experimental setup.

$$k = k(E, I, L) = \frac{P}{\delta} \tag{3.1}$$

3.2.1 Material Description

Ten MWCNTs are chosen from the sparse, vertically-aligned array described in Chapter 2 based on their relative length, uniformity, and isolation. All ten are grown in the same local region on the array, covering an area of approximately 25 by 250 μm^2. Geometrically, all of the tubes feature tapered inner and outer walls with thin graphitized structures protruding into the internal void. These protrusions are a fraction of the thickness of the primary outer wall with considerable volume separating them. They are therefore assumed to play a negligible role in the stiffness of the structure. Accordingly, each tube is modeled as a hollow cylinder with linearly varying inner and outer radii. The characteristic dimensions of this geometric model are the length, L, the inner and outer radii at the base, R_i and R_o, and the slope of inner and outer walls, α_i and α_o.

Scanning and transmission electron microscopes (SEM and TEM) are used to measure the critical dimensions of the tubes. External dimensions of the ten tubes are measured using the SEM and are listed in Table 3.1. From these values the outer radius, R_o, and outer wall slope, α_o, are calculated. General internal dimensions are measured using the TEM. Due to the destructive nature of the TEM sample preparation procedure, these values are measured from generic tubes grown in a region 4 mm away from the ten primary tubes. These measurements yield the wall thickness at the tip near the catalyst (9.2 ± 1.4 nm) and the ratio of the inner diameter to the outer diameter at the base (75 ± 9 %). The values for the inner radius, R_i, and inner wall slope, α_i, are estimated from these measurements. In all, the structural dimensions of the ten samples span three orders of magnitude with an average length of 11.17 μm, an average outer radius at the base of 210 nm, and an average smallest dimension of 9 nm for the wall thickness at the tip.

Table 3.1: Measured external geometry of MWCNTs used in this study

CNT	L_{total}	$d_{o,base}$	$d_{o,tip}$
[-]	[μm]	[μm]	[μm]
1	10.420 ± 0.120	0.377 ± 0.052	0.222 ± 0.050
2	10.890 ± 0.059	0.360 ± 0.051	0.236 ± 0.056
3	11.820 ± 0.059	0.567 ± 0.050	0.352 ± 0.053
4	12.120 ± 0.065	0.509 ± 0.056	0.317 ± 0.059
5	9.945 ± 0.083	0.402 ± 0.052	0.232 ± 0.051
6	11.060 ± 0.058	0.327 ± 0.049	0.233 ± 0.051
7	11.510 ± 0.082	0.390 ± 0.053	0.272 ± 0.052
8	11.340 ± 0.098	0.458 ± 0.065	0.300 ± 0.051
9	10.930 ± 0.077	0.427 ± 0.052	0.255 ± 0.049
10	11.630 ± 0.076	0.387 ± 0.050	0.253 ± 0.047

3.2.2 Continuum Model at the Nano Scale

Modeling the structure as a cantilever with a solid wall implies the use of continuum mechanics. While many works have utilized continuum mechanics in analyzing or reporting the mechanical behavior of carbon nanotubes [123–132], the limits of the model must be noted. Material properties such as elastic modulus (Young's modulus) and structural measurements such as stress (force per unit area) assume that parameters including *area* are readily defined. This assumption has leaded to discrepancies in the material values reported in literature. For example, there is a general consensus on the structural stiffness of SWCNTs [123] (i.e. Eh where h is the wall thickness) but there remains disagreement on the value for the elastic modulus. Additionally, it has been experimentally observed that as the diameter of both SWCNTs and MWCNTs increase, the value for Eh appears to change, indicating that the reported E may not be an independent material property [124].

To address these discrepancies, the assumptions used in deriving the continuum beam model have been examined as they apply to the CNT structure [133, 134]. For parallel-wall MWCNTs it has been shown that a minimum of 202 nested shells (walls) are required to validate the continuum cross-section hypothesis to within a 1% error. With the smallest possible inner diameter of a MWCNT being 0.4 nm [135] and assuming a shell spacing of 0.34 nm [123], the minimum outer diameter of a MWCNT that satisfies the continuum assumption is approximately 135 nm. However, all of the reported experimental data known to the author on the elastic modulus of MWCNTs study tubes with a diameter less than 100 nm and show considerable dependence on the tube diameter [126–132]. With the thin nature of the CNT walls used in this work, the structures do not satisfy the continuum cross-section hypothesis. It is therefore unknown how the stresses are distributed through the structure's cross-section when bending the CNT.

To investigate the extent to which the continuum model can still be applied at this scale, the beam deflection equations are derived for the simplified MWCNT geometry described. This is with the aim of comparing the analytical deflected beam shape to that observed during experimentation and with the goal of comparing the calculated values for E between tubes. Since the cross-section assumption is not validated, E will be referred to as the pseudo-elastic modulus, E_{pse}, in recognition of the fact that this is a structurally dependent constant and not a material property in the classic definition.

3.2.3 Boundary and Loading Conditions for Nano Beams

Adhesion between the MWCNT and the micro-cantilever alters the boundary conditions of the beam as the load is applied. An illustration of the experimental configuration is given in Figure 3.4 where a calibrated cantilever (Beam 1) is used to determine the stiffness of an unknown softer beam (Beam 2) by applying a lateral force near the tip of the beam. The difference between performing this procedure using macroscopic and nanoscopic components is illustrated at each stage of motion: forward, center (equilibrium), and backward. At the macro-scale, beam 1 applies a point load to beam 2 near its tip as it moves in the forward direction (*a.1*) while it applies no load to beam 2 as it moves in the reverse direction (*a.3*). However, at the nano-scale, beam 1 applies a distributed load to beam 2 as it moves forward causing the beam to both deflect and rotate at the tip (*b.1*). Additionally, beam 1 applies a similar distributed load to beam 2 as it moves backwards (*b.3*).

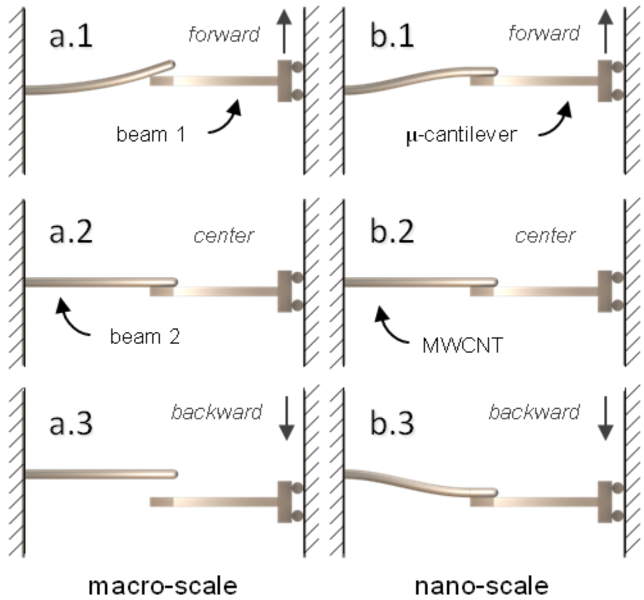

Figure 3.4: The loading configuraiton and operational differences between similar set-ups at a) the macro-scale and b) the nano-scale where beam 1 is much more stiff than beam 2.

At the nano-scale there are limits to this unique behavior. Beyond a certain point as Beam 1 moves in the forward direction, the adhesive contact can no longer hold onto the tip of Beam 2 and the arrangement reverts from that shown in (*b.1*) back to that shown in (*a.1*). Likewise, at a certain point in the reverse direction the adhesive contact releases and the arrangement reverts from that shown in (*b*.3) back to that shown in (*a.3*). Determining where these changes occur is necessary for specifying the boundary conditions in the beam equations. This is accomplished by analyzing the work of adhesion over Beam 2's range of motion. Assume for generality, that the stiffness of Beam 2 is a function of its displacement, $k\big(y(x)\big)$ and that it is deflected by a force applied to the tip of Beam 1 by a distance δ. The total work in bending Beam 2 is then:

$$W_b = \int_0^{\delta} -k(s)s\,ds = \int_0^{\delta} P(s)\,ds \tag{3.2}$$

The stiffness, $k(y)$ is a function of the boundary conditions used to derive $y(x)$ and as such is different for the macro and micro-scale cases illustrated in Figure 3.4. By comparing the work of bending between the two cases (macro/micro) for each of the three stages (forward/center/backward) the work of adhesion can be determined:

$$W_{adh} = W_{b,nano} - W_{b,macro} \tag{3.3}$$

Differentiating W_{adh} with respect to the deflection distance δ yields the total force applied to the contact area by adhesion:

$$P_{adh} = \frac{d}{d\delta}(W_{adh}) \tag{3.4}$$

For motion in the backward direction, this means that $W_{b,macro} \to 0$ and all of the work is performed by the adhesive contact. In contrast, for motion in the forward direction $W_{b,macro} \neq 0$ and the work performed by adhesion is a fraction of that used to bend the beam. In this way the maximum adhesive can be determined by bending Beam 2 in the backward direction until release occurs. As long as the force of adhesion in the forward direction is below this maximum value, then it is possible to assume that the nano-scale boundary condition shown in Figure 3.4*b.1* will hold.

The Euler-Bernoulli beam equation is not readily available for a hollow cylindrical cantilever with variable inner and outer radii. Nor is it available with the adhesive boundary condition just described. Hence, the equation is derived symbolically using the following procedure in Mathematica. In this model, the variable cross-section of the beam is described using the characteristic dimensions, yielding:

$$I(x) = \frac{\pi}{4}((R_o + \alpha_o x)^4 - (R_i + \alpha_i x)^4) \tag{3.5}$$

where $I(x)$ is the beam's second moment of inertia as a function of the distance, x, along its undeflected length, R_o and R_i are the outer and inner radii of the beam at the base, and α_o and α_i are the slopes of the outer and inner walls. The Euler-Bernoulli equation for a variable cross-section beam is:

$$I(x)y''''(x) + 2I'(x)y'''(x) + I''(x)y''(x) = 0 \tag{3.6}$$

with Equations (3.7) through (3.11) describing the equilibrium, and boundary conditions:

$$EI(x)y'''(x) + EI'(x)y''(x) + P = 0, \quad x \to L \tag{3.7}$$

$$EI(x)y''(x) + P(x - L) - M = 0, \quad x \to L \tag{3.8}$$

$$y'(x) = 0, \quad x \to L \tag{3.9}$$

$$y'(x) = 0, \quad x \to 0 \tag{3.10}$$

$$y(x) = 0, \quad x \to 0 \tag{3.11}$$

where E is the pseudo elastic modulus, $y(x)$ is the beam deflection, P is the laterally applied force, L is the distance along the beam where P is applied, and M is the constraint moment. The value of M is solved for using Equation (3.8) where the slope at the tip is fixed. Solving this system of equations for $y(x)$ gives an equation in terms of the applied force P. The basic geometry and sign conventions are illustrated in Figure 3.5.

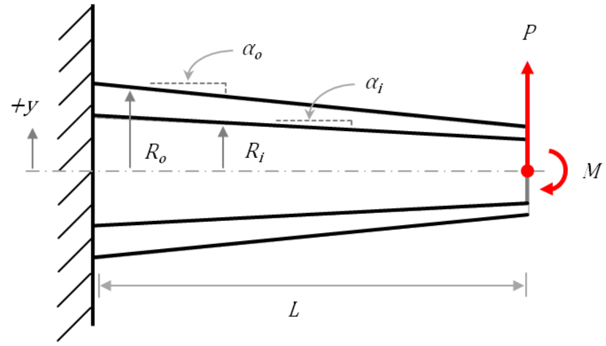

Figure 3.5: The geometry and sign conventions used in deriving the MWCNT beam bending equation

The explicit form of $y(x)$ involves a considerable number of terms and so is given in the appendix. From this equation, expressions for $k(P,\delta)$, $E(k)$, $P(E,\delta)$, and $P_{adh}(E,\delta)$ can be derived. To illustrate the large effect adhesion has on the force required to bend the cantilever, the limits of $P(E,\delta)$ and $P_{adh}(E,\delta)$ are given below where $\alpha_i \rightarrow 0$, $\alpha_o \rightarrow 0$, and $R_i \rightarrow 0$:

$$P = \frac{12EI\delta}{L^3} \tag{3.12}$$

$$P_{adh} = \frac{9EI\delta}{L^3} \tag{3.13}$$

Equations (3.12) and (3.13) show that for the stages in which the adhesive contact hold, a large fraction of the force exerted in deforming the beam results from adhesion. Through the use of these equations, the response of the MWCNT to an applied load can be analyzed.

3.2.4 Nanonewton Force Sensor

Evaluation of $k = k(P,\delta)$ requires knowing the applied force, P, and therefore the bending stiffness of the calibrated cantilever, Beam 1. The Arrow TL1Au tip-less micro-probe described in Chapter 2 is used as Beam 1 and it has a manufacturer's reported stiffness of $k = 0.03\ (+0.51, -0.026)$ N/m. While the stiffness is in the desired range, the uncertainty is too large for accurately measuring the k of MWCNTs. Hence, the stiffness of the micro-cantilever is determined in lab to narrow the measurement uncertainty.

Calibration is performed by observing the micro-cantilever's dynamic response when subjected to forced oscillation in air [136]. This method determines the spring constant by determining the first fundamental frequency of the cantilever, the quality factor in fluid (air), and the beam’s plan view dimensions. This experimental method is chosen over others that require greater knowledge of the geometry and material properties of the cantilever (e.g. layer thicknesses and material densities) because of its reduced expense and complexity and the smaller resulting uncertainties in the final value for k. The explicit expression for the bending stiffness is:

$$k = 0.1906\rho_f b^2 L Q_f \Gamma_i(\omega_f)\omega_f^2 \tag{3.14}$$

where ρ_f is the density of the fluid (air), b is the width of the cantilever, L is the length of the cantilever, Q_f is the quality factor in fluid, ω_f is the resonant frequency in fluid, and Γ_i is the imaginary component of the hydrodynamic function given in [137]. For the Arrow TL1Au with its triangular tip, L is replaced by L_{eff} which accounts for the reduction in mass by determining the length of an equivalent rectangular beam with the same width, b, and thickness, t.

$$L_{eff} = \frac{2}{L_{rec} + \frac{1}{2}L_{tri}}\left(\frac{1}{2}L_{rec}^2 + \frac{1}{2}L_{tri}\left(L_{rec} + \frac{1}{3}L_{tri}\right)\right) \tag{3.15}$$

where L_{rec} is the length of the rectangular portion of the beam and L_{tri} is the length of the triangular portion of the beam.

The natural frequencies of the micro-cantilever force sensor are experimentally measured using a Polytec MSV-400 scanning laser vibrometer. For this measurement, the cantilever, while firmly attached to a

Mini Smart Shaker (The Modal Shop, K2004E01) and positioned under the vibrometer, is vibrated through frequencies near the beam's first mode (3–8.75 kHz). The environmental conditions are also measured using a digital psychrometer (Extech, RH300) to determine the state of the fluid (air). The plan view of the beam is captured using the same optical microscope system used throughout this work. The measured frequency response of the cantilever over ten runs is shown in Figure 3.6 while the pertinent values for evaluating Equations (3.13) and (3.14) are listed in Table 3.2. The resulting measured stiffness for the Arrow TL1Au tip used in these experiments is 3.05 ± 0.07 mN/m.

Table 3.2: Measured values used to calculate the micro-cantilever beam stiffness used as the force sensor

	$\bar{x} \pm \delta x_{total}$	
ω_f	4874.2 ± 6.9	[Hz]
Q_f	26.214 ± 0.053	[-]
L	499.3 ± 2.1	[μm]
L_{rec}	418.1 ± 2.1	[μm]
b	94.9 ± 0.9	[μm]
T	26.3 ± 1.0	[°C]
RH	13.1 ± 3.0	[%]
p	102.201 ± 0.034	[kPa]

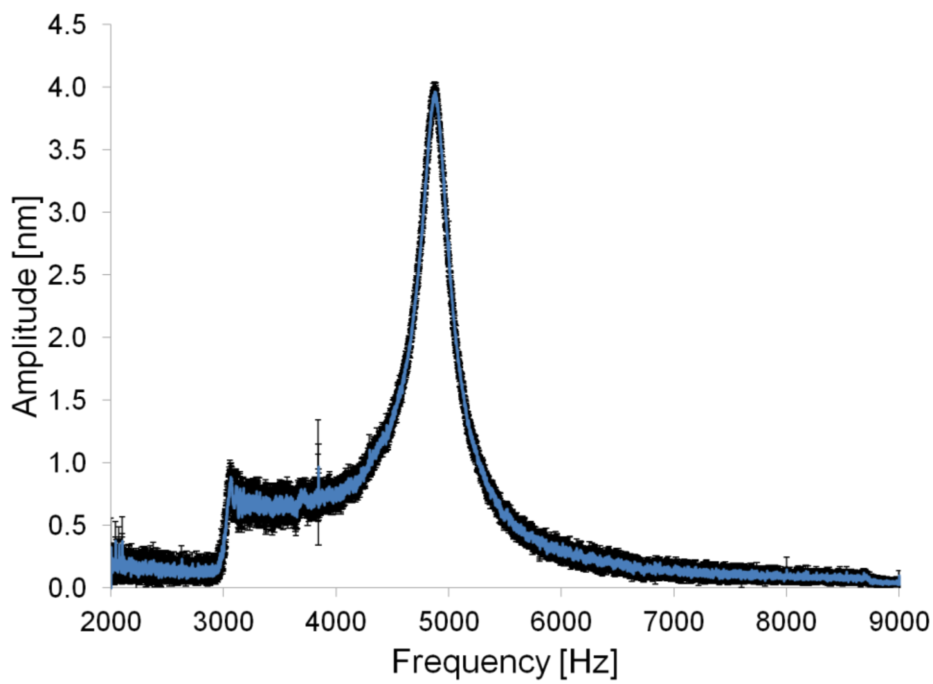

Figure 3.6: Measured frequency response of the micro-cantilever force sensor to forced oscillation in air

3.2.5 Experiment 1: Procedures

Experiment Set 1 is separated into three procedures. Procedure 1 measures the bending stiffness of the MWCNT under small deflection. This is used to evaluate the beam equation and estimate the pseudo-elastic modulus. Procedure 2 measures the maximum adhesive force between the MWCNT and the micro-cantilever force sensor. This is used to determine the boundary conditions when analyzing the beam deflection. Procedure 3 demonstrates each stage of the bending process during motion of the cantilever toward the MWCNT. Together, Procedure 2 and Procedure 3 demonstrate the transitions between each stage in the bending process which are defined by the various boundary conditions previously described. To facilitate the description of each procedure, the experimental configuration, bending stages, and experimental variables are illustrated in Figure 3.7

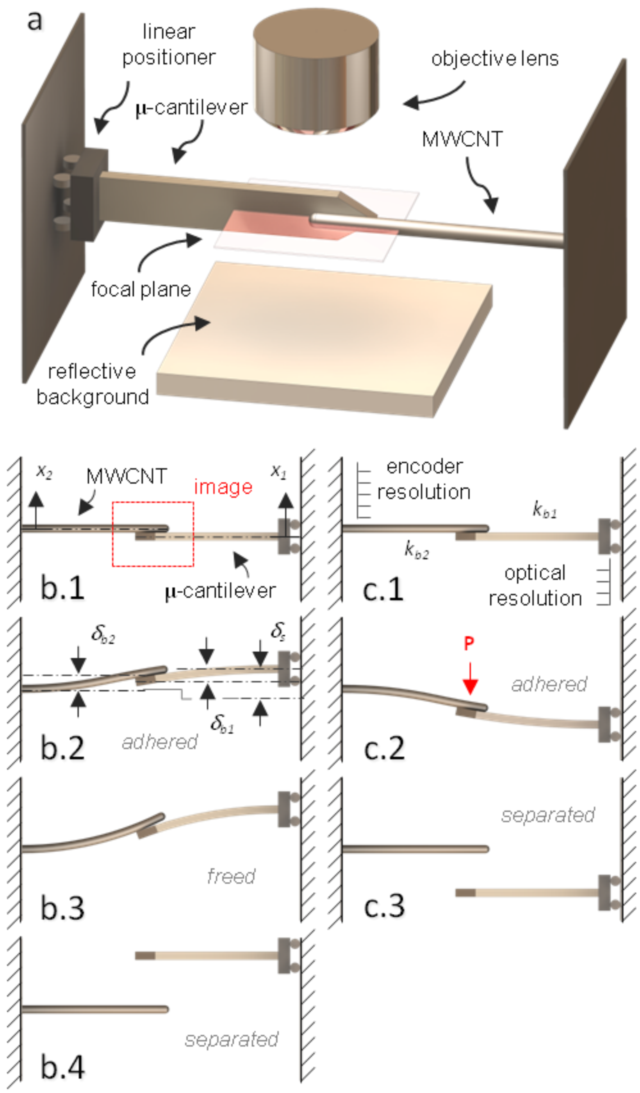

Figure 3.7: Schematics of the experimental approach where a cantilever of known properties is used to determine those of an unknown cantilever, showing a) the set-up, b) response during forward motion, and c) response during backward motion

In Experiment Set 1 there are two primary variables of interest: δ_{b1}, the displacement of the micro-cantilever from the starting datum at $x_1 = 0$, and δ_{b2}, the displacement of the MWCNT from its starting datum at $x_2 = 0$. These datums are coincident with the base of their respective beams at the initial point of contact. In the experimental analysis, these values are used in conjunction with the known stiffness of Beam 1, k_{b1}, to calculate k_{b2}, E_{pse}, and $P_{adh,max}$. The experimental design is given in Table 3.3.

Table 3.3: Design of Experimental Set 1

	Variables						
	Controlled				Independent		Dependent
Factors	electrostatic charge	pressure	position y_{b1}	position z_{b1}	humidity	displacement δ_s	position δ_{b2}
	[C]	[Pa]	[µm]	[µm]	[%RH]	[µm]	[µm]
Levels	negligible	ambient	8.00	0.00	5% (N_2)	-20.00	procedure 1
					40% (air)	$\delta_{b2} = +0.80$	procedure 2
						+20.00	procedure 3

All three procedures use the same first four steps. Step one; the target MWCNT is located optically. Two; the cantilever tip is brought into the vicinity of the tube. Three; the location of the tip relative to the substrate (near the base of the tube) is determined. This is performed by advancing the tip towards the substrate in 80 nm increments while the sourcemeter applies a 3.5 V potential across the tip and substrate using a 100 nA current limit. Once the current limit is detected, the present location of the positioners is adopted as the position datum for the substrate, $y_{b1} = 0.00$ µm. Four; the datum for the undeflected location of the MWCNT tip ($x_{b1} = 0.00$ µm) is determined in a similar manner. The cantilever is raised a predetermined distance away from the substrate ($y_{b1} \rightarrow L$) and then advanced in 80 nm increments towards the tube with the electrical source on until the current limit is detected. Once contact has been detected, the electric potential is removed. Two additional steps are executed in each of the procedures.

Procedure 1: step five, from the datum x_{b1} the cantilever is moved toward the tube a distance δ_s, causing it to bend until the beam has deflected by the desired amount δ_{b2}. This is set at 10-15% of the y_{b1} (the distance between the substrate and the point at which the force is applied) so as to maintain a small maximum deflection angle for comparison with the analytic beam equation. Sixth, the cantilever is returned to the undeflected datum. Ten runs are performed on each of the ten tubes.

Procedure 2: step five, from the datum x_{b1} the cantilever is moved away from the tube a distance δ_s, causing it to bend until the stored elastic energy overcomes the energy of adhesion and the two beams separate. The MWCNT snaps back into its original shape and position without noticeable plastic deformation. Sixth, the cantilever is returned to the undeflected datum. Ten runs are performed on five of the tubes.

Procedure 3: step five, from the datum x_{b1} the cantilever is moved towards the tube a distance δ_s, causing it to bend until the cantilever passes over the tube entirely and the MWCNT returns into its original shape and position without noticeable plastic deformation. Sixth, the cantilever is returned to the undeflected datum following a path that does not contact the MWCNT again until the datum is reached (up-and-over). Ten runs are performed on the five of the tubes. Ten additional runs are performed using this procedure on one tube using 40% relative humidity to investigate the capillary effect.

3.2.6 Experiment 1: Results and Analysis

A series of in situ images captured during Procedures 1 - 3 is displayed in Figure 3.8 as a direct comparison to Figure 3.7. The images have been post-processed using Adobe Photoshop CS4 by converting the mode to Grayscale and applying the Smart Sharpen filter (Amount: 500%, Radius: 64.0 pixels) to show each stage of motion. Using these images in conjunction with the closed-loop position control system, direct measurements of δ_{b2} and δ_s are taken during each procedure. For Procedure 1 the raw values are listed in Table 3.4, from which the experimental analysis proceeds.

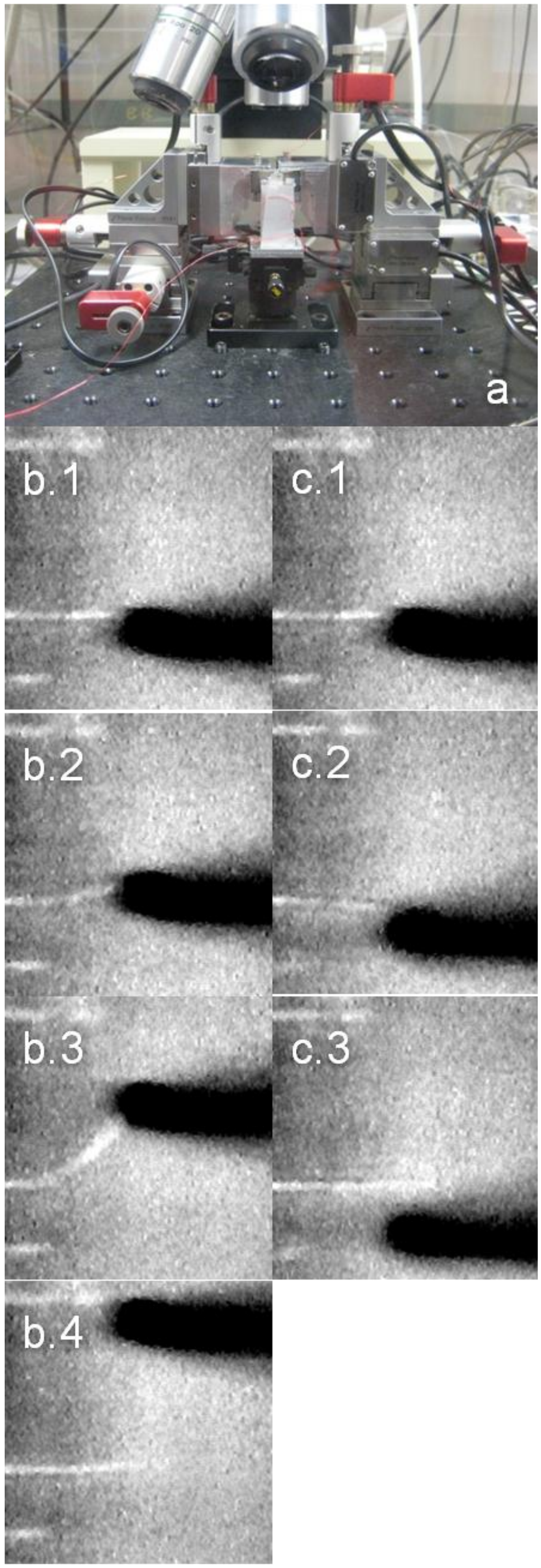

Figure 3.8: a) Photograph of the the experimental set-up, b) Optical images of the cantilever bending in the forward direction, c) the cantilever bending in the backward direction

Table 3.4: Raw data collected during Procedure 1

CNT	δ_s	δ_{b2}
[-]	[nm]	[nm]
1	2.11 ± 0.22 (0.22)	1.11 ± 0.09 (0.09)
2	2.38 ± 0.19 (0.18)	1.06 ± 0.08 (0.08)
3	4.49 ± 0.58 (0.57)	0.87 ± 0.21 (0.21)
4	6.01 ± 0.53 (0.50)	1.33 ± 0.24 (0.24)
5	2.52 ± 0.14 (0.12)	1.16 ± 0.10 (0.10)
6	2.05 ± 0.17 (0.16)	0.77 ± 0.09 (0.09)
7	1.82 ± 0.41 (0.41)	0.75 ± 0.18 (0.18)
8	2.42 ± 0.30 (0.29)	0.89 ± 0.13 (0.13)
9	2.35 ± 0.16 (0.14)	0.79 ± 0.08 (0.08)
10	1.83 ± 0.14 (0.13)	0.85 ± 0.09 (0.09)

Five assumptions are used in the analysis of the experiment:

1) The closest point of contact between the two beams will remain at the tip of b_1 throughout the motion of the beam.
2) While the beams remain adhered (stages *b.1* and *c.1*), the slope of b_1 and b_2 will be equivalent at the point of contact as b_1 moves in the $+x_1$ direction.
3) While b_1 moves in the $+x_1$ direction, its deflection (δ_{b1}) remains very small relative to the beam's length allowing the slope of b_1 to be considered constant (0 rad).
4) The adhesive force between b_1 and b_2 provides a lateral resistance to slipping that is much less than the force required to noticeably strain b_1 in the axial direction.
5) The adhesive force between b_1 and b_2 provides a lateral resistance to slipping that is much less than the force required to noticeably strain b_2 in the axial direction.

Analysis of Procedure 1 begins by calculating the force, P, applied to the MWCNT and its structural stiffness, k_{b2}. Given the MWCNT's deflection, δ_{b2}, and the micro-cantilever's commanded displacement, δ_s, the deflection of the micro-cantilever can be calculated:

$$\delta_{b1} = \delta_s - \delta_{b2} \tag{3.16}$$

Given δ_{b1}, the applied force is:

$$P = k_{b1}\delta_{b1} \tag{3.17}$$

Dividing Equation (3.17) by δ_{b2} yields the expression for the MWCNT's structural stiffness:

$$k_{b2} = \frac{k_{b1}(\delta_s - \delta_{b2})}{\delta_{b2}} = \frac{k_{b1}\delta_{b1}}{\delta_{b2}} \tag{3.18}$$

Complete analysis of Procedure 1 requires the preliminary results from Procedure 2. This is to determine which set of boundary conditions is applicable to the experimental runs in Procedure 1. The preliminary analysis is as follows. For the bending of the MWCNT in the forward direction to remain in the stage shown in Figure 3.7*b.2*, P_{adh} must be less than $P_{adh,max}$. Consider the analysis given in the discussion of Equations (3.2) – (3.4). There it is observed that all of the work performed in bending the MWCNT in the reverse direction is done by the adhesive contact while only a fraction of the work done in the forward direction is performed by the adhesive contact. This means that if the force applied while moving in the forward direction is less than or equal to the maximum force sustained in the reverse direction, the adhesive contact in the forward direction is postulated to hold. Since the applied force is proportional to δ_{b1} (Equation (3.17)), only the values of δ_{b1} need be compared so as to determine if the system remains in stage *b.2* during Procedure 1. This is indeed the case for the five runs performed in Procedure 2. These results are extrapolated to the remaining five MWCNTs. With the proper boundary conditions determined (full adhesive contact), evaluation of E_{pse} is performed. The results for k_{b2} and E_{pse} are given in Table 3.5.

Table 3.5: Bending stiffness and pseudo elastic modulus for ten MWCNTs. Errors posted in black are total uncertainties including random and systematic uncertainties. Errors in gray parentheses are random errors only.

CNT	k_{b2}	E_{pse}
[-]	[mN/m]	[Mpa]
1	2.8 ± 0.6 (0.6)	446 ± 658 (85)
2	3.8 ± 0.5 (0.5)	593 ± 923 (77)
3	13.1 ± 2.6 (2.5)	333 ± 339 (65)
4	11.2 ± 3.0 (2.9)	424 ± 508 (111)
5	3.6 ± 0.5 (0.5)	454 ± 729 (58)
6	5.1 ± 0.9 (0.8)	1051 ± 1669 (170)
7	4.4 ± 0.8 (0.7)	454 ± 649 (74)
8	5.4 ± 1.2 (1.2)	314 ± 477 (68)
9	6.0 ± 1.0 (0.9)	523 ± 713 (80)
10	3.6 ± 1.0 (1.0)	395 ± 541 (107)

Analysis of Procedure 1 shows an expected result where the wider MWCNTs have a higher stiffness (correlating Table 3.5 with Table 3.1). They also show notably small values for the pseudo elastic modulus, considering that the conservative estimate for a SWCNT's elastic modulus is 1 TPa [123].

To compare, consider an ideal cylindrical MWCNT with similar average dimensions to those used in this study. Let both the outer and inner radii be constant ($\alpha_o \to 0,\ \alpha_i \to 0$), the inner diameter be 10 nm, and the outer diameter be 342 nm. Note that this hypothetical MWCNT would satisfy the assumptions of continuum mechanics. The explicit equation for the stiffness becomes:

$$k = \frac{P}{y(L)} = \frac{3E\pi\left({R_o}^4 - {R_i}^4\right)}{L^3} \tag{3.19}$$

By choosing $E = 1$ TPa, k would be approximately 252 N/m for this idealized structure. Compared to the average 6.3 mN/m reported in Table 3.5, this is five orders of magnitude more stiff. Even with the high total uncertainty in the calculated value, the values for the elastic modulus do not approach the theoretical ideal. This is further exemplified by the graph presented in Figure 3.9 which compares the pseudo elastic modulus measured in this work to the elastic modulus of other, smaller MWCNT reported literature [126–

132]. The vertical red line represents the minimum outer diameter necessary to comply with the continuum cross-section hypothesis as described in Section 3.2.2. This minimum diameter assumes a thick, ordered wall for which the tubes in this study do not satisfy even though the outer diameters are quite large. This suggests that the thin, variable radii sidewalls and stacked-cone arrangement of these structures has a pronounced effect on the structure's mechanical characteristics.

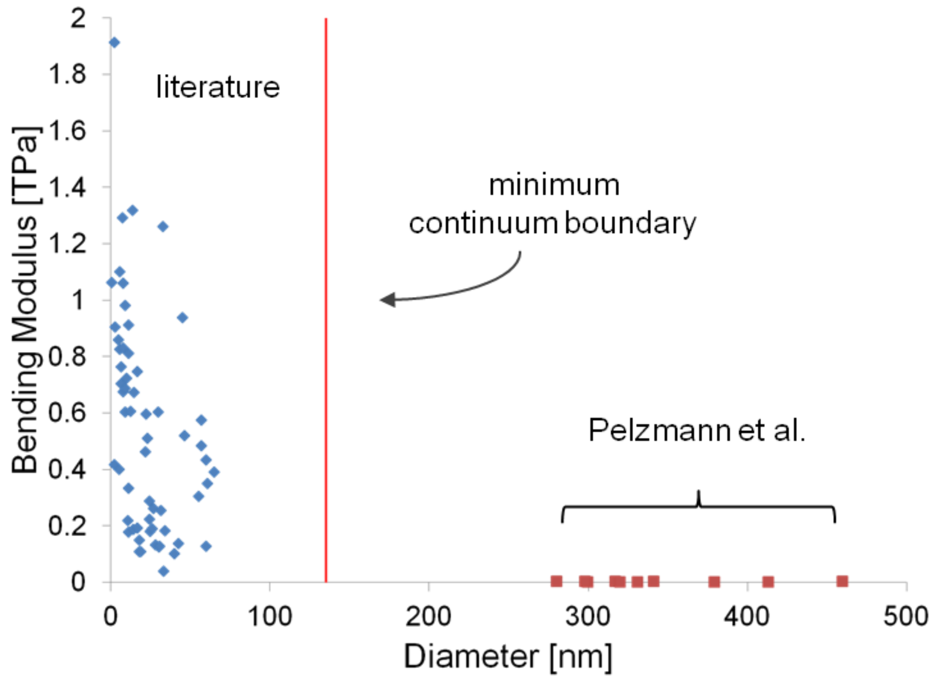

Figure 3.9: A comparison of the measured MWCNT modulus from various works.

While the large uncertainty makes inter-tube and material comparison difficult, the random errors (standard deviations shown in gray) of the raw measurements in Table 3.4 along with the analyzed values in Table 3.5 show that experimentation on the same tube is repeatable. The discrepancy between the random and total errors shown for E_{pse} in Table 3.5 is due to the beam equation's sensitivity to the large uncertainty in the tube's internal dimensions, α_i and R_i. However, by treating E_{pse} as a structural property of an individual tube instead of a general material property, the value proves useful in plotting the analytical shape of the deflected beam. In Figure 3.10, this analytical shape is compared to the recorded images of the deflected beam from Procedure 1. The measured value in the plot is produced using post processing in both Adobe Photoshop CS4 and Matlab. In Photoshop the images are converted to gray scale, manually cropped, rotated and the background removed, and then subjected to the Smart Sharpen Filter (Amount: 500%, Radius: 64.0 pixels). In Matlab the boarders of the tube are detected using the built-in *edge.m* function with the threshold value swept from 0 to 20. The centerline for each threshold value is determined and then averaged to produce the measured curve shown in the figure. The analytical shape is calculated using the dimensions of the tube, the average E_{pse} for the ten runs, and the average deflection. This shows that by employing E_{pse} a good correlation can be made between the theoretically predicted shape using continuum mechanics and the experimentally observed structure within the measurement capabilities of this system.

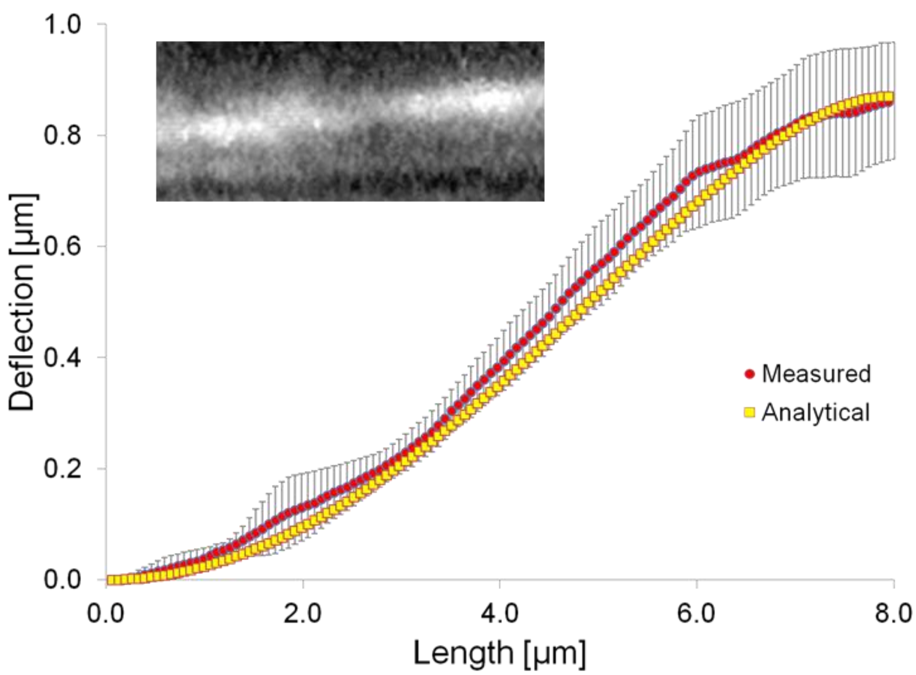

Figure 3.10: Deflected MWCNT shape for tube #8 where the measured curve represents the average centerline of 10 runs produced using Matlab and the analytical curce represents the continuum mechanics approximation

From the measurements and analysis performed during Procedure 1 it has been shown that: 1) the structural stiffness of the MWCNT is very low; 2) the pseudo-modulus of elasticity is similarly low relative to those reportedfor single walled and multiwalled CNTs; and 3) the pseudo-continuum expression for the deflection shape of the MWCNT closely matches that observed.

Analysis of Procedure 2 produces a quantitative comparison between the adhesive force present during motion in the forward and backward directions. This is the force of adhesion required to maintain the boundary condition moving forward as compared to the maximum force of adhesion measured moving backward. Application of Equation (3.4) results in the data listed in Table 3.6.

Table 3.6: Comparison of adhesive force calculated in Procedure 1 (P_{adh}) and the maximum adhesive force sustained by the contact area from Procedure 2 ($P_{adh,max}$)

CNT	P_{adh}	$P_{adh,max}$
[-]	[nN]	[nN]
1	1.9 ± 4.6 (0.4)	3.0 ± 1.0 (1.0)
2	2.6 ± 6.1 (0.3)	4.8 ± 0.7 (0.6)
4	9.2 ± 16.4 (0.9)	12.8 ± 1.3 (1.2)
5	2.5 ± 5.9 (0.2)	5.1 ± 1.0 (0.9)
9	3.0 ± 4.3 (0.3)	6.4 ± 0.5 (0.5)

The results show that the average value for P_{adh} is lower than the average for $P_{adh,max}$ for all MWCNTs tested. The total measurement uncertainty is again large for P_{adh} due to the use of $E = E(P, I, L, \delta)$ in the calculations which is sensitive to the uncertainty in α_i and R_i. In contrast, the standard deviation in the values of P_{adh} are notably smaller. The values for $P_{adh,max}$ do not show the same large systematic uncertainty because they are directly calculated from Equation (3.17). These results suggest, but do not prove, that the zero-tip-slope boundary condition is maintained for all runs. However, while the explicit calculation of these forces do not yield conclusive results, a conclusion can be drawn by using the analysis of δ_s previously given when examining Procedure 1. When comparing the two sets of runs (forward and backward) using only the deflection of the micro-cantilever, δ_s, it is observed that this value is always greater in the backward direction. This does strongly support the claim that the boundary condition is maintained.

In addition to analyzing the adhesion for its role in the boundary condition, the effect of the relative humidity in adhesion is analyzed briefly. Ten runs of Procedure 2 are performed on CNT #4 at 40% RH to investigate whether or not capillary effects in this range alter the maximum force of adhesion. The pull-off force $P_{adh,max}$ recorded under these conditions is 12.8 ± 0.7 (0.4) which aligns with the value shown in Table 3.5 for the same test at 5% RH. This agrees with the prediction that capillary effects only start to become evident at an RH above 54% [121] as discussed in Chapter 2.

Analysis of Procedure 3 produces a qualitative comparison of each stage in the bending process. This is performed for completeness, providing a record of the behavioral differences through all stages of motion in the forward and backward directions. As is evident from Figure 3.8, the shape of the beam exhibits an inflection point during both stages *b.2* and *c.2*. That point disappears in *b.3* as the MWCNT undergoes large deflection. Finally, in stage *b.4* the two beams separate, showing the notable elastic resilience of these MWCNTs.

To summarize the findings of Experiment Set 1: Procedure 1 demonstrates the low stiffness and pseudo elastic modulus measured for the MWCNTs used in this work. It also demonstrates that, while continuum mechanics cannot not be strictly applied to these nano-structures, their shape in bending is sufficiently approximated using the Euler-Bernoulli beam equation under specific conditions. Procedure 2 shows that the force of adhesion over the contact area is strong enough to maintain the boundary condition when performing Procedure 1, and offers suggestive quantitative measurements as additional support. It also shows that a relative humidity up to 40% does not measurably change the adhesion. Finally, Procedure 3 shows the difference between motion of the micro-cantilever in the forward direction and motion in the backward direction in all stages. It also shows that the MWCNTs in this work are capable of large elastic deformation. The experimental information gathered in Experiment Set 1 facilitates Experimental Set 2 and Set 3.

3.3 Experiment 2: Nano Kinematic Pairs

With the knowledge of the elastic behavior of the MWCNTs produced from Experiment Set 1, Experiment Set 2 studies the adhesive behavior of two MWCNTs assembled into a kinematic pair. This is accomplished by using the MWCNTs themselves as force sensors through apply the knowledge of their mechanical stiffness. In this manner, the maximum resistive force sustained by the adhesive contact, ϕ_{max}, can be estimated for both applied forces and moments. This defines the threshold between the nano-adhesive joint's two regions of behavior: elastic (stick) and inelastic (slip). In Experiment Set 2, slipping is used to further demonstrate the nature of contact, mechanical constraint, and available relative motion of the joint. This culminates in a demonstration of the nonlinear, energy-dissipative behavior of the constraint between the two MWCNTs. Additionally, the ability to alter this behavior by welding the CNTs together is examined; specifically, how the value of ϕ_{max} can be increased. Experiment Set 2 is divided into four procedures based on the relative orientation of the MWCNT links and the displacement applied to each. To facilitate the description of each procedure, the experimental configuration, relative link orientations, and applied displacements are illustrated in Figure 3.11.

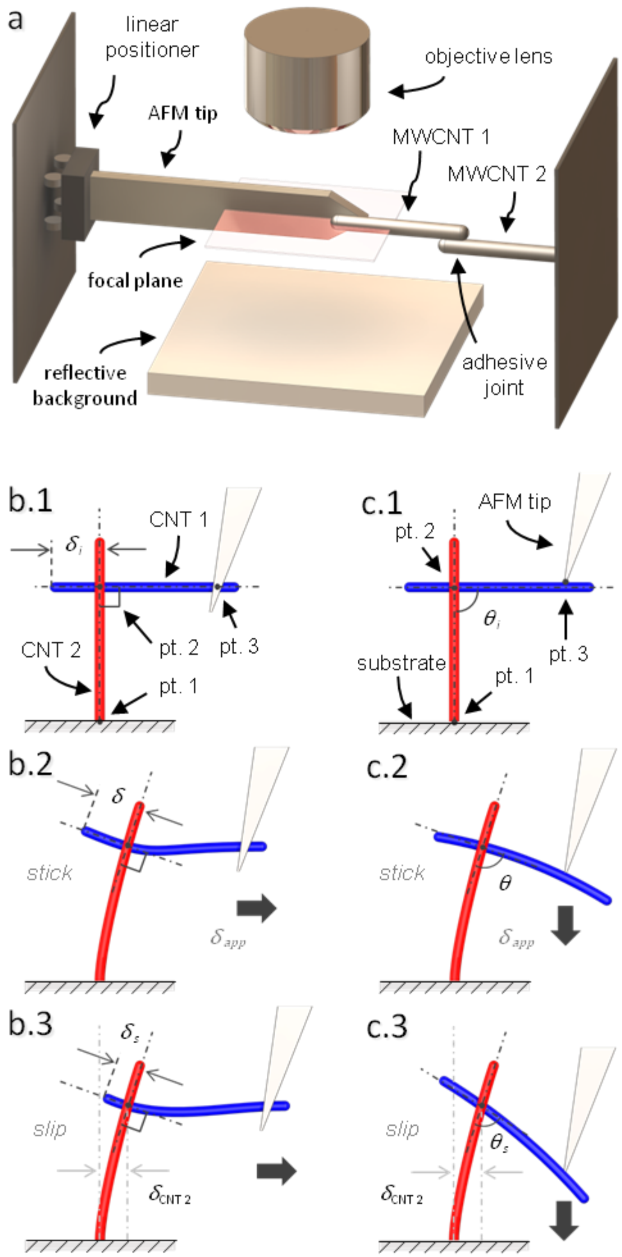

Figure 3.11: The experimental approach using two MWCNT cantilevers of known properties to determine the adhesive properties of their mutual contact with a) the set-up, b) an applied linear force, and c) an applied rotational force

3.3.1 Experiment 2: Procedures

In Experiment Set 2 the primary variable of interest is δ_{CNT2}, the displacement of the MWCNT fixed to the substrate from its equilibrium position. By examining δ_{CNT2} as CNT 1 is displaced, the force transmitted between the two bodies, ϕ, via the adhesive contact can be estimated. Observing this behavior for both applied forces and moments gives an initial understanding of the stability of the nano-adhesive joint. This gives a baseline from which methods of altering the region of stability can be examined, e.g. welding of the structures. The experimental design is given in Table 3.7.

Table 3.7: Design of Experiment Set 2

	Variables						
	Controlled			Independent			Dependent
Factors	electrostatic charge	pressure	humidity	pose	contact motion	contact state	position $\delta_{\mathrm{CNT\,2,\,max}}$
	[C]	[Pa]	%RH	[-]	[-]	[-]	[µm]
Levels	negligible	ambient	5 (welding)	$\perp$	linear	natural	procedure 1
			40 (pose)	$\parallel$	revolute	welded	procedure 2
							procedure 3
							procedure 4

Preparing each experimental procedure requires positioning and welding of the CNT structures. This involves the cutting of MWCNTs from the surface of the substrate, dexterous manipulation of the structures into position, and welding of the MWCNTs into place (either onto the end-effector or the contacting nanotube). Cutting and welding of MWCNTs is performed using direct Joule heating, following the work of [88]. In the cited work, multiple MWCNTs were assembled into free standing structures spelling the letters 'A T I' using dexterous manipulation inside an SEM and welded into position. While the bond was stated to be 'mechanically robust', the degree to which the links were bonded was not examined, nor was the contacts between the links and manipulators treated as kinematic joints. The following is a description of the cutting, manipulating, and welding processes used in this work.

Cutting is used to either reduce the length of the target MWCNT or to separate it from its current contacts. This is primarily used to remove the MWCNT from the substrate, as is illustrated in Figure 3.12. To cut, at least one end-effector is brought into contact with the MWCNT, giving two points of electrical contact to the tube. The polarities of contacts are assigned via the VI (+5.0V/Gnd) and the current limit of the sourcemeter is set 1.0 mA. Once power is supplied to the assembly, the Joule heating induced in the MWCNT quickly vaporizes the current-carrying section. The result is the CNT now adhered only to the end-effector.

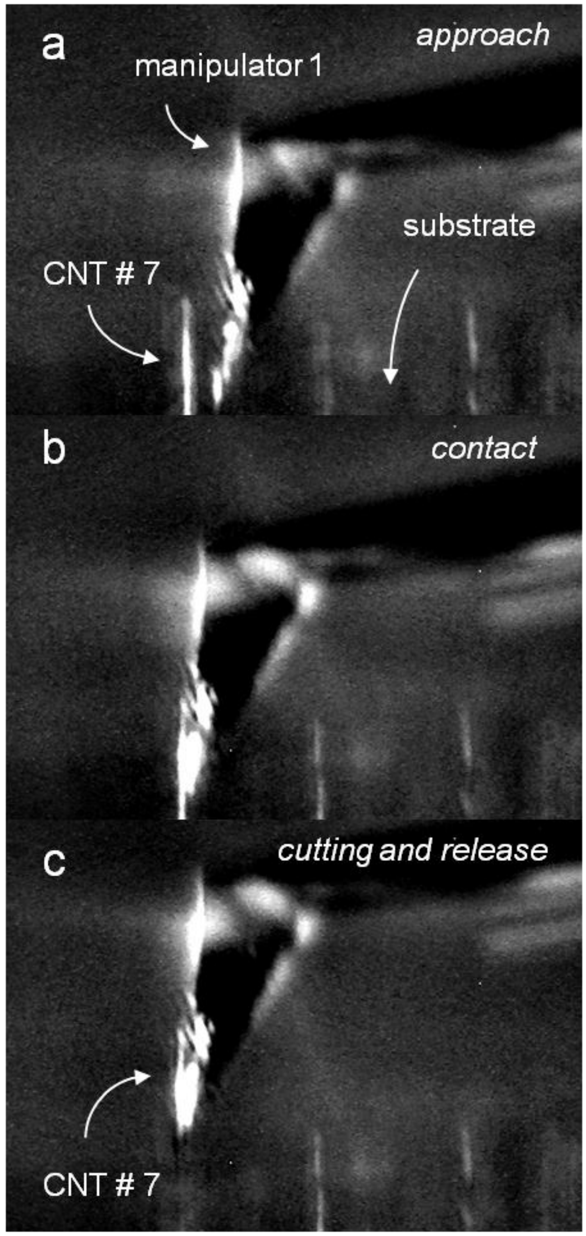

Figure 3.12: Image series showing the cutting process used to separate the MWCNT from the substrate

Dexterous manipulation is performed on the freed MWCNTs to orient them spatially as demonstrated in Figure 3.13. This is performed using coordinated motion of the two end-effectors in contact with the nanotube. Since the mechanical behavior of the contact is not robustly understood prior to this work, manipulation is performed intuitively by the operator using either numeric commands or a commercial gaming controller. The process is notably tedious but results in the MWCNTs being properly arranged for the purposes of this work.

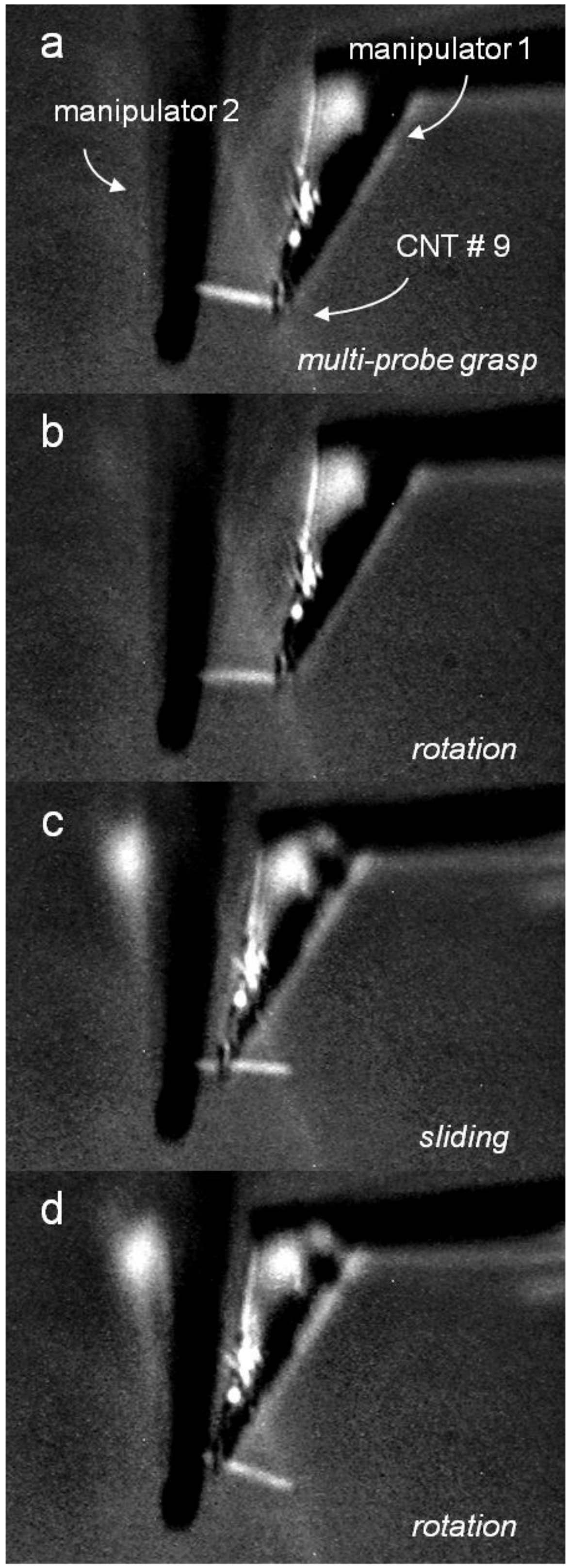

Figure 3.13: A series of images showing the dexterous manipulation of a MWCNT using two end-effectors

Welding is performed on the assembled MWCNT mechanism by applying a controlled potential across the structure while imposing a strict current limit. For MWCNT with smaller diameters, cycling the applied electric potential between $0 \rightarrow 5V$ with a $10\mu A$ current limit has shown successful welding when performed in a vacuum [88]. Performing welding in a vacuum—as opposed to in air— alters the means by which the nano-structure can dissipate heat as well as limits the gaseous elements surrounding the tube that might catalyze MWCNT degradation. Taking this into consideration, all welding processes are performed in a predominately nitrogen environment (5% RH) to minimize oxidation of the tubes during welding. For the larger diameter tubes in this work, a 5V with 130 μA limit has been sustained by the joint without loss of continuity. However, to minimize damage to the tubes, welding in this work is performed using the same potential and current limit (5V and 10 μA limit) reported in [88] with upwards of 15 power cycles. Complete vaporization of a tube—when the limit is not imposed—is demonstrated in Figure 3.14 for instructive purposes.

Due to the potentially high temperatures present during cutting and welding, along with mechanical damage resulting from contact, the probe tips degrade with use. The primary form of degradation is the loss of the conductive coating on the probe tips which alters the adhesion and inhibits electrical continuity. These regions are identified by observing the displacement of a MWCNT via probe contact while failing to establish electrical continuity across the MWCNT. Once a damaged region on a probe is observed, it is actively avoided during experimentation. If an exceedingly large surface area is deemed damaged, the probe is replaced. While damage was recorded on one dexterous probe tip due to welding, the extent never proved great enough to justify replacement. Together cutting, manipulating, and welding are the three primary processes used to prepare the samples for procedures 1-4.

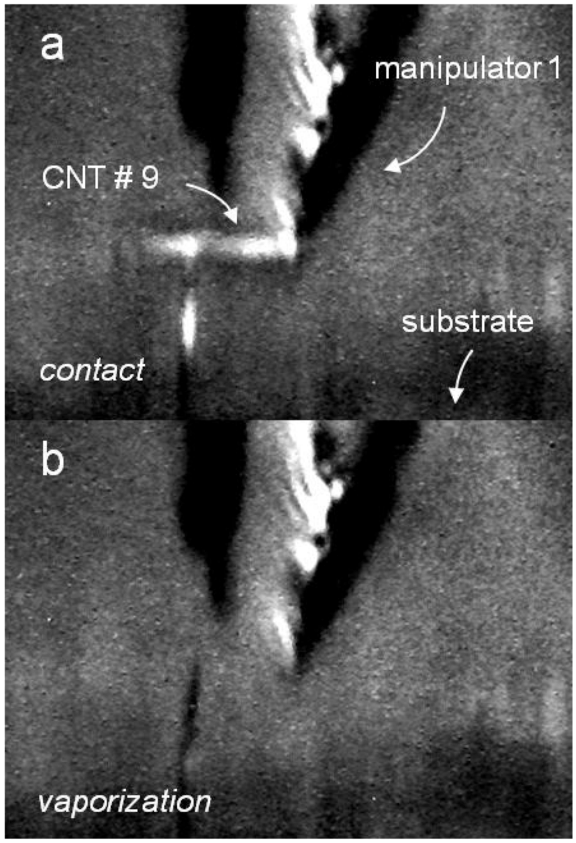

Figure 3.14: Image series showing the vaporization of a MWCNT using Joule heating

Procedure 1 investigates the nano-joint's response to a linearly applied force. It is designed to investigate the maximum force, ϕ_{max}, that the joint can sustain before inelastic motion between the nano-structures occurs. The experiment is separated into two sub procedures. Sub-Procedure 1.1 investigates the natural joint behavior caused purely by van der Waals force. Sub-Procedure 1.2 investigates the augmented joint behavior where the contact has been heat treated (welded) using Joule heating.

The experimental configuration includes the two MWCNTs in a perpendicular orientation as shown in Figure 3.11*b* which minimizes the shared surface area between the tubes when in contact. Motion of CNT 1 is controlled by attaching it to the end-effector of manipulator 1. To increase adhesion between CNT 1 and the end-effector, the contact region is situated away from the probe tip, increasing the total contact area and the associated adhesive force. After the components have been properly oriented, the procedure includes four steps. Step one; CNT 1 is situated in an xz plane not coincident with CNT 2. Step two; CNT 1 is moved along the x_1 direction behind CNT 2 until a portion of CNT 1, δ_i, extends beyond CNT 2. This ensures that when slipping initially occurs, contact is not lost. Step three, with the electrical continuity check system activated, CNT 1 is moved along z_2 until contact is detected. Once contact is made the electrical system is deactivated. Step four, CNT 1 is moved away from CNT 2 at a constant rate until the tubes separate entirely. In Procedure 1.1, steps one through four are repeated for ten runs.

For Procedure 1.2, steps one through three are maintained. In step four, the two tubes are subjected to ten power cycles of 5.0 V with a 10 µA current limit. Step five, CNT 1 is moved away from CNT 2 at a constant rate until the tubes separate entirely. Steps one through five are repeated for five runs.

Procedure 2 investigates the nano-joint's response to an applied moment. It is designed to investigate the maximum force, ϕ_{max}, that the joint can sustain before inelastic motion between the nano-structures occurs and is separated into two sub procedures. Similarly to Procedure 1, sub-Procedure 2.1 investigates the natural joint behavior caused purely by van der Waals force. Sub-Procedure 2.2 investigates the augmented joint behavior where the contact has been heat treated (welded) using Joule heating.

The experimental configuration includes the two MWCNTs in a perpendicular orientation as shown in Figure 3.11*c*. Motion of CNT 1 is controlled by attaching it to the end-effector of manipulator 1. Since pure rotational motion of CNT 1 around the contact with CNT 2 is desired, contact with the end-effector is minimized. This is to avoid the boundary condition observed in both Experiment Set 1 and Procedure 1 of Experiment Set 2 to the extent possible by minimizing the total contact area. Prior to the first step, CNT 1 is positioned on CNT 2 in the desired orientation. Step 1, the end-effector is moved 0.8 µm toward the substrate ($-y_1$ direction), causing CNT 1 to rotate about the contacts with CNT 2 and the end-effector. The small range of motion is maintained in an attempt to ensure the area of the contact ellipse does not undergo drastic change, increasing the contact's resistance to slipping. Step 2, the end-effector is moved 0.8 μm away from the substrate ($+y_1$ direction). Step 3, the end-effector is moved an additional distance away from the substrate so that the equilibrium orientation of the CNTs is reset to parallel relative to the substrate. Step 4, the end-effector is returned to the equilibrium position. In Procedure 2.1, steps one through four are repeated for ten runs.

Procedure 2.2 is identical to Procedure 2.1 except that step one is preceded by a step subjecting the CNT assembly to ten power cycles of 5.0 V with a 10 μA current limit. Steps one through five are then repeated for five runs.

Procedure 3 investigates the effect of the contact area's size on the nano-joint's response to an applied moment. This is performed with the two MWCNTs situated in a parallel orientation so that the area can be most effectively varied as illustrated in Figure 3.3. It is designed to investigate the maximum force, ϕ_{max}, that the joint can sustain before inelastic motion between the nano-structures occurs and is separated into three sub procedures. Similarly to Procedures 1 and 2, sub-Procedure 3.1 investigates the natural joint behavior caused purely by van der Waals force when the contact area is small. Sub-Procedure 3.2 investigates the augmented joint behavior where the contact has been heat treated (welded) using Joule heating. Procedure 3.3 re-positions the tubes so that the overlap area is larger and again investigates the natural joint behavior.

The experimental configuration includes the two MWCNTs in a parallel orientation as shown in Figure 3.11*a*. Motion of CNT 1 is controlled by attaching it to the end-effector of manipulator 1. Since pure rotational motion of CNT 1 around the contact with CNT 2 is again desired, contact with the end-effector is minimized. Prior to the first step, CNT 1 is positioned on CNT 2 in the desired orientation. Step 1, the end-effector is moved 0.8 μm along the substrate ($-x_1$ direction), causing CNT 1 to rotate about the contacts with CNT 2 and the end-effector. Step 2, the end-effector is moved 0.8 μm back along the substrate ($+x_1$ direction). Step 3, the end-effector is moved an additional distance away from the substrate so that the equilibrium orientation of the CNTs is reset to parallel. Step 4, the end-effector is returned to the equilibrium position. In Procedure 3.1, steps one through four are repeated for ten runs.

Procedure 3.2 is identical to Procedure 3.1 except that step one is preceded by a step subjecting the CNT assembly to ten power cycles of 5.0 V with a 10 μA current limit. Steps one through five are then repeated for five runs.

Procedure 3.3 is identical to Procedure 3.1 except that the initial orientation has a larger overlapping length between the two tubes. Steps one through four are then repeated for ten runs.

Procedure 4 investigates the nonlinear, energy-dissipative nature of the nano-joint when subjected to a linearly applied force. This includes studying the maximum force elastically sustained by the joint, ϕ_{max}, the elastic stiffness of the joint, k_c, and the hysteretic behavior of the contact's position.

The experimental configuration is identical to Procedure 1 and includes the two MWCNTs in a perpendicular orientation as shown in Figure 3.11*b* with a large area of contact between the end-effector and CNT 1. Motion of CNT 1 is controlled using manipulator 1. After the components have been properly oriented so that a large length of CNT 1 (δ_i) is initially positioned beyond CNT 2, the procedure includes two steps. Step one, the end-effector is moved in the $+x_1$ direction 2 μm. Step two, the end-effector is moved back 2 μm in the $-x_1$ direction.

3.3.2 Experiment 2: Results and Analysis

The primary variable measured and used for analysis in Experiment Set 2 is the deflection of CNT 2, $\delta_{\text{CNT 2}}$. This is due to CNT 2's role as the nano-scale force sensor used to detect the force transmitted between the MWCNTs by means of the adhesive contact. For Procedures 1, 2, and 3, CNT 1 is tube #7 as described in Table 3.1 and CNT 2 is tube #1. For Procedure 3, CNT 1 and CNT 2 are tubes #3 and #2 respectively. The recorded values for $\delta_{\text{CNT 2}}$ are listed in Table 3.8. Analysis of the nano-joint proceeds from these values.

Table 3.8: Raw data collected during Experiment Set 2

Proc.		Pose	Motion	Contact		Region	$L_{\text{CNT 2}}$	$\delta_{\text{CNT 2 max}}$
				Type	Area			
[-]		[-]	[-]	[-]	[-]	[-]	[μm]	[μm]
1	1.1	⊥	linear	natural	small	stick	7.14	0.38 ± 0.11 (0.11)
	1.2			welded				0.80 ± 0.23 (0.23)
2	2.1	⊥	revolute	natural	small	stick	6.47	0.09 ± 0.03 (0.03)
	2.2			welded				0.11 ± 0.06 (0.06)
3	3.1	∥	revolute	natural	small	stick	9.87	0.07 ± 0.02 (0.02)
	3.2			welded				0.14 ± 0.03 (0.03)
	3.3			natural	large		7.79	0.36 ± 0.05 (0.05)
4	4.1	⊥	linear	natural	small	slip	8.21	0.55 ± 0.01 (0.01)

Five assumptions are used in the analysis of Experiment Set 2:

1) During Procedure 1, the adhesion of CNT 1 to the end-effector of manipulator 1 is much stronger than the adhesion of CNT 1 to CNT 2, permitting no motion between the end-effector and CNT 1.
2) During Procedure 1, all inelastic motion occurs along the length of CNT 1, i.e. the contact between CNT 1 and CNT 2 undergoes no rotation, maintaining a relative orientation of $\pi/2$ rad.
3) During Procedure 2 and Procedure 3, the adhesion of CNT 1 to CNT 2 is much stronger than the adhesion of CNT 1 to the end-effector, permitting rotation between the end-effector and CNT 1.
4) During Procedure 2 and Procedure 3, all inelastic motion occurs about the region of contact between CNT 1 and CNT 2, i.e. the contact between CNT 1 and CNT 2 undergoes no linear motion.
5) During Procedure 4, assumptions 1 and 2 are valid.

Analyses of Procedures 1-4 use a variation of the beam equation derived for Experiment Set 1. For Experiment Set 2 the slope of the cantilever's free end is unconstrained. This leads to the following system where Equation (3.20) is the expression for the variable second moment of inertia:

$$I(x) = \frac{\pi}{4}((R_o + \alpha_o x)^4 - (R_i + \alpha_i x)^4) \tag{3.20}$$

with R_o and R_i representing the outer and inner radii of the tube at the base, α_o and α_i representing the slope of the outer and inner walls, and x representing the distance along the undeflected axis of the tube. This again leads to the Euler-Bernoulli equation for a variable cross-section beam:

$$I(x)y''''(x) + 2I'(x)y'''(x) + I''(x)y''(x) = 0 \tag{3.21}$$

where $y(x)$ is the beam deflection. Equation (3.21) is solved using the following equilibrium and boundary conditions when considering an applied force P:

$$EI(x)y'''(x) + EI'(x)y''(x) + P = 0, \quad x \to L \tag{3.22}$$

$$EI(x)y''(x) + P(x - L) = 0, \quad x \to L \tag{3.23}$$

$$y'(x) = 0, \quad x \to 0 \tag{3.24}$$

$$y(x) = 0, \quad x \to 0 \tag{3.25}$$

where E is the pseudo elastic modulus. For the procedures in which a moment, M, is applied at the contact, the equilibrium and boundary conditions become:

$$EI(x)y'''(x) + EI'(x)y''(x) = 0, \quad x \to L \tag{3.26}$$

$$EI(x)y''(x) + M = 0, \quad x \to L \tag{3.27}$$

$$y'(x) = 0, \quad x \to 0 \tag{3.28}$$

$$y(x) = 0, \quad x \to 0 \tag{3.29}$$

For both systems, L refers to the center of the contact region along the length of the tube. The maximum linear elastic force offered by the contact in resisting slip motion is calculated for each condition and listed in Table 3.9.

Table 3.9: Maximum linear elastic force sustained by nano-contact

Proc.	Constraint Force
[-]	[-]
1.1	0.65 ± 1.21 (0.19) [nN]
1.2	1.35 ± 2.51 (0.40) [nN]
2.1	-0.81 ± 1.55 (0.27) [fNm]
2.2	-1.02 ± 1.99 (1.55) [fNm]
3.1	-0.24 ± 0.56 (0.08) [fNm]
3.2	-0.50 ± 1.14 (0.10) [fNm]
3.3	-2.42 ± 4.92 (0.34) [fNm]
4.1	0.57 ± 1.07 (-) [nN]

While the high systemic uncertainty hinders inter-process comparison when examining the calculated forces, the values are useful in offering an order of magnitude for analysis of the maximum contact resistance. However, direct comparison between experimental factors and levels is possible when examining the raw displacement data from Table 3.8.

Analysis of Procedure 1 draws from Table 3.8 and Table 3.9. In Procedure 1, two primary results are demonstrated. First, it is shown that the contact area is capable of transmitting enough force between the MWCNTs to cause a visible deflection. The average deflection of CNT 2 in Procedure 1.1 and 1.2 is 0.38 µm and 0.80 µm respectively. For comparison, the maximum deflection of CNT 2 (tube #1) due to pure adhesion to the micro-cantilever in Experiment Set 1 was 0.99 µm, demonstrating the intuitive result that the larger the contact area, the more adhesive force present. Second, a statistical difference is evident between the natural and welded performance of the contact. In this example, heat treatment of the contact area increased the average maximum sustainable deflection by a factor of two. A series of images showing these observations is given in Figure 3.15. Greater detail is observable in Figure 3.16 where the linear motion of the contact point (output) is plotted against the commanded input displacement (input) for both Procedures 1.1 and 1.2. The slope of the fitted lines for the natural joint is 0.65 ± 0.12 while the fitted slope for the characteristic welded line shown is 0.71. This indicates that, while welding increases the maximum sustainable force, it does not change the elastic behavior's stiffness.

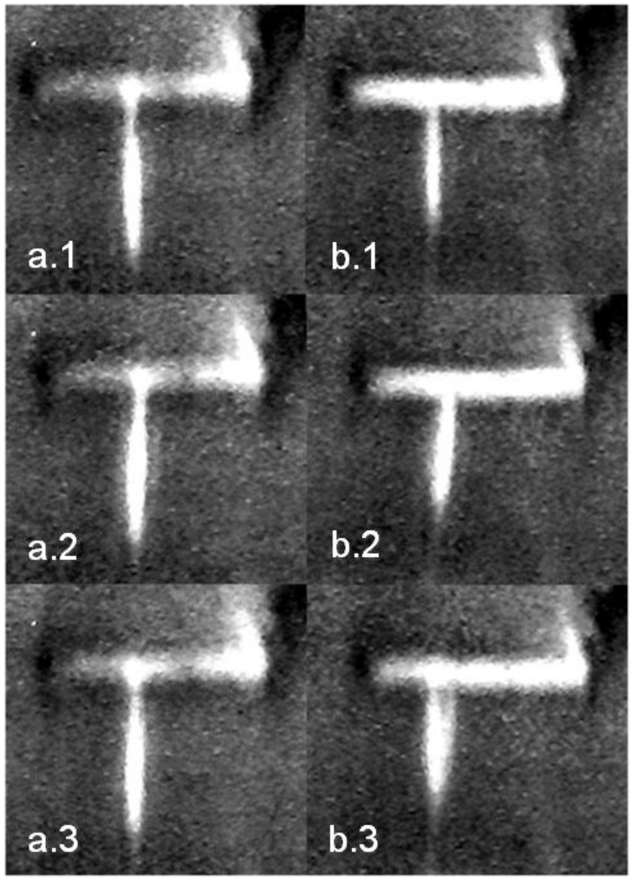

Figure 3.15: Optical images of Procedure 1 with a) demonstration of the natural contact, and b) demonstration of the welded contact

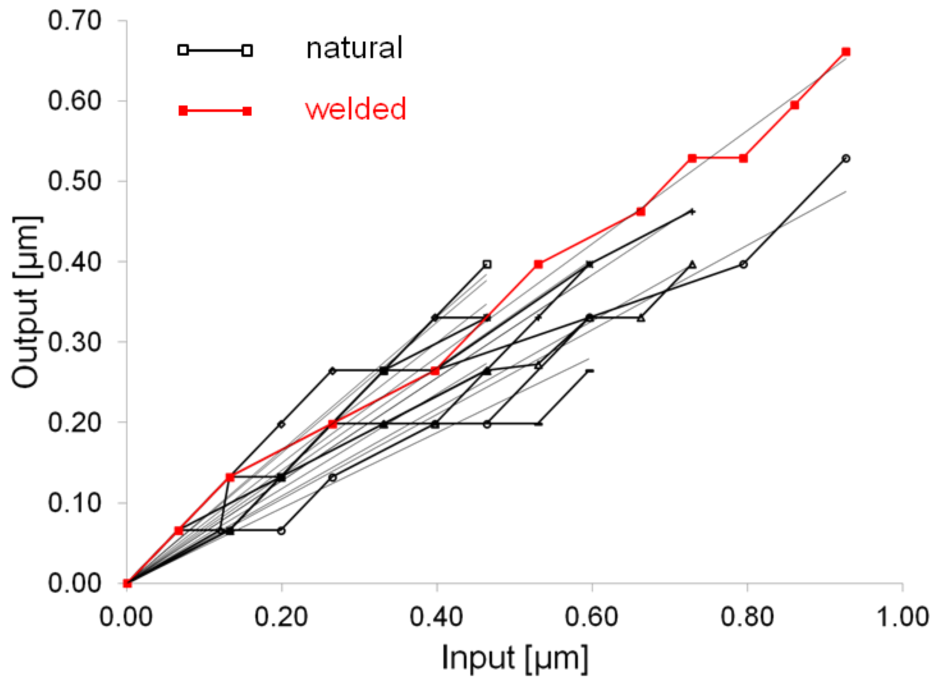

Figure 3.16: Displacement of the contact point with respect to the commanded input displacement

Analysis of Procedure 2 offers two observations. First, the maximum deflection of CNT 2 due to an applied moment is smaller than that due to an applied force as shown in Figure 3.17. The largest average deflection observed is 0.11 µm. Second, no statistical difference between the natural and welded contact area is observed. To ensure that welding had occurred, Procedure 1.2 was applied to the CNT pair again after Procedure 2.2 was performed, i.e. CNT 1 was moved linearly away from CNT 2. Indeed, the deflection of CNT 2 did reach the range measured for the welded linear performance, confirming successful heat treatment. This may demonstrate that a large moment is required to bend these MWCNTs or that the contact has a limited ability to transmit a moment between the structures in this configuration.

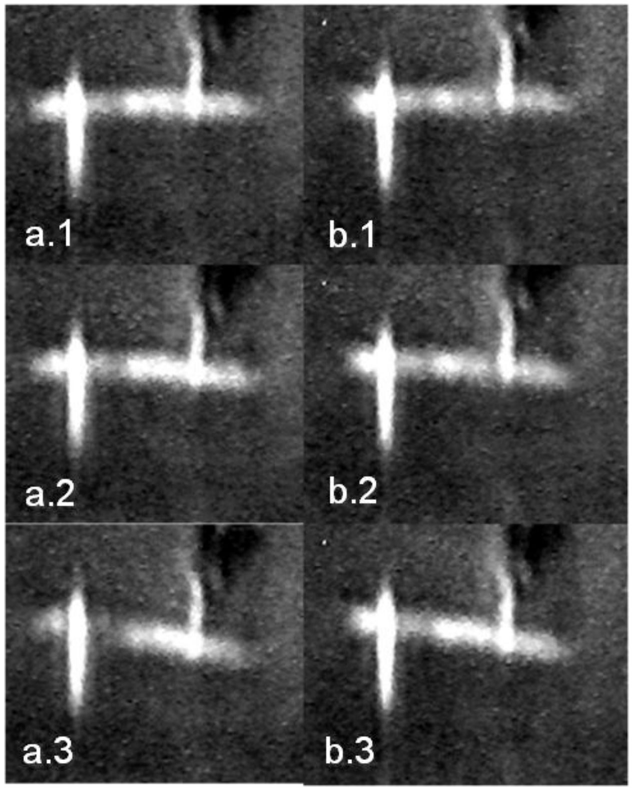

Figure 3.17: Optical images of Procedure 2 with a) demonstration of the natural contact, and b) demonstration of the welded contact

Analysis of Procedure 3 offers three observations. First, that the natural deflection of CNT 2 due to the rotation of CNT 1 is small and statistically similar to that observed in Procedure 2.1. Second, that the heat treatment of the joint does produce a statistically larger deflection in this configuration as compared to the natural condition. However, the welded deflection is statistically similar to that in Procedure 2.2. This suggests that there may be a difference in the deflection between Procedure 2.1 and 2.2 as well but that the experimental uncertainty makes the distinction undetectable. Third, the effect of increasing the natural contact area is large. The maximum deflection observed with the larger area is more than twice that shown for the smaller contact area in the same configuration. This too is in agreement with the observation from Experiment Set 1 that the force of adhesion is dependent on the total contact area.

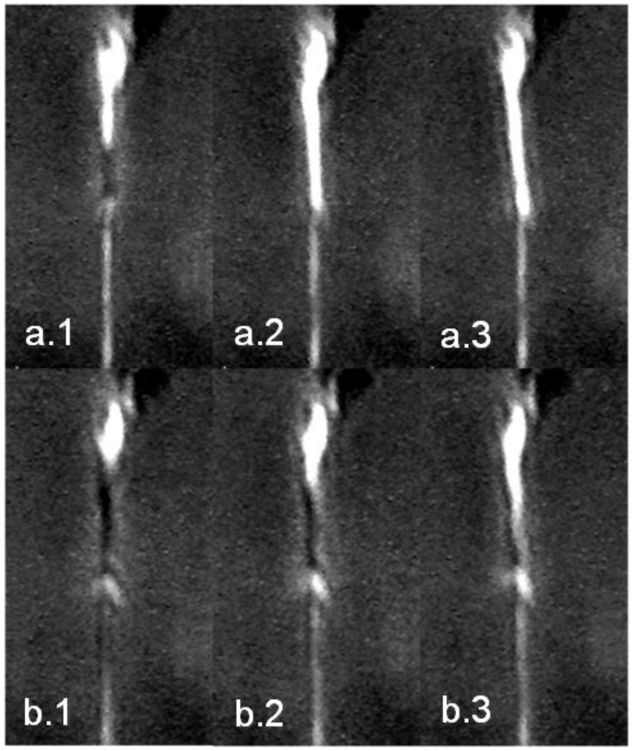

Figure 3.18: Optical images of Procedure 3 with a) demonstration of the natural contact, and b) demonstration of the welded contact

Analysis of Procedure 4 offers three observations. First, that the maximum force sustained by the contact in this experiment agrees with that observed in Procedure 1.1. Second, that there is a measurable elastic component to the nature of the contact prior to the on-set of slipping. Third, a quantitative measurement of the energy-dissipative nature of the nano-joint. Each observation is illustrated in the input/output behavior of the joint given in Figure 3.19.

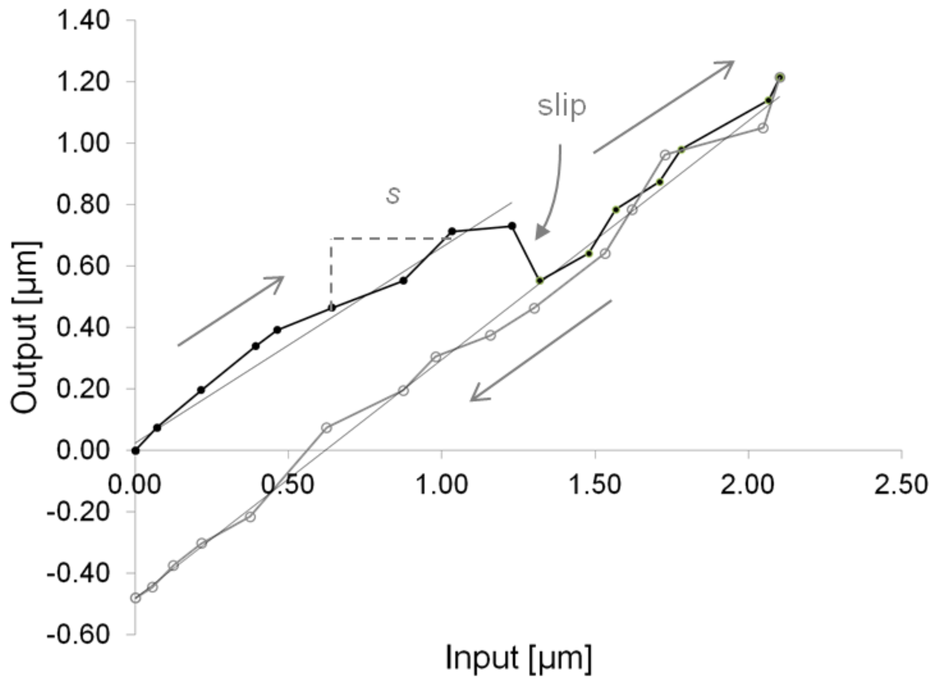

Figure 3.19: Plot of the nano-joint response to a controlled linear displacement

The axes in the plot refer to the lateral motion of CNT 1 in the $+x_1$ direction (input) and the corresponding lateral motion of the contact point with CNT 2 in the same direction (output). The slope of the curve, s, shows that the joint permits elastic motion between the MWCNTs prior to slipping and is related to the elastic stiffness of the joint, k_j, by:

$$k_j = \frac{P_j(L_{app}, \delta_{out})}{\delta_{in} - \delta_{out}} = \frac{P_j(L_{app}, \delta_{out})}{\delta_{in}(1 - s)} \tag{3.30}$$

where P_j is the force applied at the joint's contact, L_{app} is the length along CNT 2 at which the force is applied, and δ_{out} is the motion of the joint due to the applied displacement, δ_{in}. As the slope, s, approaches 1, the joint becomes increasingly stiff. For Procedure 4, the average value for s is 0.707 ± 0.098 and is calculated from the linear fit of both the forward (black) and reverse (gray) motion. From this observation, a stick-slip model can be constructed for the joint. This includes a linearly elastic region of behavior with a stiffness of k_j and a maximum resistive force of

$$\phi_{j,max} = k_j(\delta_{in} - \delta_{out}) \tag{3.31}$$

beyond which an inelastic slipping behavior occurs. Further refinements may be made to this approximation, including a model for the high speed dynamic behavior during slipping, but this represents an accurate first order study of the joint.

To summarize the findings of Experiment Set 2: *Procedure 1* demonstrated the nano-joint's ability to resist rectilinear motion due to an applied force. Procedure 1.1 quantified the maximum force $\phi_{j,max}$ that the joint could elastically withstand naturally while Procedure 1.2 showed how that maximum value could be increased through heat treatment. *Procedure 2* demonstrated the nano-joint's ability to resist rotational motion due to an applied moment. Procedure 2.1 showed that, while small, the ability for the contact to resist motion is observable. Procedure 2.2 showed that heat treatment has little observable effect on the maximum moment the contact could resist. *Procedure 3* demonstrated the effect of the orientation between the bodies on the joint's nature. Procedure 3.1, like 2.1, showed that the contact has a limited ability to resist an applied moment. Procedure 3.2 showed a greater response to heat treatment, resulting in a significant—thought small—difference in the joint's ability to elastically resist motion. Procedure 3.3 showed that when large regions of the CNTs overlap, much larger forces can be transmitted across the contact. This demonstrates the natural dependence of the stiction on the contact area. *Procedure 4* demonstrates the nonlinear, energy-dissipative nature of the joint. Here the hysteretic effect of slipping is shown and a first order model is constructed from the results for a stick-slip spring representation of the joint. Finally, Experiment 2 also demonstrates the ability for the optical nanomanipulation system to successfully assemble nano-scale mechanisms using a dexterous mechanical grasp. SEM images of the assemblies used in Procedures 1-4 are shown in Figure 3.20 as further evidence of this ability.

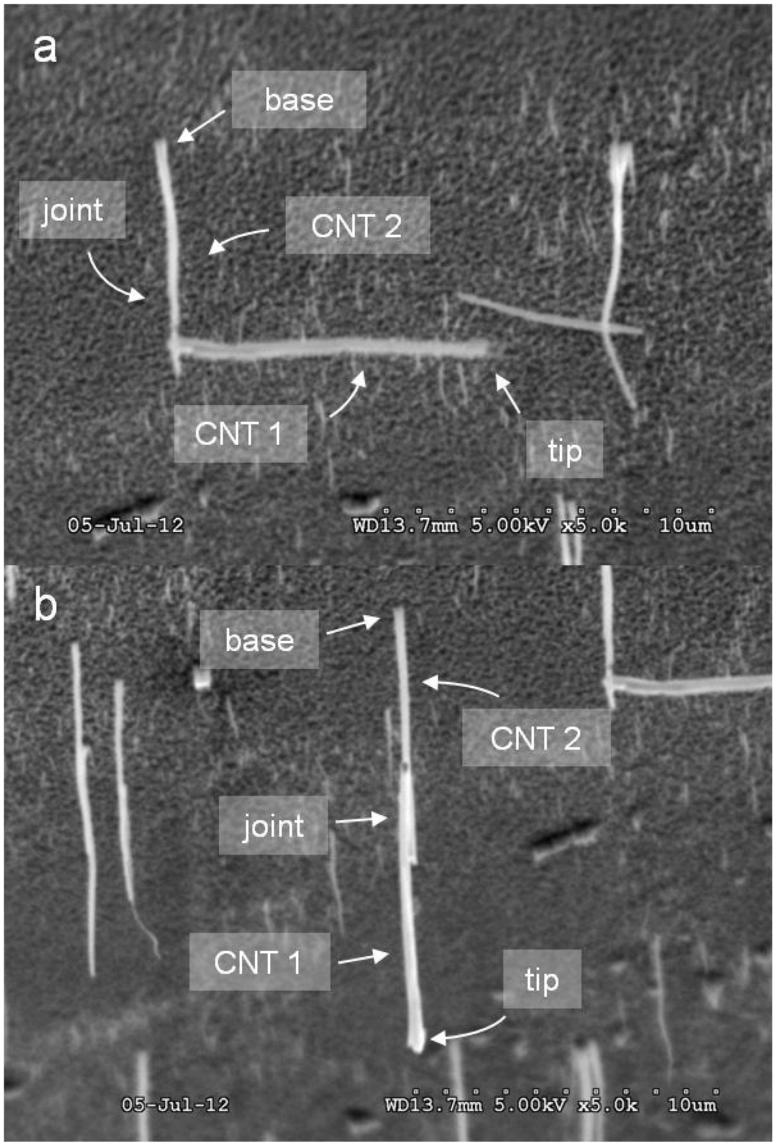

Figure 3.20: SEM images of the nano-mechanical mechanisms constructed as a part of Experiment Set 2

3.4 Experiment 3: Nano Kinematic Chain

By combining the knowledge of the MWCNTs elastic behavior with the stick-slip nature of the contact between multiple MWCNTs previously observed, Experiment Set 3 studies the motion of a closed kinematic chain of three MWCNTs. This is accomplished through arranging the MWCNT chain into a double-rocker four-bar mechanism with three compliant links and a rigid ground (the substrate). By applying a commanded displacement to one of the rockers, the transmission of motion across two nano-adhesive joints can be observed. Experiment Set 3 consists of a single procedure which is illustrated in Figure 3.21.

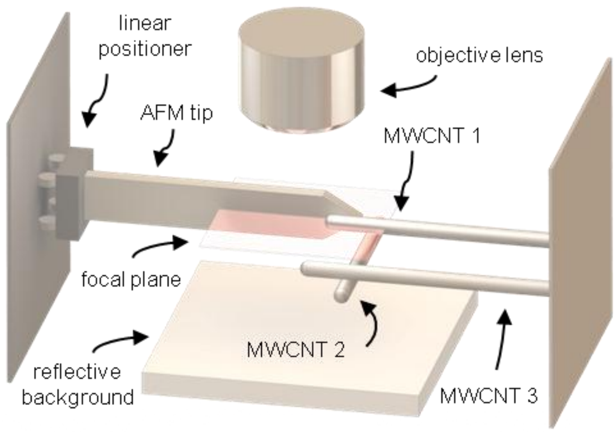

Figure 3.21: The experimental approach using three MWCNTs arranged into a four-bar mechanism with a) the set-up and b) an applied linear displacement

3.4.1 Experiment 3: Procedures

In Experiment Set 3 the primary variable of interest is δ_{CNT3}, the displacement of the MWCNT rocker from its equilibrium position. By examining δ_{CNT3} as CNT 1 is displaced, the elastic behavior of four nano-joints connected in a closed chain can be examined. These joints include three that are reinforced using Joule welding and one created during the MWCNT sample fabrication process. Together these represent a nano-compliant four-bar mechanism. The experimental design is given in Table 3.10.

Table 3.10: Design of Experiment 3

	Variables						
	Controlled					Independent	Dependent
Factors	electrostatic charge	pressure	humidity	contact motion	contact state	input	output
	[C]	[Pa]	%RH	[-]	[-]	[µm]	[µm]
Levels	negligible	ambient	40	linear	welded	0.80	procedure 1

As in Experiment Set 2, preparing the experimental procedure requires positioning and welding of the CNT structures. This involves the cutting of MWCNTs from the surface of the substrate, dexterous manipulation of the structures into position, and welding of the MWCNTs into place (either onto the end-effector, the contacting nanotube, or the substrate). All operations are performed using the same preoperational procedures outlined in Experiment Set 2.

The Procedure investigates the kinematic motion of the nano four-bar mechanism by applying a controlled displacement to free end of CNT 1 and consists of three steps. Step one, with the electrical continuity system activated, the end-effector is moved along the substrate in $-x_1$ direction until contact with the rocker is detected; after which the electrical system is deactivated. Step two, the end-effector is moved in the $-x_1$ direction 0.80 µm. Step three, the end-effector is reversed 0.80 µm in the $+x_1$ direction. Steps two and three are repeated ten times.

3.4.2 Experiment 3: Results and Analysis

Optical images capturing the experimental configuration and procedure are shown in Figure 3.22. From these images the orientation of the links is evident, where both rockers are positioned near vertical relative to the substrate while the coupler is positioned at an angle sloping up and away from the end-effector. The mechanism is constructed from MWCNTs #5, #6, and #10. Tube #6 and #10 are firmly attached to the substrate 3.5 µm apart. Tube # 5 is attached to tube #6 a distance of 6.1 µm from the substrate and tube #10 a distance of 7.8 µm from the substrate. The location of the input commanded displacement is 6.5 µm along CNT #6 as measured from the substrate which is approximately 0.4 µm above the joint with CNT #5. The joint between CNT #5 and CNT #10 is chosen as the output of the mechanism.

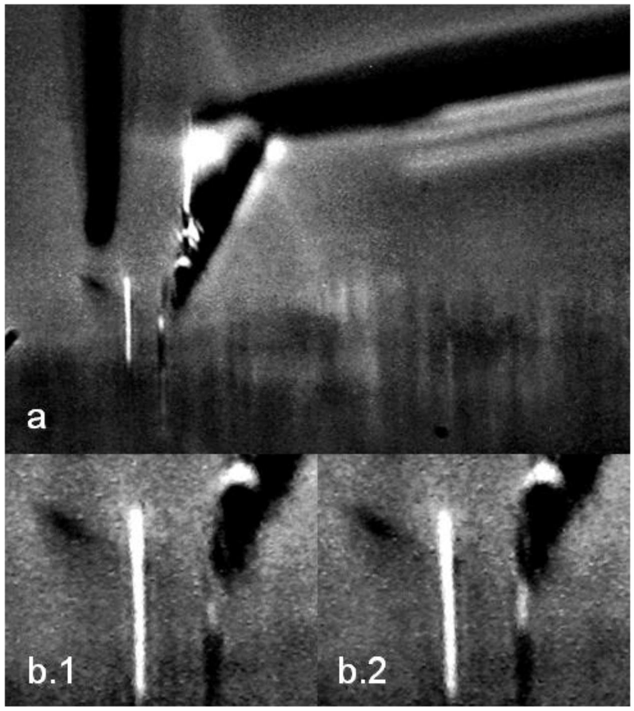

Figure 3.22: Optical image of Experiment 3 where a) shows the relative placement of components and b) shows the procedure

The input/output behavior of the mechanism is plotted for the ten runs in Figure 3.23. The input is measured as the displacement provided by the end-effector to CNT 1 and the output is measured as the resulting motion of the joint between CNT 2 and CNT 3. Multiple effects are compounded in this plot including the elastic behavior of the links, the joints, and the kinematics of the configuration. The plot also shows that each joint remains within its elastic region of behavior.

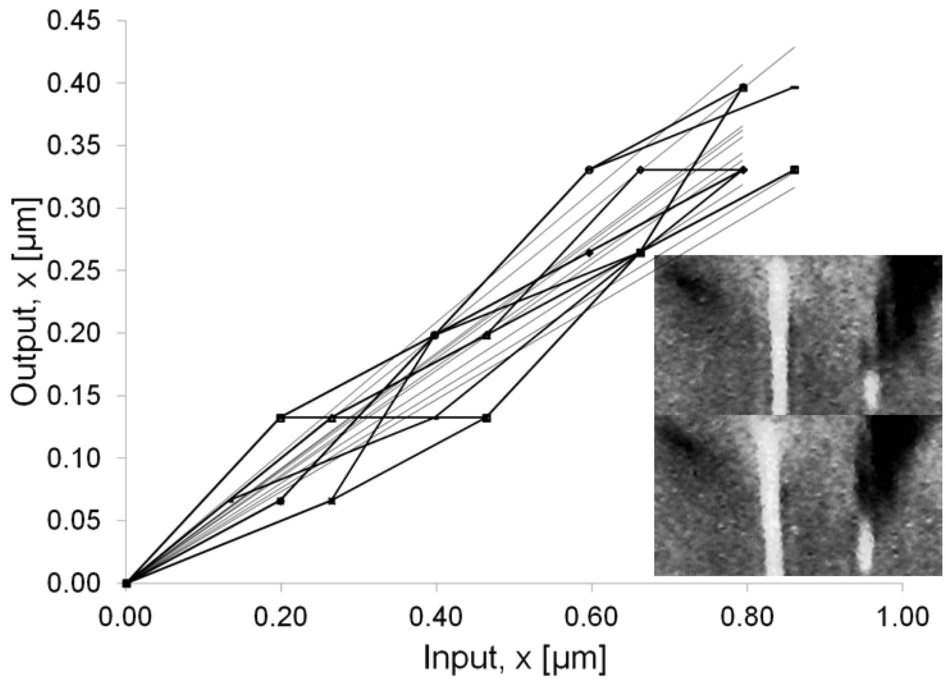

Figure 3.23: Plot of the nano four-bar mechanism response to a controlled linear displacement

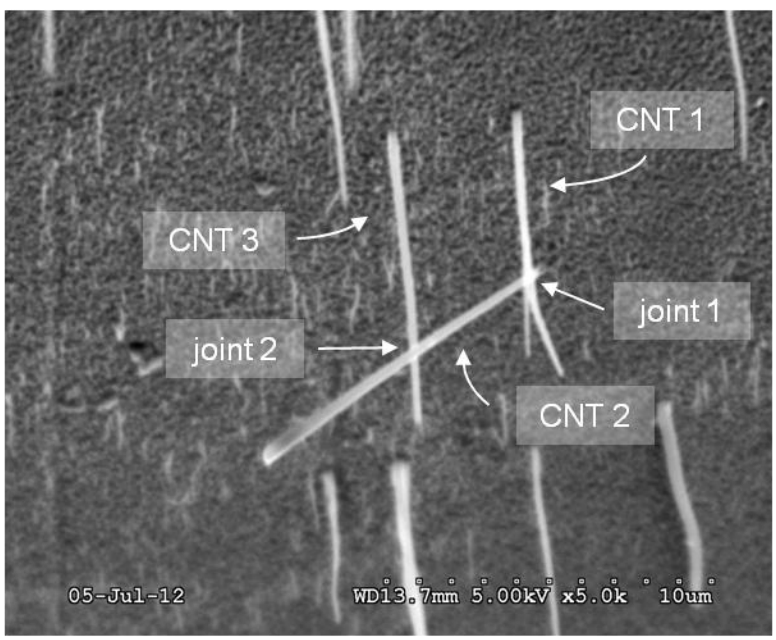

Figure 3.24: SEM images of the nano-mechanical mechanism constructed as a part of Experiment Set 3

In summary, Experiment 3 applies and demonstrates the knowledge gathered from Experiments 1 and 2 to construct a closed-chain kinematic mechanism from nanoscopic components. The prominent observation from this experiment is the successful transmission of motion across three nanoscopic bodies.

3.5 Discussion and Conclusions

Chapter 3 has presented a broad range of experimental investigations used to pursue an understanding of the mechanics and kinematics of both MWCNTs in contact with the end-effectors of a nanomanipulation system and one-another. This is with the aim of advancing the technique of contact nanomanipulation for the assembly of nano-mechanical structures and mechanisms. Three sets of experiments have been reported which each investigating different mechanical aspects associated with nanomanipulation; specifically the dexterous grasp of nanoscopic objects.

Experiment Set 1 has shown how dry adhesion, caused by van der Waals forces, greatly affects the interaction between a MWCNT and a nanomanipulation system's end-effector. This is with regard to the available loading configurations and the contact's ability to apply both a positive and negative force to the surface of an object. Additionally, Experiment Set 1 offered quantitative measurement of the bending stiffness of large diameter, stacked-cone MWCNTs, the pull-off force between the MWCNT and end-effector, and an estimation for the pseudo-elastic modulus of the MWCNT structure.

Experiment Set 2 has demonstrated the nature of the unique nonlinear, energy-dissipative, nonholonomic nano-joint formed between two MWCNTs. This was performed through constructing various arrangements of MWCNT kinematic pairs and systematically exploring how the orientation, motion, and condition of the bodies at the contact affected the joint's behavior. Through this it has been shown that 1) the total area of contact greatly effects the joint's ability to elastically resist motion, 2) for the same contact area, the joint resists linear motion to a greater extent than it does rotational motion, 3) Joule heating does have a measurable effect on the maximum force with which the joint can resist inelastic motion, and 4) once slipping is induced, a hysteretic behavior is observed in the position of the contact between the MWCNTs in the pair.

Experiment Set 3 combines the finding of Set 1 and 2 in the construction and operation of a four-link nano-scale assembly. This assembly constitutes a double-rocker four-bar mechanism with three flexible links. Through controlling the displacement of the end of one of the rockers, the deflection of the other rocker is measured and analyzed. This demonstrates the ability to assemble MWCNTs to form working, compliant nanoscopic mechanisms where the links are joined by the nano-scale adhesive joint investigated in Experiment Set 2.

In all, the experimental observations reported in this chapter constitute a concerted effort towards the advancement of contact nanomanipulation and assembly through investigating flexible nano-structures and adhesive nano-joints.

4 MECHANICS AND KINEMATICS OF NANOMANIPULATION: MODELING

Formulating an accurate model of nano-scale multibody dynamics is an important step toward realizing controllable, automated nanomanipulation and assembly systems. Two features appear to play a dominant role in the dynamics of the nano-mechanical systems studied here: the flexible nature of the links and the nonlinear, nonconservative, nonholonomic nature of the adhesive nano-joints. Capturing these features in a model may aid in the creation of complex, spatially oriented, nanoscopic structures and mechanisms formed from CNTs.

In pursuit of controlled nano-assembly, this chapter utilizes the observations gathered in Chapter 3 to formulate a first stage model for the elastic behavior of nanoscopic multibody systems consisting of flexible linkages constrained by adhesive joints. This model pertains only to the *steady-state*, *linearly elastic* region of behavior for *planar* bodies prior to slipping. However, it is formulated in such a way as to facilitate future expansion into the nonlinear regime and includes suggestions for the pursuit of that goal. This is achieved by formulating the equations of motion using Lagrangian differential algebraic equations which are well suited for solving flexible (under-actuated), nonlinear, non-conservative systems. For the steady-state, conservative system studied in this chapter, the equations of motion are reduced and solved for using a nonlinear optimization routine that minimizes the system's total potential energy. The model's description is separated into seven sections: kinematics of single-body and dual-body systems, kinetics of multibody systems, formulation of the equations of motion, formulation of the nano-body system, methods for solving the equations of motion, model validation and solutions, and discussion of the results with concluding remarks.

4.1 Kinematics

To facilitate the model description, this section offers a brief introduction to the nomenclature used to represent the motion of bodies; both individually and as a constrained pair. This includes the variables for the position, velocity, and acceleration of bodies, points on a body, and select constraint equations. While various systems of symbols are commonly employed to describe these relationships, the nomenclature used here generally follows that of Shabana presented in [138].

4.1.1 Single Body

For a single body subject to planar motion, three quantities are required to fully describe its location at the position level. These quantities are referred to as the generalized coordinates. In the Cartesian system, they are the lateral positions, x and y, and the orientation, θ about z. For each body, i, these are grouped together to form:

$$\boldsymbol{q}^i = [\, q_1^i \quad q_2^i \quad q_3^i]^T = \left[\, R_x^i \quad R_y^i \quad \theta^i \right]^T \tag{4.1}$$

The velocity (4.2) and acceleration (4.3) levels of the generalized coordinates follow by taking successive time derivatives of Equation (4.1):

$$\dot{\boldsymbol{q}}^i = \frac{d}{dt}\boldsymbol{q}^i = \boldsymbol{f}^i = \left[\, \dot{R}_x^i \quad \dot{R}_y^i \quad \dot{\theta}^i \right]^T \tag{4.2}$$

$$\ddot{\boldsymbol{q}}^i = \frac{d}{dt}\dot{\boldsymbol{q}}^i = \dot{\boldsymbol{f}}^i = \left[\, \ddot{R}_x^i \quad \ddot{R}_y^i \quad \ddot{\theta}^i \right]^T \tag{4.3}$$

where the quantities accented by one and two dots represent the first and second time derivatives of the variable respectively. Likewise, the location of point P on body i can be described as:

$$\boldsymbol{r}_P^i = [\, x_P^i \quad y_P^i]^T = \boldsymbol{R}^i + \boldsymbol{A}^i \bar{\boldsymbol{u}}_P^i \tag{4.4}$$

where $\boldsymbol{R}^i = \left[R_x^i(t) \quad R_y^i(t) \right]^T$ locates the origin of the body's reference frame, $\theta^i(t)$ is the orientation of the body in the global reference frame, $\boldsymbol{A}^i(\theta^i)$ is the rotation matrix, and $\overline{\boldsymbol{u}}_P^i = [\, \bar{x}_P^i(t) \quad \bar{y}_P^i(t)]^T$ is the position of point P in the body's frame of reference. With $+\theta^i$ representing rotation in the counter-clockwise direction about z, the rotation matrix can be written as:

$$\boldsymbol{A}^i = \begin{bmatrix} \cos\theta^i & -\sin\theta^i \\ \sin\theta^i & \cos\theta^i \end{bmatrix} \tag{4.5}$$

Assuming for generality that the position of $\overline{\boldsymbol{u}}_P^i$ can vary with time, the velocity of $\boldsymbol{r}_P^i$ is:

$$\dot{\boldsymbol{r}}_P^i = \dot{\boldsymbol{R}}^i + \dot{\theta}^i \boldsymbol{A}_\theta^i \overline{\boldsymbol{u}}_P^i + \boldsymbol{A}^i \dot{\overline{\boldsymbol{u}}}_P^i \tag{4.6}$$

where

$$\boldsymbol{A}_\theta^i = \frac{\partial}{\partial \theta^i} \boldsymbol{A}^i = \begin{bmatrix} -\sin\theta^i & -\cos\theta^i \\ \cos\theta^i & -\sin\theta^i \end{bmatrix} \tag{4.7}$$

The expression for the acceleration of $\boldsymbol{r}_P^i$ follows:

$$\ddot{\boldsymbol{r}}_P^i = \ddot{\boldsymbol{R}}^i - \dot{\theta}^{i^2} \boldsymbol{A}^i \overline{\boldsymbol{u}}_P^i + \ddot{\theta} \boldsymbol{A}_\theta^i \overline{\boldsymbol{u}}_P^i + 2\dot{\theta}^i \boldsymbol{A}_\theta^i \dot{\overline{\boldsymbol{u}}}_P^i + \boldsymbol{A}^i \ddot{\overline{\boldsymbol{u}}}_P^i \tag{4.8}$$

This series of equations, (4.1) – (4.8), can be used to describe the motion of a planar body and a point moving on that body. From these relationships, constraints governing the coupled behavior of two bodies can be described.

4.1.2 Two Body

Constraint equations describe the position-level relationships restricting either the motion of a single body or those of multiple coupled bodies. The system of these relationships is represented in the constraint matrix, $\boldsymbol{C}$. For the MWCNT mechanisms, this matrix includes sets of commanded displacements and kinematic joints.

Direct constraint on the pose of a body or the location of a point on a body can take the form of:

$$\boldsymbol{C}_1(\boldsymbol{q},t) = \boldsymbol{q}^i - \boldsymbol{c}^i = \boldsymbol{0} \tag{4.9}$$

or

$$\boldsymbol{C}_2(\boldsymbol{q},t) = \boldsymbol{r}_P^i - \boldsymbol{c}_P^i = \boldsymbol{0} \tag{4.10}$$

where $\boldsymbol{c}^i = [c_1^i(t) \quad c_2^i(t) \quad c_3^i(t)]^T$ and $\boldsymbol{c}_P^i = [c_{P1}^i(t) \quad c_{P2}^i(t)]^T$. Inter-body joints are described in a similar manner. For a revolute joint—where two bodies are connected at a point around which both may rotate—the constraint relationship can be formulated as:

$$\boldsymbol{C}_3(\boldsymbol{q},t) = \boldsymbol{r}_P^i - \boldsymbol{r}_P^j = \boldsymbol{R}^i + \boldsymbol{A}^i\bar{\boldsymbol{u}}_P^i - \boldsymbol{R}^j - \boldsymbol{A}^j\bar{\boldsymbol{u}}_P^j = \boldsymbol{0} \tag{4.11}$$

where $\bar{\boldsymbol{u}}_P^i$ and $\bar{\boldsymbol{u}}_P^j$ are constant. The position variable $\bar{\boldsymbol{u}}_P$ may also vary with time. Under certain conditions, such as when describing surface contact between bodies, it may be beneficial to parameterize $\bar{\boldsymbol{u}}_P$ as a function of s:

$$\bar{\boldsymbol{u}}_P^i = \left[\, \bar{x}_P^i\big(s(t)\big) \quad \bar{y}_P^i\big(s(t)\big)\right]^T \tag{4.12}$$

where the vector $\boldsymbol{s}^i = \begin{bmatrix} s_1^i & s_2^i & \cdots & s_{n_s}^i \end{bmatrix}^T$ can accompany the vector $\boldsymbol{q}^i$ in describing the position of body i using n_s additional variables. In this case, $\boldsymbol{s}^i$ can also be described at the position, velocity, and acceleration level:

$$\boldsymbol{s}^i = \begin{bmatrix} s_1^i & s_2^i & \cdots & s_{n_s}^i \end{bmatrix}^T \tag{4.13}$$

$$\dot{\boldsymbol{s}}^i = \frac{d}{dt}\boldsymbol{s}^i = \boldsymbol{g}^i = \begin{bmatrix} \dot{s}_1^i & \dot{s}_2^i & \cdots & \dot{s}_{n_s}^i \end{bmatrix}^T \tag{4.14}$$

$$\ddot{\boldsymbol{s}}^i = \frac{d}{dt}\dot{\boldsymbol{s}}^i = \dot{\boldsymbol{g}}^i = \begin{bmatrix} \ddot{s}_1^i & \ddot{s}_2^i & \cdots & \ddot{s}_{n_s}^i \end{bmatrix}^T \tag{4.15}$$

Each individual constraint can be combined into a system at the position level using matrix notation:

$$\boldsymbol{C}(\boldsymbol{q},\boldsymbol{s},t) = [\,\boldsymbol{C}_1(\boldsymbol{q},\boldsymbol{s},t) \quad \boldsymbol{C}_2(\boldsymbol{q},\boldsymbol{s},t) \quad \cdots \quad \boldsymbol{C}_n(\boldsymbol{q},\boldsymbol{s},t)]^T \tag{4.16}$$

For a system with explicit dependencies on pose ($\boldsymbol{q}$), secondary parameters ($\boldsymbol{s}$), and time (t) the velocity level constrain matrix takes the form:

$$\frac{d}{dt}\boldsymbol{C}(\boldsymbol{q},\boldsymbol{s},t) = \boldsymbol{C}_{\boldsymbol{q}}\dot{\boldsymbol{q}} + \boldsymbol{C}_{\boldsymbol{s}}\dot{\boldsymbol{s}} + \boldsymbol{C}_t = \boldsymbol{0} \tag{4.17}$$

where

$$\boldsymbol{C}_{\boldsymbol{q}} = \frac{\partial}{\partial \boldsymbol{q}}\boldsymbol{C}(\boldsymbol{q},\boldsymbol{s},t) \tag{4.18}$$

$$\boldsymbol{C}_{s} = \frac{\partial}{\partial \boldsymbol{s}}\boldsymbol{C}(\boldsymbol{q},\boldsymbol{s},t) \tag{4.19}$$

$$\boldsymbol{C}_t = \frac{\partial}{\partial t}\boldsymbol{C}(\boldsymbol{q},\boldsymbol{s},t) \tag{4.20}$$

Likewise, the acceleration level constraint matrix can be expressed as:

$$\frac{d^2}{dt^2}\boldsymbol{C}(\boldsymbol{q},\boldsymbol{s},t) = \boldsymbol{C_q}\ddot{\boldsymbol{q}} + \boldsymbol{C_s}\ddot{\boldsymbol{s}} + \left(\boldsymbol{C_q}\dot{\boldsymbol{q}}\right)_{\boldsymbol{q}}\dot{\boldsymbol{q}} + (\boldsymbol{C_s}\dot{\boldsymbol{s}})_{\boldsymbol{s}}\dot{\boldsymbol{s}} + \mathbf{2}\boldsymbol{C}_{\boldsymbol{q}t}\dot{\boldsymbol{q}} + \mathbf{2}\boldsymbol{C}_{\boldsymbol{s}t}\dot{\boldsymbol{s}} + \mathbf{2}\boldsymbol{C}_{\boldsymbol{qs}}\dot{\boldsymbol{q}}\dot{\boldsymbol{s}} + \boldsymbol{C}_{tt} \tag{4.21}$$

where

$$\left(\boldsymbol{C_q}\dot{\boldsymbol{q}}\right)_{\boldsymbol{q}} = \frac{\partial}{\partial \boldsymbol{q}}\boldsymbol{C_q}\dot{\boldsymbol{q}} \tag{4.22}$$

$$(\boldsymbol{C_s}\dot{\boldsymbol{s}})_{\boldsymbol{s}} = \frac{\partial}{\partial \boldsymbol{s}}\boldsymbol{C_s}\dot{\boldsymbol{s}} \tag{4.23}$$

$$\boldsymbol{C}_{\boldsymbol{q}t} = \frac{\partial}{\partial t}\boldsymbol{C_q}(\boldsymbol{q},\boldsymbol{s},t) \tag{4.24}$$

$$\boldsymbol{C}_{\boldsymbol{s}t} = \frac{\partial}{\partial t}\boldsymbol{C_s}(\boldsymbol{q},\boldsymbol{s},t) \tag{4.25}$$

$$\boldsymbol{C}_{tt} = \frac{\partial}{\partial t}\boldsymbol{C}_t(\boldsymbol{q},\boldsymbol{s},t) \tag{4.26}$$

Together, the equations offered in this section describe some of the basic kinematic relationships of free and constrained bodies which will be useful in describing the nano-mechanical system presented in this work.

4.2 Kinetics

The kinematics of section 4.1 is combined with kinetics to formulate a compact, generalized system of equations, describing how the various forces affect a nano-multibody system. Kinetics relates the motion of a body to the efforts or causes of the motion; that being forces and moments in this study. Lagrangian mechanics offers an elegant method for describing this relationship. For non-conservative systems in which a body—having both kinetic energy, $\boldsymbol{T}$, and potential energy, $\boldsymbol{P}$—can lose energy due to dissipation, $\boldsymbol{D}$, the generalize formulation of the energies can be written as:

$$\boldsymbol{T} = \boldsymbol{T}(\boldsymbol{q}, \dot{\boldsymbol{q}}) \tag{4.27}$$

$$\boldsymbol{V} = \boldsymbol{V}(\boldsymbol{q}) \tag{4.28}$$

$$\boldsymbol{D} = \boldsymbol{D}(\dot{\boldsymbol{q}}) \tag{4.29}$$

For a multibody system, the total kinetic, potential, and dissipative energy is the sum of the energy of each individual body, i, over the total number of bodies, n_b:

$$\boldsymbol{T} = \sum_{i=1}^{n_b} \boldsymbol{T}^i \tag{4.30}$$

$$\boldsymbol{V} = \sum_{i=1}^{n_b} \boldsymbol{V}^i \tag{4.31}$$

$$\boldsymbol{D} = \sum_{i=1}^{n_b} \boldsymbol{D}^i \tag{4.32}$$

Using the nomenclature presented in section 4.1, the energies associated with the motion of a rigid body, —where its frame of reference is coincident with its center of mass—can be written as:

$$\boldsymbol{T}^i = \frac{1}{2} m^i \dot{\boldsymbol{R}}^{i^T} \dot{\boldsymbol{R}}^i + \frac{1}{2} J^i \left(\dot{\theta}^i\right)^2 \tag{4.33}$$

$$\boldsymbol{V}^i = \boldsymbol{V}^i\left(\boldsymbol{R}^i, \theta^i\right) \tag{4.34}$$

$$\boldsymbol{D}^i = \boldsymbol{D}^i\left(\dot{\boldsymbol{R}}^i, \dot{\theta}^i\right) \tag{4.35}$$

with m^i representing the inertial mass of the body and J^i representing the mass moment of inertia. The various forms of energy in the system are related through the Lagrangian equation:

$$\frac{d}{dt}\left(\frac{\partial \boldsymbol{\mathcal{L}}}{\partial \dot{\boldsymbol{q}}}\right) - \frac{\partial \boldsymbol{\mathcal{L}}}{\partial \boldsymbol{q}} + \frac{\partial \boldsymbol{D}}{\partial \dot{\boldsymbol{q}}} = \boldsymbol{0} \tag{4.36}$$

where $\boldsymbol{\mathcal{L}}$ is the Lagrangian function:

$$\boldsymbol{\mathcal{L}} = \boldsymbol{T} - \boldsymbol{V} \tag{4.37}$$

This formulation assumes that $\partial \boldsymbol{V}/\partial \dot{\boldsymbol{q}} = 0$, which is maintained in this system. The result given in (4.36) is a system of second-order differential equations describing the motion of bodies subject to non-conservative forces, without the constraints explicitly stated. This is a basis for formulating the equations of motion for constrained systems.

4.3 Equations of Motion for Constrained Systems

The Euler-Lagrange formulation expands on Equation (4.36) by introducing the Lagrangian multiplier, $\boldsymbol{\lambda}$, which accounts for the forces maintaining the algebraic constraints, $\boldsymbol{C}$. The result is a coupled system of both differential and algebraic equations (DAEs):

$$\frac{d}{dt}\left(\frac{\partial \boldsymbol{\mathcal{L}}}{\partial \dot{\boldsymbol{q}}}\right) - \frac{\partial \boldsymbol{\mathcal{L}}}{\partial \boldsymbol{q}} - \boldsymbol{\lambda}\frac{\partial \boldsymbol{C}}{\partial \boldsymbol{q}} + \frac{\partial \boldsymbol{D}}{\partial \dot{\boldsymbol{q}}} = \boldsymbol{0} \tag{4.38}$$

$$\boldsymbol{C}(\boldsymbol{q}) = \boldsymbol{0} \tag{4.39}$$

While general, this formulation is not readily solved using computational methods. To address this issue, the system can be reformulated by: evaluating the partial derivatives of Equation (4.38), putting the generalized coordinates in a state space representation, and explicitly including the external forcing functions, $\boldsymbol{e}^S$ (sources of effort). Doing so results in the generalized index-3 Lagrangian DAEs (LDAEs) for constrained dynamics presented in [139]:

$$\dot{\boldsymbol{q}} - \boldsymbol{f} = \boldsymbol{0} \tag{4.40}$$

$$\boldsymbol{M}\dot{\boldsymbol{f}} + \boldsymbol{C}_{\boldsymbol{q}}^T\boldsymbol{\lambda} - \boldsymbol{Q}_e = \boldsymbol{0} \tag{4.41}$$

$$\boldsymbol{C}(\boldsymbol{q}) = \boldsymbol{0} \tag{4.42}$$

where the mass matrix, $\boldsymbol{M}$, is:

$$\boldsymbol{M} = \frac{\partial^2 \boldsymbol{T}}{\partial \boldsymbol{f}^2} \tag{4.43}$$

and $\boldsymbol{Q}_e$, which includes the terms that are generally quadratic with respect to the coordinates, $\boldsymbol{q}$, is:

$$\boldsymbol{Q_e} = -\left[\left[\frac{\partial}{\partial \boldsymbol{q}}\left(\frac{\partial \boldsymbol{T}}{\partial \boldsymbol{f}}\right)\right]\boldsymbol{f} + \frac{\partial}{\partial t}\left(\frac{\partial \boldsymbol{T}}{\partial \boldsymbol{f}}\right) - \frac{\partial \boldsymbol{T}}{\partial \boldsymbol{q}} + \frac{\partial \boldsymbol{V}}{\partial \boldsymbol{q}} + \frac{\partial \boldsymbol{D}}{\partial \boldsymbol{f}} - \boldsymbol{e}^s\right] \tag{4.44}$$

By adding both velocity (flow) and force (effort) constraints to equations (4.40) – (4.42), the equations of motion for a broad variety of physical systems can be captured in this form. In addition to its generality, "this approach to systems modeling is particularly attractive for physical systems that involve a large number of variables, or systems that contain nonlinear constraints," [139], such as found in flexible MWCNT multibody systems.

For the potential configuration of bodies and constraints present in the MWCNT mechanism, the LDAE system can be further refined and expanded. This includes the parameterized variables, $\boldsymbol{s}$, for contact between surfaces as described in [138] and the derivatives of the constraint matrix, relating the acceleration level of the kinematic constraints to the kinetic equations:

$$\dot{\boldsymbol{q}} - \boldsymbol{f} = \boldsymbol{0} \tag{4.45}$$

$$\dot{\boldsymbol{s}} - \boldsymbol{g} = \boldsymbol{0} \tag{4.46}$$

$$\boldsymbol{M}\dot{\boldsymbol{f}} + \boldsymbol{C}_{\boldsymbol{q}}^{T}\boldsymbol{\lambda} + \left(\boldsymbol{V}_{\boldsymbol{q}} + \boldsymbol{D}_{\boldsymbol{f}} - \boldsymbol{e}^{s}\right) = \boldsymbol{0} \tag{4.47}$$

$$\boldsymbol{C}_{\boldsymbol{s}}^{T}\boldsymbol{\lambda} = \boldsymbol{0} \tag{4.48}$$

$$\boldsymbol{C} = \boldsymbol{0} \tag{4.49}$$

$$\boldsymbol{C}_{\boldsymbol{q}}\boldsymbol{f} + \boldsymbol{C}_{\boldsymbol{s}}\boldsymbol{g} + \boldsymbol{C}_{t} = \boldsymbol{0} \tag{4.50}$$

$$\boldsymbol{C}_{\boldsymbol{q}}\dot{\boldsymbol{f}} + \boldsymbol{C}_{\boldsymbol{s}}\dot{\boldsymbol{g}} + \left(\boldsymbol{C}_{\boldsymbol{q}}\dot{\boldsymbol{q}}\right)_{\boldsymbol{q}}\boldsymbol{f} + (\boldsymbol{C}_{\boldsymbol{s}}\dot{\boldsymbol{s}})_{\boldsymbol{s}}\boldsymbol{g} + 2\boldsymbol{C}_{\boldsymbol{q}t}\boldsymbol{f} + 2\boldsymbol{C}_{\boldsymbol{s}t}\boldsymbol{g} + 2\boldsymbol{C}_{\boldsymbol{qs}}\boldsymbol{f}\boldsymbol{g} + \boldsymbol{C}_{tt} = \boldsymbol{0} \tag{4.51}$$

where $\boldsymbol{V}_{\boldsymbol{q}} = \partial\boldsymbol{V}/\partial\boldsymbol{q}$ and $\boldsymbol{D}_{\boldsymbol{f}} = \partial\boldsymbol{D}/\partial\boldsymbol{f}$. This represents a generalized formulation for the equations of motion of constrained multibody systems. With the judicious choice of the methods for modeling flexible bodies and the stick-slip nano-joint, this generalized formulation may be applied to multibody CNT systems.

4.4 Formulation of the Nano-mechanical System

Two primary features are considered in the formulation of the nano-mechanical system: the flexible nature of the linkages and the nonlinear, energy dissipative behavior of the adhesive joints constraining them. Models for both the bodies and joints are presented in this section.

4.4.1 Flexible Bodies

Chapter 3 demonstrated the MWCNTs ability to undergo large deflections elastically, which plays a significant role in the kinematics and kinetics of manipulating these nano-structures. Flexible-body motion differs from that of a rigid body (described in sections 4.1 and 4.2) in that separate regions of the same body are allowed to move relative to one another as the body deforms. Accordingly, the mass matrix varies with time as the distribution of the body's inertia changes with the shape. This greatly complicates the description of the body's kinematics and kinetics.

Various methods exist for describing the behavior of flexible linkages in multibody dynamics. Compliant-segmentation [140] is one such method in which flexible bodies are discretized into a collection of rigid segments. Each segment is coupled by a kinematic constraint and a force element for the purpose of mimicking the behavior of the flexible body. This method is a bridge between classic multibody formulations and finite element methods. It is beneficial in that the origin of the segment's reference frame can remain coincident with its center of mass throughout the motion and that the inertial matrix for each segment remains constant. For these reasons, and its ability to be readily integrated with the general LDAE formulation, compliant-segmentation is used to describe the flexible MWCNT in this model. To illustrate this concept, a compliant-segment representation of a planar flexible beam is shown in Figure 4.1 where multiple segments are connected by revolute joints and influenced by torsion-spring force elements.

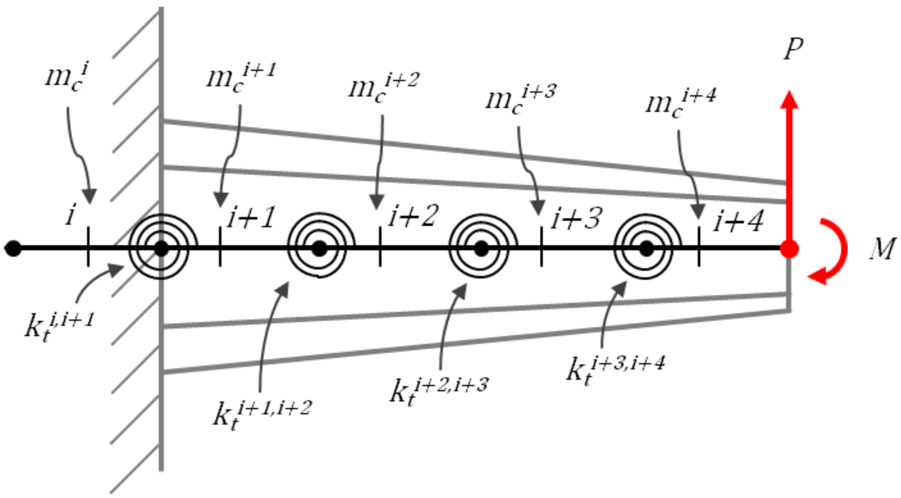

Figure 4.1: Model of a flexible beam representation using compliant-segmentation

Here each segment in connected by means of a revolute constraint where the position vectors, $\bar{\boldsymbol{u}}_P$, are constant:

$$\boldsymbol{C}\left(\boldsymbol{q}^i,\, \boldsymbol{q}^j\right) = \boldsymbol{r}_A^i - \boldsymbol{r}_A^j = \boldsymbol{R}^i + \boldsymbol{A}^i\bar{\boldsymbol{u}}_A^i - \boldsymbol{R}^j - \boldsymbol{A}^j\bar{\boldsymbol{u}}_A^j = \boldsymbol{0} \tag{4.52}$$

with the superscripts i and j referring to adjacent segments in the beam. The moments, M^i and M^j, and potential energy, V^{ij} , of the accompanying torsion spring are:

$$M^i = -k_t^{ij}\left(\theta^i - \theta^j - \theta_0^{ij}\right) \tag{4.53}$$

$$M^j = -k_t^{ij}\left(\theta^j - \theta^i - \theta_0^{ji}\right) \tag{4.54}$$

$$V^{ij} = \frac{k_t^{ij}}{2}\left(\theta^j - \theta^i - \theta_0^{ij}\right)^2 \tag{4.55}$$

where $\theta_0^{ij} = \theta_0^i - \theta_0^j$ and $\theta_0^{ji} = \theta_0^j - \theta_0^i$ are the equilibrium angles between bodies i and j . The component of the internal force matrix resulting from the torsion spring is:

$$\boldsymbol{V}_{\boldsymbol{q}}^i = [\,0 \quad 0 \quad M^i\,]^T \tag{4.56}$$

For the variable radii MWCNTs, each segment's frame of reference is fixed to its center of mass. The location of the frame's origin and the segment's inertial characteristics are determined by assuming the simplified geometry described in Chapter 2. Accordingly, the volume of each segment is the volume of a truncated hollow cone:

$$\not{V}^i = \not{V}^i_{s,out} - \not{V}^i_{s,in} \tag{4.57}$$

where the subscript s denotes a solid volume, the subscript out refers to the cone forming the outer wall, and the subscript in refers to the cone forming the inner wall. Here

$$\not{V}^i_s = \frac{\pi h}{3}\left({R^i_a}^2 + R^i_a R^i_b + {R^i_b}^2\right) \tag{4.58}$$

describes the volume for a truncated solid cone where h is the length of the segment, R^i_a is the radius of the cone's bottom surface, and R^i_b is the radius of the cone's top surface. Assuming a constant density, ρ, the center of mass of the tubular segment is located along the axis of the tube a distance m^i_c from the base:

$$m^i_c = \frac{\not{V}^i_{out} m^i_{c,s\ out} - \not{V}^i_{in} m^i_{c,s\ in}}{\not{V}^i_{out} - \not{V}^i_{in}} \tag{4.59}$$

where $m^i_{c,s}$ is the mass center of each solid cone:

$$m^i_{c,s} = \frac{h\left({R^i_a}^2 + 2R^i_a R^i_b + 3{R^i_b}^2\right)}{4\left({R^i_a}^2 + R^i_a R^i_b + {R^i_b}^2\right)} \tag{4.60}$$

The linear and rotational inertia are calculated using the hollow volume and the mass center point. The linear inertial mass is:

$$m = \rho \cancel{V}^i \tag{4.61}$$

The segment's mass moment of inertia is calculated using [141] about the base of the hollow cone. Here, $f_1(x)$ is the curve representing the inner wall of the tube along the segment's length x, and $f_2(x)$ is the curve of the outer wall.

$$J_x = \frac{\pi\rho}{2}\int_{x_0}^{x_f}[f_2(x)^4 - f_1(x)^4]\,dx \tag{4.62}$$

$$J_y = \frac{J_x}{2} + \pi\rho\int_{x_0}^{x_f}x^2[f_2(x)^2 - f_1(x)^2]\,dx \tag{4.63}$$

$$J_z = \frac{J_x}{2} + \pi\rho\int_{x_0}^{x_f}x^2[f_2(x)^2 - f_1(x)^2]\,dx \tag{4.64}$$

Using the parallel axis theorem, the moment of inertia about the mass center point is given by:

$$J_{z'} = J_z + mr^2 \tag{4.65}$$

where $r = m_c^i$. Given Equations (4.57) – (4.65), the reference frame and inertial constants for each segment can be determined.

Two factors greatly influence the accuracy of compliant-segment models: the number of segments, n_s, and the magnitude of the force elements, k_t. As the number of segments is increased, the chain of rigid bodies can more closely approximate the true curve of the flexible beam. This comes at the cost of increasing the number of generalized coordinates in the multibody formulation. By tuning the stiffness of the springs, the number of segments can be minimized to achieve both accuracy and decrease computational time. Optimization of the number of elements and the stiffness of the springs for general loading conditions has not been previously reported to the author's knowledge. Due to the importance of the flexible body's performance in the system, optimization is performed in section 4.6 during model validation.

4.4.2 Nano Stick-Slip Joint

In addition to the flexible elastic nature of MWCNTs, Chapter 3 demonstrated the unique stick-slip behavior of the contact between MWCNTs. Representing this behavior in the equations of motion for nano-multibody systems may prove pivotal in constructing high-precision, automated nanomanipulation systems. Three primary characteristics of the joint were demonstrated: 1) the elastic response near the equilibrium configuration, 2) the inelastic response beyond a specific, repeatable threshold, and 3) the dependence of the elastic response on contact area size. Each characteristic must be represented in the joint model so as to fully represent the nano stick-slip joint. While this model is only an initial investigation—and as such is solely concerned with the elastic region of behavior—suggestions for implementing the inelastic response are also presented.

Elastic Response: The contact's elastic region of behavior between bodies, α and β, can be represented by a simple linear spring with a stiffness k_j as demonstrated in Section 3.3.2. The force vector exerted by the spring, $\boldsymbol{\phi}_j$, is a function of the displacement between the equilibrium contact points on each body, $\boldsymbol{r}_C^\alpha$ and $\boldsymbol{r}_C^\beta$:

$$\boldsymbol{\phi}_j^\alpha = -k_j \left(\boldsymbol{r}_C^\beta - \boldsymbol{r}_C^\alpha \right) \tag{4.66}$$

$$\boldsymbol{\phi}_j^\beta = -k_j \left(\boldsymbol{r}_C^\alpha - \boldsymbol{r}_C^\beta \right) \tag{4.67}$$

with a corresponding potential energy:

$$V_j^{\alpha\beta} = \frac{k_j}{2}\left(\boldsymbol{r}_C^\alpha - \boldsymbol{r}_C^\beta\right)^T \left(\boldsymbol{r}_C^\alpha - \boldsymbol{r}_C^\beta\right) \tag{4.68}$$

where $\bar{\boldsymbol{r}}_C^i = \begin{bmatrix}\bar{r}_{C,1}^i & \bar{r}_{C,2}^i\end{bmatrix}$ is the vector of the contact point in segment i's body frame of reference.

Due to the potential slipping behavior of the joint, both $\boldsymbol{r}_C^\alpha$ and $\boldsymbol{r}_C^\beta$ cannot necessarily be fixed in a particular segment's frame of reference. One solution is to locate the these points along smooth parameterized curves $\boldsymbol{f}^\alpha(x(s_1^\alpha),\ y(s_2^\alpha))$ and $\boldsymbol{f}^\beta(x(s_1^\beta),\ y(s_2^\beta))$ fixed to each body, which intersect the the mass center points of the three nearest segments to the contact region along with the point of contact itself as illustrated in Figure 4.2. Such curves can be represented by seventh degree polynomials where the coefficients are determined by the location of the intersection points, the orientation of the segments, and the angles of each body. Necessarily, as the bodies deform these curves must be recalculated, either regarding their coefficients and/or the segments they connect as the contact point slides along the body. The resulting kinematic constraint is given in Equation (4.69). Since this investigation is only concerned with the elastic region of behavior, relative motion of the contact's equilibrium position does not occur, and hence the use of parameterized curves is a suggested solution for future consideration. Still, the concept is presented here for completeness.

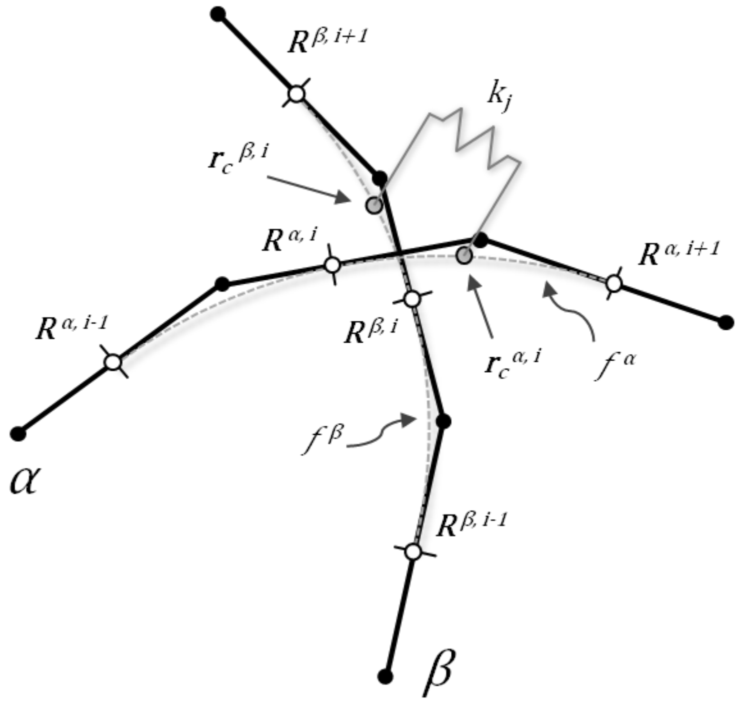

Figure 4.2: Diagram of the equilibrium contact points between bodies α and β located along the parameterized curves $\boldsymbol{f}^{\alpha}$and $\boldsymbol{f}^{\beta}$.

$$\boldsymbol{C}(\boldsymbol{q}, \boldsymbol{s}, t) = \boldsymbol{r}_C^{\alpha,i} - \boldsymbol{r}_C^{\beta,i} = \boldsymbol{R}^{\alpha,i} + \boldsymbol{A}^{\alpha,i}\bar{\boldsymbol{u}}_P^{\alpha,i}(\boldsymbol{s}^{\alpha}) - \boldsymbol{R}^{\beta,i} - \boldsymbol{A}^{\beta,i}\bar{\boldsymbol{u}}_P^{\beta,i}(\boldsymbol{s}^{\beta}) = \boldsymbol{0} \tag{4.69}$$

Inelastic Response: Likewise for completeness, a description of the spring's inelastic behavior is offered. An initial representation of the complete joint combines the contact's inelastic region of behavior with the elastic joint model. It was observed in Chapter 3 that the joint's resistive force reaches a maximum beyond which the equilibrium point beings to move. For planar motion, this can be thought of as a system of stick-slip springs as illustrated in Figure 4.3.

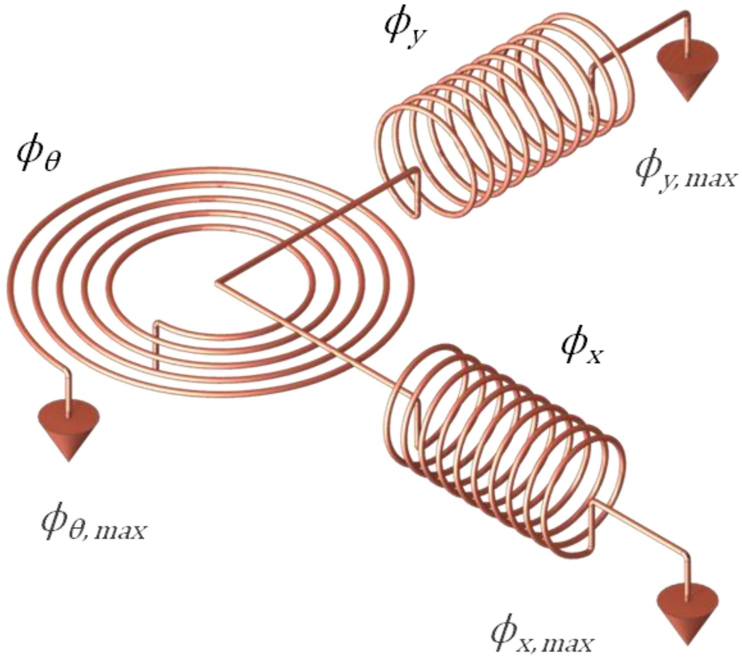

Figure 4.3: A schematic model of a system of stick-slip springs influencing the DOF of planar motion.

To capture this phenomenon in a preliminary model, the spring's linear behavior is modified to include a limit on its available resistive force. This is accomplished by applying two discrete Heaviside step function to the linear spring at the stick-slip transitions, one in either direction:

$$\phi_j^i(\delta) = -k_j\delta + k_j\left(\delta - \phi_{j,max}^i\right)H\left(\delta - \phi_{j,max}^i\right) - k_j\left(\delta + \phi_{j,max}^i\right)\left(H\left(\delta - \phi_{j,max}^i\right) - 1\right) \quad \textbf{(4.70)}$$

where δ is the displacement between the equilibrium contact points on each body along one of the DOF (x , y , or θ). Equation (4.70) is then modified to form a continuous function by substituting the Heaviside step function with the analytic approximation:

$$H(x) = \lim_{n\to\infty}\left(\frac{1}{2} + \frac{1}{\pi}\tan^{-1} nx\right) \quad \textbf{(4.71)}$$

where in practice $n \geq 10$. The nonlinear spring model is plotted in Figure 4.3 with $n = 10$ to illustrate the smooth transition. The corresponding potential energy is:

$$V_j^{\alpha\beta}(\delta) = \frac{-k_j}{2\pi n^2}\left(\left(1 + n^2\left(\delta + \phi_{j,max}^i\right)^2\right)\tan^{-1}\left(n\left(\delta + \phi_{j,max}^i\right)\right) - \left(1 + n^2\left(\delta - \phi_{j,max}^i\right)^2\right)\tan^{-1}\left(n\left(\delta - \phi_{j,max}^i\right)\right)\right) \tag{4.72}$$

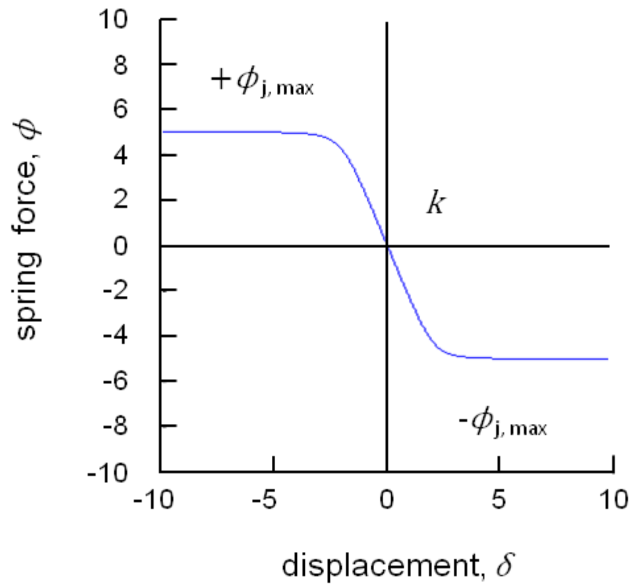

Figure 4.4: Nonlinear spring force vs. displacement plot

Spring systems featuring a greater complexity in their formulations can also be used if future experiments refine the understanding of the adhesive contact's dynamic behavior. Such stick-slip systems are used in the modeling of nonlinear, energy dissipative behavior in the analysis of materials [142] and may prove useful in future multibody formulations that include this nano-joint configuration.

Whether using the simple linear spring model (Equations (4.66) – (4.68)), a single nonlinear spring model (Equations (4.70) – (4.72)), or a more complex system of nonlinear springs [142] to represent the force acting in each direction at the contact, the internal force vector for the joined segments can be represented by:

$$V_{q,1}^{i} = \phi_{j,1}^{i} \tag{4.73}$$

$$V_{q,2}^{i} = \phi_{j,2}^{i} \tag{4.74}$$

$$V_{q,3}^{i} = \left(\phi_{j,2}^{i}\bar{r}_{C,1}^{i} - \phi_{j,1}^{i}\bar{r}_{C,2}^{i}\right)\cos\theta^{\boldsymbol{i}} - \left(\phi_{j,1}^{i}\bar{r}_{C,1}^{i} + \phi_{j,2}^{i}\bar{r}_{C,2}^{i}\right)\sin\theta^{\boldsymbol{i}} \tag{4.75}$$

which can also be written as

$$\boldsymbol{V}_{\boldsymbol{q}}^{i} = [\, V_{q,1}^{i} \quad V_{q,2}^{i} \quad V_{q,3}^{i} \,]^{T} \tag{4.76}$$

Equation (4.76) is the internal force acting on the segment from the spring element. It transforms the force of the nonlinear spring element into an equivalent force-moment system acting at the mass center of the segment.

Contact Area Size: The dependence of the joint's elastic stiffness on the size of the contact area is due to the energy associated with surface area formation as described in Chapter 3. While it is difficult to directly observe how the surface area between two contacting MWCNTs changes, adhesive-contact mechanics offers a means of approximating the relationship. For two cylinders, α and β, oriented perpendicularly to one another, the contact area can be approximated as a circle with a radius a_0 (see Section 3.1). As the cylinders rotate about the contact, the area becomes increasingly eccentric as illustrated in Figure 4.5. This progresses until the area becomes approximately rectangular with a width, w, equal to the diameter of the circular contact area and a length, l, dependent on the resulting overlap between the bodies. For non-parallel orientations of cylinders α and β, the boundary of the contact area can be described in the global frame of reference by:

$$\boldsymbol{c}^{\alpha\beta}(\bar{\theta}_e) = \boldsymbol{r}_C^{\alpha\beta} + \boldsymbol{A}(\theta_a)\,\bar{\boldsymbol{u}}_e^{\alpha\beta}(\bar{\theta}_e), \qquad 0 \le \bar{\theta}_e \le 2\pi \tag{4.77}$$

where $\boldsymbol{c}^{\alpha\beta}$ is a point along the boundary, $\boldsymbol{r}_C^{\alpha\beta}$ is the vector to the center of the contact area, $\boldsymbol{A}$ is the planar rotation matrix, θ_a is the angle of the elliptical apogee in the global reference frame, $\overline{\boldsymbol{u}}_e^{\alpha\beta}$ is a vector to the boundary in the contact's frame of reference, and $\bar{\theta}_e$ is the angle around the boundary in the contact's frame of reference. Here:

$$\overline{\boldsymbol{u}}_e^{\alpha\beta}(\bar{\theta}_e) = [a\ \cos\bar{\theta}_e \quad p\ \sin\bar{\theta}_e] \tag{4.78}$$

where the magnitudes of the apogee (a) and perigee (p) are:

$$a = \left(\frac{1}{\tan\theta_g} + 1\right)a_0, \qquad 0 < \theta_g \leq 2\pi \tag{4.79}$$

$$b = a_0 \tag{4.80}$$

Here, θ_g refers to the smallest angle (or gap angle) between the two body segments. At $\theta_g = 2\pi$ the bodies are perpendicularly oriented and $a = a_0$, which describes the circular contact area. As the bodies rotate toward a parallel orientation, θ_g decreases and a grows. At $\theta_g = 0$, a is infinite and the contact area is approximately rectangular. Subsequently, by mapping the boundary of the contact area using (4.77) – (4.80), all of the segments in each body that fall within the contact area can be determined.

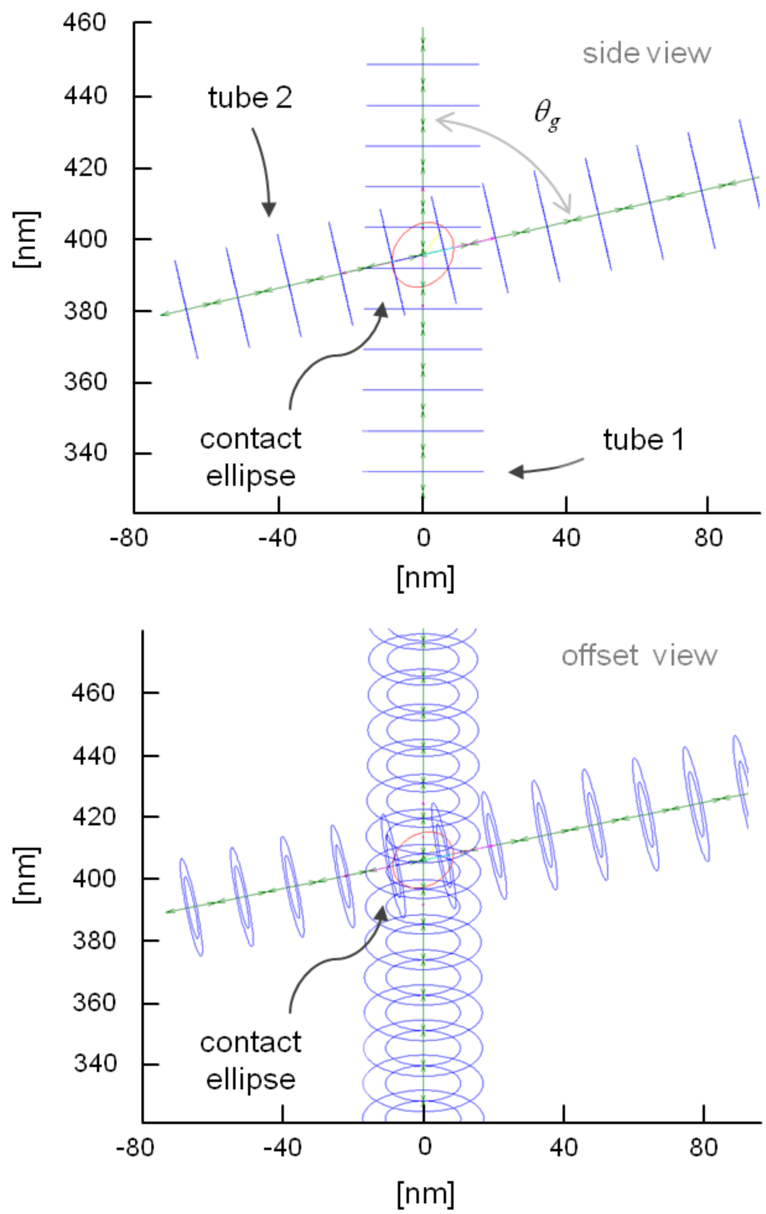

Figure 4.5: Approximation of the contact area boundary between two MWCNTs

In this model, the segments within the boundary are then given an additional constraint that fixes their relative orientation to one another while in the contact area as shown in (4.81). This approximates the effect in which the adhesion influences not just the segments centered within the contact area, but all of the segments within the boundary. These additional constraints are illustrated for body α and are identical for body β:

$$\boldsymbol{C}^{\alpha}\left(\theta^{\boldsymbol{i}},\ \theta^{\ i+1},\dots,\ \theta^{\ n_\alpha}\right) = \begin{bmatrix} \theta^{\boldsymbol{i}} -\ \theta^{\ i+1} - c^{i,i+1} \\ \theta^{\ i+1} -\ \theta^{\ i+2} - c^{i+1,i+2} \\ \vdots \\ \theta^{n_\alpha - 1} -\ \theta^{\ n_\alpha} - c^{n_\alpha - 1, n_\alpha} \end{bmatrix} \tag{4.81}$$

where i through n_α are the segments within the contact area in body α, and c is the angle between the adjacent segments while inside the boundary. As the center of the contact area slips along the curves parameterized by $\boldsymbol{s}$ or the bodies rotate about one another, $\boldsymbol{C}^{\alpha}$ and $\boldsymbol{C}^{\beta}$ necessarily change, requiring the system to be reformulated which can be performed automatically.

Together, the model for the linear and nonlinear behavior of the springs and the variable contact area offer a means by which to capture the adhesive joint's influence on the dynamics of the MWCNT assemblies.

4.4.3 Nano-mechanical System

The equations of motion for the nano-mechanical system are formulated using the models for the flexible bodies and the adhesive joints. The kinematic constraint matrix, $\boldsymbol{C}(\boldsymbol{q}, \boldsymbol{s}, t)$, includes: the compliant-segment representation for each flexible body (4.52), the fixed segments occupying the contact area (4.81), the ground constraints (4.9), the commanded displacements (4.10), and the contact points between the bodies (4.69). The internal force matrix, $\boldsymbol{V_q}$, includes: the contribution of the compliant-segment springs (4.56) and of the nonlinear stick-slip spring (4.76). Finally, the mass matrix, $\boldsymbol{M}$, includes the linear (4.61) and rotational (4.65) inertial terms. Additional sources of effort, $\boldsymbol{e^s}$, can be added instead of or in addition to the commanded displacement terms. These matrices are combined into the LDAE system given in (4.45) – (4.51) to form the equations of motion for the nano-mechanical system.

4.5 Solutions to the Equations of Motion

Numerous methods for solving the equations of motion have been produced in the field of multibody dynamics. The LDAE system given in Section 4.3 is formulated with the constraint forces explicitly stated. This results in a general applicability, it allows for nonlinear constraint forces to be easily implemented, and it is well suit for numeric evaluation [139]. Other formulations of the equations-of-motion are offered in literature and may be based on either the constraint forces or the system's DOF [138]. In general, these reduce the DAE to a system of differential equations and solves it using standard numeric techniques. The under-actuated, nonlinear nature of the nano-mechanical system here does not lend itself to these more compact, efficient, formulations.

Instead the entire system is solved using implicit integration [139]. This can be accomplished in an effective manner by reducing the index-3 LDAE in Section 4.3 to a Gear, Gupta, and Leimkuhler (GGL) index-2 DAE form:

$$\dot{\boldsymbol{q}} - \boldsymbol{f} + \boldsymbol{C}_{\boldsymbol{q}}^{T}\boldsymbol{\nu}_{\boldsymbol{q}} = \boldsymbol{0} \tag{4.82}$$

$$\dot{\boldsymbol{s}} - \boldsymbol{g} + \boldsymbol{C}_{\boldsymbol{s}}^{T}\boldsymbol{\nu}_{\boldsymbol{s}} = \boldsymbol{0} \tag{4.83}$$

$$\boldsymbol{M}\dot{\boldsymbol{f}} + \boldsymbol{C}_{\boldsymbol{q}}^{T}\boldsymbol{\lambda} + \left(\boldsymbol{V}_{\boldsymbol{q}} + \boldsymbol{V}_{\boldsymbol{f}} - \boldsymbol{e}^{s}\right) = \boldsymbol{0} \tag{4.84}$$

$$\boldsymbol{C}_{\boldsymbol{s}}^{T}\boldsymbol{\lambda} = \boldsymbol{0} \tag{4.85}$$

$$\boldsymbol{C} = \boldsymbol{0} \tag{4.86}$$

$$\boldsymbol{C}_{\boldsymbol{q}}\boldsymbol{f} + \boldsymbol{C}_{\boldsymbol{s}}\boldsymbol{g} + \boldsymbol{C}_{t} = \boldsymbol{0} \tag{4.87}$$

where $\boldsymbol{\nu_q}$ and $\boldsymbol{\nu_s}$ are additional multipliers associated with the Jacobians of the constrain matrix, $\boldsymbol{C_q}$ and $\boldsymbol{C_s}$. The GGL index-2 reduction method transforms the index-3 system by removing the acceleration level constraint equation while adding the vector of multipliers. Using a state space representation, this system can be written as:

$$\Phi\left(\boldsymbol{Y}, \dot{\boldsymbol{Y}}, t\right) = \boldsymbol{0} \tag{4.88}$$

where

$$\boldsymbol{Y} = [\boldsymbol{q}^T \quad \boldsymbol{s}^T \quad \boldsymbol{f}^T \quad \boldsymbol{g}^T \quad \boldsymbol{\lambda}^T \quad \boldsymbol{\nu}^T]^T \tag{4.89}$$

and

$$\dot{\boldsymbol{Y}} = [\dot{\boldsymbol{q}}^T \quad \dot{\boldsymbol{s}}^T \quad \dot{\boldsymbol{f}}^T \quad \dot{\boldsymbol{g}}^T \quad \dot{\boldsymbol{\lambda}}^T \quad \dot{\boldsymbol{\nu}}^T]^T \tag{4.90}$$

For the steady-state or quasi-static solution to the nano-mechanical LDAE system in the elastic region of behavior, Equations (4.82) – (4.87) can be further reduced to:

$$\boldsymbol{C}_{\boldsymbol{q}}^T\boldsymbol{\lambda} + \left(\boldsymbol{V_q} - \boldsymbol{e}^s\right) = \boldsymbol{0} \tag{4.91}$$

$$\boldsymbol{C} = \boldsymbol{0} \tag{4.92}$$

with

$$\boldsymbol{Y}_r = [\boldsymbol{q}^T \quad \boldsymbol{\lambda}^T]^T \tag{4.93}$$

which results in

$$\Phi_r(\boldsymbol{Y}_r) = \boldsymbol{0} \tag{4.94}$$

This is possible because in the elastic region of behavior the system is conservative. Here the locations of the contacts resulting from adhesion do not change (removing the need for $\boldsymbol{s}$) and all flow parameters are zero (removing $\boldsymbol{f}$, $\boldsymbol{\nu}$, and the associated state variables). Solving and analyzing the reduced system of equations is the focus of the remainder of Chapter 4.

Equation (4.94) is solved for by minimizing the total potential energy of the system, $\boldsymbol{V}(\boldsymbol{Y}_r)$, through the use of a numeric nonlinear optimization routine:

$$\min_{\boldsymbol{Y}_r} \boldsymbol{V}(\boldsymbol{Y}_r) \tag{4.95}$$

subject to

$$\Phi_r(\boldsymbol{Y}_r) = \boldsymbol{0} \tag{4.96}$$

Vector $\boldsymbol{V}$ contains the potential of the compliant-segment springs given in Equations (4.55) and the nano-joints given in Equation (4.68). The model is constructed in MATLAB and solved for using the function *fmincon.m*, available as part of the Optimization Toolbox.

4.6 Model Validation and Solutions

Applying the reduced equations of motion to the MWCNT mechanisms presented in Chapter 3 is performed in two parts. First the model is calibrated and validated using a series of benchmarks. Then select nano-mechanisms are modeled and compared to the experimentally observed behavior.

4.6.1 Validation

Confirmation of the model's accuracy is achieved by comparing the steady-state solution for $\boldsymbol{Y}_r$ to those given by commercial finite element software. As discussed in Section 4.4.1, the accuracy of compliant-segmentation for approximating the deflection of beams and linkages is dependent on both the number of segments, n, used as well as the stiffness of the torsion springs acting at the segment joints, . In [140] the spring stiffness is calculated as:

$$k_j = \frac{EI}{L} \tag{4.97}$$

where L is the length of the segment, I is the second moment of area, and E is the elastic modulus. This is formulated by analytically determining the bending stiffness of a cantilever subjected to an applied moment, M, at the tip. This assumption is tested to determine how Equation (4.97) might be altered to minimize the total number of segments necessary while maintaining accuracy for both applied moments and lateral loads. To do so, the cantilever stiffness is analyzed analytically under various loading conditions using the Euler-Bernoulli beam equation:

$$I(x)y''''(x) + 2I'(x)y'''(x) + I''(x)y''(x) = 0 \tag{4.98}$$

Equation (4.98) is solved for $y(x)$ using the following equilibrium and boundary conditions.

Loading Configuration A: Lateral Force, P, applied to the tip:

$$EI(x)y'''(x) + EI'(x)y''(x) + P = 0, \qquad x \to L \tag{4.99}$$

$$EI(x)y''(x) + P(x - L) = 0, \qquad x \to L \tag{4.100}$$

$$y'(x) = 0, \qquad x \to 0 \tag{4.101}$$

$$y(x) = 0, \qquad x \to 0 \tag{4.102}$$

Loading Configuration B: Moment, M, applied about the tip:

$$EI(x)y'''(x) + EI'(x)y''(x) = 0, \qquad x \to L \tag{4.103}$$

$$EI(x)y''(x) + M = 0, \qquad x \to L \tag{4.104}$$

$$y'(x) = 0, \qquad x \to 0 \tag{4.105}$$

$$y(x) = 0, \qquad x \to 0 \tag{4.106}$$

For *Configuration A*, with $I'(x) = I''(x) = 0$, the steady-state solutions at the tip gives:

$$y(x) = \delta_A \ = \frac{PL^3}{3EI} \tag{4.107}$$

$$y'(x) = \theta_A \ = \frac{PL^2}{2EI} \tag{4.108}$$

$$k_j\theta_A = \frac{2EI}{L}\theta_A \ = PL \tag{4.109}$$

For *Configuration B*, with $I'(x) = I''(x) = 0$, the steady-state solutions at the tip gives:

$$y(x) = \delta_B \ = \frac{ML^2}{3EI} \tag{4.110}$$

$$y'(x) = \theta_B \ = \frac{ML}{EI} \tag{4.111}$$

$$k_j\theta_B = \frac{EI}{L}\theta_B \ = M \tag{4.112}$$

By comparing Equations (4.109) and (4.112), it can be seen that if Equation (4.97) is implemented in a compliant-segment model without regards to the manner in which the load is applied then the error in θ_p may be as high as 200% when only one segment ($n = 1$) is used.

This dependency on the loading configuration is explored by comparing the tip deflection, tip slope, and shape of a simple cantilever using: (1) the Equations (4.95) – (4.96) and (2) COMSOL Multiphysic v3.3, 3D structural mechanics static module. The model parameters are given in Table 4.1.

Table 4.1: Material, shape, and loading conditions used in initial model validation.

Shape		
cross section	*circular solid*	
profile	*constant*	
Geometric Properties		
r	0.015	[m]
L	0.500	[m]
I	3.976E-08	[m^4]
Materail Properties		
material	*ASTM A36 Steel*	
E	2E+11	[Pa]
ρ	7850	[kg/m^3]
ν	0.26	[-]
Load		
P	22.24	[N]

For the reduced LDAE model, the deflection $y(x)$ and slope $y'(x)$ are calculated at the tip of each segment, s, for configurations with $n = 1$, 2, 4, 8, 16, and 32 total segments. The dependency on n and s is then determined by inspection for *Configuration A* and *Configuration B*:

$$\theta_A(n, s) = \left(\frac{PL^2}{EI}\right)\left(\frac{(1 + 2n - s)s}{2n^2}\right) \tag{4.113}$$

$$\delta_A(n,s) = \sum_{s=1}^{n} \left(\frac{L}{n}\right) \sin\big(\theta_A(n,s)\big) \tag{4.114}$$

$$\theta_B(n,s) = \left(\frac{ML}{EI}\right)\left(\frac{s}{n}\right) \tag{4.115}$$

$$\delta_B(n,s) = \sum_{s=1}^{n} \left(\frac{L}{n}\right) \sin\big(\theta_A(n,s)\big) \tag{4.116}$$

The absolute errors between Equations (4.113) – (4.116) and the analytic equivalents, (4.107), (4.108), (4.110), and (4.111), are systematically evaluated in a loop for a given load (P or $M = PL$). The total number of segments is increased by $n = n + 1$ until the absolute error for θ_A, δ_A, θ_B, and δ_B are below 1%. This method determines that for a cantilever with a constant circular cross-section, 100 segments of the beam are required to reach the desired accuracy.

In an attempt to reduce the total number of segments needed, a scaling factor, c, is introduced to the calculated stiffness k_j. This alters Equations (4.113) and (4.115), multiplying the right-hand side by $(1/c)$. Another search routine is then executed where for each n, c is varied until a minimum in the absolute error is reached. The search is terminated when the minimum absolute error for Equations (4.113) – (4.116) for the current value of c are all below the desired tolerance. The resulting values for n_{min} and c are given in Table 4.2.

Table 4.2: The effect of scaling factor *c* on the minimum number of segments needed for a given accuracy

|error|	c	n_{min}
1.0%	1.000000	100
1.0%	1.009997	88
1.5%	1.018211	58
2.0%	1.020103	44

While the dependency of δ and θ on n and s can be determined by inspection for constant cross-section beams, the relationship shows an undetermined dependency on R_o, R_i, α_o, and α_i for the variable cross-section tubes. As a first approximation, the values for the constant cross-section beam with 2% accuracy are used throughout the remainder of this chapter to model flexible beams with variable cross-section.

4.6.2 Solutions

Three configurations of MWCNT beams are used to demonstrate the use of the reduced LDAE system: 1) a single MWCNT undergoing a commanded displacement of the tip with a fixed slope at the tip, 2) two MWCNTs oriented orthogonally, connected by a linear nano-joint, with the horizontal link undergoing a commanded displacement, and 3) three MWCNTs assembled into a four-bar mechanism with one of the rockers undergoing a commanded displacement. These three demonstrations mimic portions of the experimental procedures described in Chapter 3.

Demonstration 1 mimics the forward bending procedure from Experiment Set 1 in Chapter 3, using MWCNT #8 from Table 3.1 oriented perpendicular to the substrate. The base segment is firmly attached to ground with $\boldsymbol{q}^1 = [0.0\ \text{nm} \quad -90.9\ \text{nm} \quad 1.5708\ \text{rad}]^T$, and the segment 8.0 μm from the base (tip, $i = 45$) is rotationally constrained. The tip segment is then subjected to a 0.89 μm displacement parallel to the surface of the substrate which is the average recorded for this MWCNT during the experiment. The resulting deformed shape is shown in Figure 4.6. At equilibrium, the end of the tip segment is located at $\boldsymbol{r}_{tip} = [889.9\ \text{nm} \quad 7938.8\ \text{nm}]^T$. The final tip location deviates from 8.0 μm for two reasons: (1) each segment is assumed to be rigid, prohibiting strain in the model, (2) unlike in the experiment where the adhered length of the tube may slip off of the cantilever to make up for this change in length, the model only accounts for the 8.0 μm that is initially 'free' from contact with the cantilever.

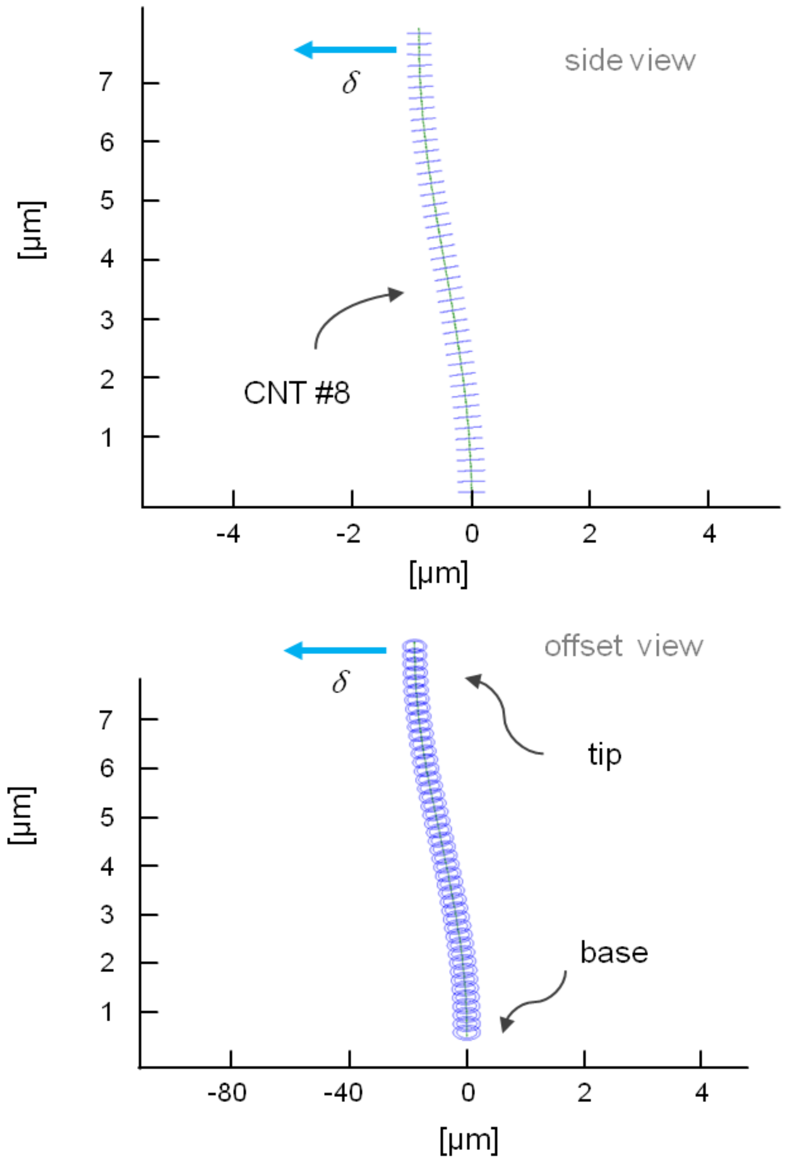

Figure 4.6: Schematic representations of demonstration 1 where a single MWCNT is subject to a command displacement at its tip

Demonstration 2 uses MWCNTs #1 and #7 to form a two link mechanism joined by a linear nano-joint, representing Procedures 1.1 and 1.2 from Experiment Set 2. Tube #1 is fixed to the substrate at its base with $\boldsymbol{q}_{base}^{1} = [0.0\text{ nm} \quad -90.9\text{ nm} \quad 1.5708\text{ rad}]^{T}$ and the orientation of tube #7's base is fixed perpendicularly to Tube #1 with an initial location of $\boldsymbol{q}_{base}^{2} = [5112.2\text{ nm} \quad 7140.0\text{ nm} \quad 3.1416\text{ rad}]^{T}$. Tube #7 is then subjected to a 0.59 μm displacement parallel to the substrate. The magnitude of this displacement is chosen by dividing the measured deflection of the contact point, $\delta = 0.38$ μm (shown in

Table 3.8, Proc. 1.1) by the average slope of the input/output curve, $s = 0.65$, (shown in Figure 3.16) used to determine the contact stiffness, k_j. The resulting deformation is illustrated in Figure 4.7 which shows the contact moving 0.40 μm and the angle between the bodies in contact increasing to 1.6458 rad. This increase in the displacement can be attributed to the uncertainty in knowing the precise section of CNT #7 occupying the gap between the manipulator and the contact as well as the fact that the entire CNT is discretized into 44 segments instead of just the gap region (reducing the number of segments in the deflected region which decreases the accuracy of the model).

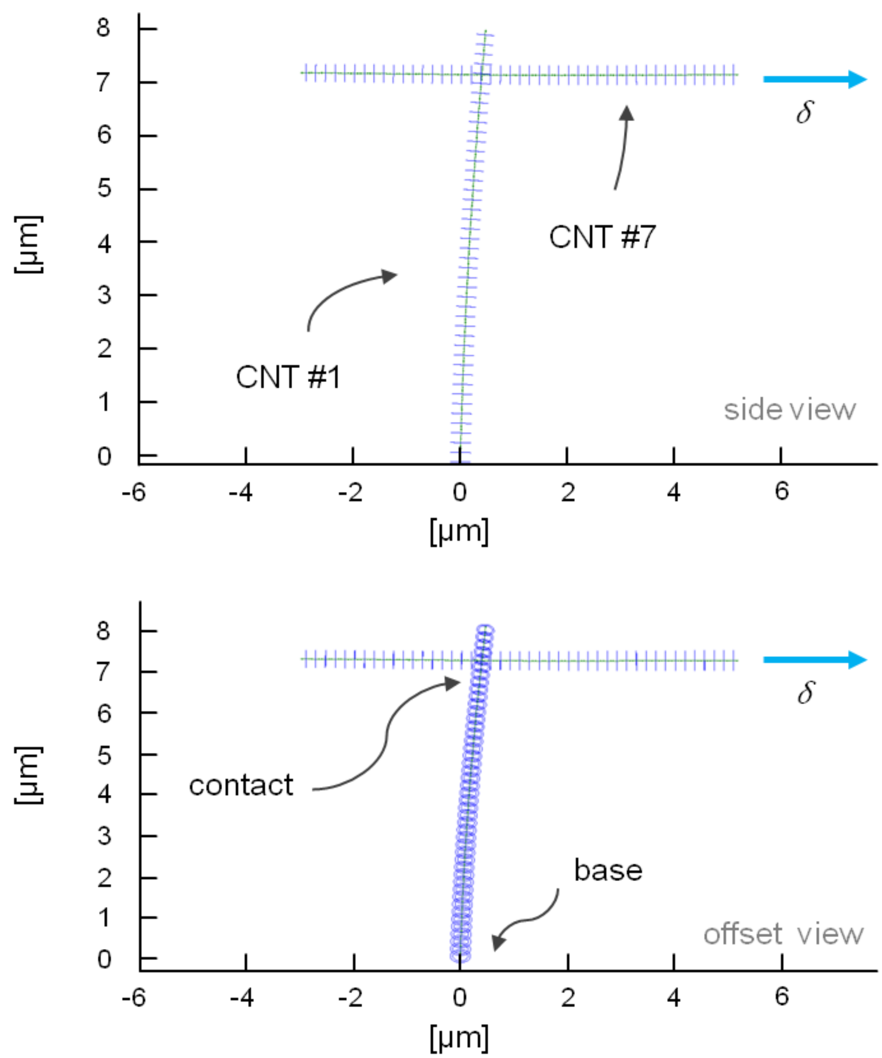

Figure 4.7: Schematic representations of demonstration 2 where a two-linke MWCNT chain is subjected to a commanded displacement

Demonstration 3 uses MWCNTs #5, #6, and #10 to form a double-rocker four-bar mechanism representing Experiment Set 3 from Chapter 3. Tube #6 and #10 are firmly attached to the substrate 3.5 μm apart. Tube # 5 is attached to tube #6 a distance of 6.1 μm from the substrate and tube #10 a distance of 7.8 μm from the substrate. Tube #6 undergoes a commanded displacement applied at a segment 6.5 μm from the base for a distance of 0.80 μm toward Tube #10, parallel to the substrate. The result is shown in Figure 4.8. Experimentally, the output was observed to move 0.35 μm along $-\boldsymbol{x}$ while in this model the displacement is closer to 0.35 μm. Additionally, CNT #6 exhibits a larger radius of curvature than that experimentally observed. These differences may be attributed to model and measurement uncertainty

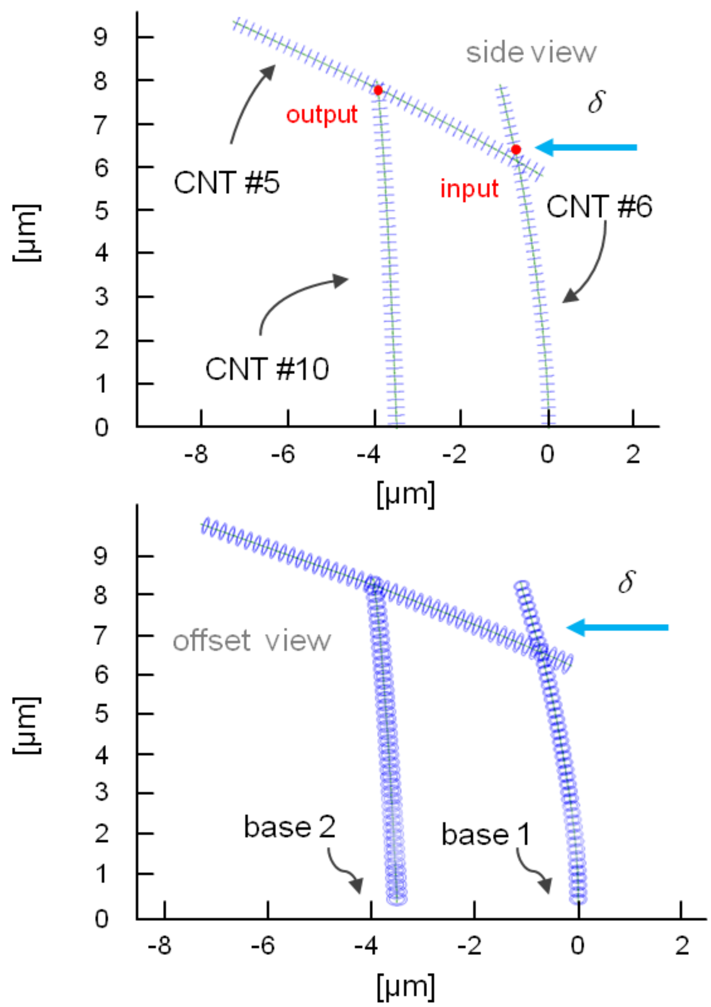

Figure 4.8: Schematic representations ofdemonstration 3 showing the activation of a four-bar MWCNT mechanism

Each demonstration (1-3) provides a model analogous to portions of the experiments performed in Chapter 3. When the uncertainty in the experimental measurement and the accuracy of the model are combined in quadrature, the resulting expected uncertainty in Demonstration 1 is 9.2%, in Demonstration 2 it is 29.2%, and in Demonstration 3 it is 25.3%. When accounting for this uncertainty, all three models show motion similar to that experimentally observed.

4.7 Discussion and Conclusion

Chapter 4 has presented an approach to modeling the nano-scale adhesive joint behavior as part of a multibody system. This has been performed in the pursuit of a model capable of capturing the nonlinear, nonconservative, nonholonomic behavior of the nano-joint. To that end, a generalized model has been formulated using LDAEs addressing both the flexible nature of the nanoscopic components and the nonlinear nature of the joints. Suggestions have been presenting as to how the model may be expanding to encompass the full range of behaviors observed in Chapter 3. Additionally, solutions to various configurations have been presented as a demonstration of nano-multibody modeling under restricted conditions. Capturing the full behavior of the nano-joint in a multibody model may advance the abilities to controllably, automatically manipulate and assemble nano-mechanical mechanisms using contact techniques.

5 CLOSURE

5.1 Conclusion

Motivated by the potential engineering and societal benefits of advancing assembly-based nanomanufacturing, this work has pursued experimental and theoretical investigations into a select set of fundamental scientific issues central to enabling the manipulation of MWCNTs. This has included three specific aims: (1) the observation of MWCNTs and measurement of their structural and pseudo-material properties, (2) the observation and characterization of the 'joint-like' contact formed between nano-scale bodies in certain configurations, and (3) the validation of an initial model mathematically capturing the observed kinematics. These objectives have been successfully realized in this thesis work. The remainder of this chapter summarizes the actives performed, results and conclusions from each research objective, the research contributions, and proposed improvements for future work.

5.1.1 Specific Aim 1

The first aim sought to observe and measure the structural properties of MWCNTs for use in contact nano-manipulation. This included creating the means by which to visualize and manipulate MWCNTs as well as investigating the extent to which conventional continuum mechanics can be used to model the observed behavior. A novel, dexterous nanomanipulation system was successfully constructed as part of this aim with the capability of repeatedly exploring the mechanical manipulation of specific MWCNTs. Through the use of this system, ten specific MWCNTs were identified and characterized with regards to their structural stiffness, pseudo-elastic modulus, and deflected shape. It was found that (1) the structural stiffness varied with the geometry of the tube, (2) the pseudo-elastic modulus was lower than expected and may vary greatly between tubes, and (3) even with the uncertainty in the material elasticity, the Euler-Bernoulli beam equation could be used to give a reliable approximation of the deformed MWCNT shape.

5.1.2 Specific Aim 2

The second aim sought to observe and measure the adhesion between nano-scale components and its effect on the motion of bodies when constrained within mechanical grasps and assemblies. This was achieved through the use of the nanomanipulation system to dexterously assemble multiple mechanisms constructed from the MWCNTs characterized as part of Aim 1. A systematic study was performed on two types of nano-mechanisms: a kinematic pair and a four-bar mechanism. By studying the kinematic pair it was shown that: (1) van der Waals interactions cause a stable elastic bond or joint to form between MWCNTs which can resist relative motion between the bodies, (2) the elasticity of this joint is dependent on the total area of contact, (3) while stable, the joint still allows three planar degrees of freedom between the bodies, (4) above a given threshold, this elastic joint yields to inelastic motion of the two MWCNTs, (5) this threshold is higher for linear motion along the surface than for rotational motion about the surface when the tubes are oriented perpendicularly, (6) Joule heating of the MWCNT pair measurably raised the value of the threshold between elastic and inelastic motion but appeared to have no effect on the elastic stiffness prior to slipping. These observations were employed to construct the four-bar mechanism. By studying the four-bar mechanism it was shown that, (1) a multi-link nano-mechanical mechanism can be constructed using contact manipulation, and (2) mechanical motion can be repeatedly transferred through multiple flexible nano-structures and joints. Based on this demonstration of a functional prototype four-bar mechanism assembled from three individual carbon nanotubes through mechanical manipulation, it is concluded that it is feasible to create "kinematic joints" between CNTs through nanomanipulation and assembly-based nanomanufacturing may be exploited in the future to build more complex nano-scale structures and machines such as those envisioned in Figure 1.1.

5.1.3 Specific Aim 3

The third aim sought to construct a multibody model capable of representing the interactions observed in the pursuit of Aims 1 and 2. The MWCNTs were shown to exhibit notable elastic flexibility over a range of displacements. Additionally, the jointed behavior was shown to approximate a nonlinear, nonconservative, nonholonomic constraint. Combining both of these behaviors into a single model proved daunting. For the purposes of suggesting future modeling methods, an LDAE formulation was adopted and modeling techniques for flexible bodies with nonholonomic constraints were discussed. A simplified model was solved for in which the joints constraining the flexible MWCNTs where only strained within their elastic limits. This showed that,within the uncertainty of the system,the model could describe: (1) the static deflection of a single MWCNT by means of the micro-cantilever, (2) the static bending of a MWCNT pair, and (3) the static deflection of a four-bar MWCNT mechanism.

5.2 Research Contributions

Through the construction of the nanomanipulation system, the experimentation with nano-multibody systems, and the modeling of the observed behavior, unique contributions to the current field of nanomanipulation and assembly-based nanomanufacturing have been made in this thesis. Major scientific and technical contributions of this thesis include:

1. Demonstration of the dexterous mechanical manipulation and assembly of free-standing MWCNTs visualized by means of optical microscopy.

2. The description and characterization of adhesive contact between MWCNTs as a kinematic joint featuring behavior unique to the micro-/nano-scale.

5.3 Proposed Improvements and Future Work

As an exploratory investigation into contact nanomanipulation, there are many aspects of the materials, tools, and theory that can be improved upon in future work.

First among the improvements is the quality of the nano-scale materials. As demonstrated, the MWCNTs used in this work are of low quality. The internal atomic structure of the tubes featured graphitic walls with basal planes that were not parallel to the axis of the tube. The walls were far thinner than desired and numerous thin sheets of graphene protruded into the central void of each tube. The walls also demonstrated variable inner and outer radii and structural kinks. Future work should use MWCNTs featuring smaller variation in shape and structure between tubes, walls with graphitic planes parallel to the tube axis, and smaller maximum outer diameters.

Second would be improvements to the manipulation and visualization systems. While the manipulators were controllable remotely, both the positioner on which the substrate was carried and the positioning and focusing of the microscope were performed manually. Computer control of the carrier and the microscope would greatly improve the accuracy and rate with which experiments could be performed. An improvement in the accuracy of the manipulators would also benefit the experimentation. The system discussed here had a positioning accuracy of 80 nm. This could be improved by either adding an additional set of fine actuators atop the current system or using miniaturized, compliant, chip-scale manipulation systems with the desired range and DOF. Finally, a faster, higher resolution camera system could potentially capture more of the dynamic behavior of the multibody system leading up to and during slipping events.

Third, would be an increase in the number of experiments performed. With a faster more accurate manipulation system and better raw materials, a large number of experimental runs could be executed for a larger population of MWCNTs. This would be important for reliably determining the structural and mechanical properties of MWCNTs, the joints between them, and the possible welds formed for the purposes of nano-mechanism design and assembly.

Fourth would be improvement to the mathematical model of the nano-multibody system. This would include validation of the dynamic LDAE formulation for the inelastic region of behavior for the nano-joint. From here, expansion into a fully three-dimensional, spatial representation of the workspace would improve the accuracy of the model.

Fifth would be the creation of an automated manipulation system from the improved mathematical model. This could result in systems capable of calculating necessary path plans for the automatic manipulation and assembly of nano-scale structures. Additionally, it could potentially apply and detect the proper electrical current necessary to form joints of specific elasticity and strength.

While many questions were discovered during the course of this work and many improvements which might help answer them, the tools and theories presented represent a step toward the creation of an automated, dexterous nanomanipulation and assembly system. Contact nanomanipulation may someday produce structures and mechanisms in the quantity and complexity necessary to meaningfully impact both engineering and science to the betterment of human kind.

6 APPENDEX

Explicit solution to the system of equations formed from Equations (3.5) – (3.11), given in a format easily copied and entered into and modified for a computer function:

```
y = (P*(4*(Ro*ai - Ri*ao)*ArcCot[(Ro*ai - Ri*ao)/(Ri*ai + Ro*ao)]^2 -
      2*Ri*ai*ArcCot[(Ro*ai - Ri*ao)/(Ri*ai + Ro*ao + x*(ai^2 + ao^2))]*
      Log[Ri - Ro] + 2*Ro*ai*ArcCot[(Ro*ai - Ri*ao)/(Ri*ai +
      Ro*ao + x*(ai^2 + ao^2))]*Log[Ri - Ro] - 2*x*ai^2*
      ArcCot[(Ro*ai - Ri*ao)/(Ri*ai + Ro*ao + x*(ai^2 + ao^2))]*Log[Ri - Ro] +
      2*Ri*ao*ArcCot[(Ro*ai - Ri*ao)/(Ri*ai + Ro*ao + x*(ai^2 + ao^2))]*
      Log[Ri - Ro] - 2*Ro*ao*ArcCot[(Ro*ai - Ri*ao)/(Ri*ai +
      Ro*ao + x*(ai^2 + ao^2))]*Log[Ri - Ro] + 4*x*ai*ao*
      ArcCot[(Ro*ai - Ri*ao)/(Ri*ai + Ro*ao + x*(ai^2 + ao^2))]*Log[Ri - Ro] -
      2*x*ao^2*ArcCot[(Ro*ai - Ri*ao)/(Ri*ai + Ro*ao + x*(ai^2 + ao^2))]*
      Log[Ri - Ro] - 2*Ri*ai*ArcCot[(Ro*ai - Ri*ao)/(Ri*ai +
      Ro*ao + x*(ai^2 + ao^2))]*Log[Ri + Ro] - 2*Ro*ai*
      ArcCot[(Ro*ai - Ri*ao)/(Ri*ai + Ro*ao + x*(ai^2 + ao^2))]*Log[Ri + Ro] -
      2*x*ai^2*ArcCot[(Ro*ai - Ri*ao)/(Ri*ai + Ro*ao + x*(ai^2 + ao^2))]*
      Log[Ri + Ro] - 2*Ri*ao*ArcCot[(Ro*ai - Ri*ao)/(Ri*ai +
      Ro*ao + x*(ai^2 + ao^2))]*Log[Ri + Ro] - 2*Ro*ao*
      ArcCot[(Ro*ai - Ri*ao)/(Ri*ai + Ro*ao + x*(ai^2 + ao^2))]*Log[Ri + Ro] -
      4*x*ai*ao*ArcCot[(Ro*ai - Ri*ao)/(Ri*ai + Ro*ao + x*(ai^2 + ao^2))]*
      Log[Ri + Ro] - 2*x*ao^2*ArcCot[(Ro*ai - Ri*ao)/(Ri*ai +
      Ro*ao + x*(ai^2 + ao^2))]*Log[Ri + Ro] + 4*Ro*ai*Log[Ri - Ro]*
      Log[Ri + Ro] - 4*Ri*ao*Log[Ri - Ro]*Log[Ri + Ro] + 2*Ri*ai*
      ArcCot[(Ro*ai - Ri*ao)/(Ri*ai + Ro*ao + x*(ai^2 + ao^2))]*
      Log[Ri^2 + Ro^2] + 2*x*ai^2*ArcCot[(Ro*ai - Ri*ao)/(Ri*ai +
      Ro*ao + x*(ai^2 + ao^2))]*Log[Ri^2 + Ro^2] + 2*Ro*ao*
      ArcCot[(Ro*ai - Ri*ao)/(Ri*ai + Ro*ao + x*(ai^2 + ao^2))]*
      Log[Ri^2 + Ro^2] + 2*x*ao^2*ArcCot[(Ro*ai - Ri*ao)/(Ri*ai +
      Ro*ao + x*(ai^2 + ao^2))]*Log[Ri^2 + Ro^2] -
      2*Ro*ai*Log[Ri - Ro]*Log[Ri^2 + Ro^2] +
      2*Ri*ao*Log[Ri - Ro]*Log[Ri^2 + Ro^2] -
      2*Ro*ai*Log[Ri + Ro]*Log[Ri^2 + Ro^2] +
      2*Ri*ao*Log[Ri + Ro]*Log[Ri^2 + Ro^2] +
      Ro*ai*Log[Ri^2 + Ro^2]^2 - Ri*ao*Log[Ri^2 + Ro^2]^2 + 2*Ri*ai*
      ArcCot[(Ro*ai - Ri*ao)/(Ri*ai + Ro*ao + x*(ai^2 + ao^2))]*
      Log[Ri - Ro + L*ai - L*ao] - 2*Ro*ai*ArcCot[(Ro*ai - Ri*ao)/(Ri*ai +
      Ro*ao + x*(ai^2 + ao^2))]*Log[Ri - Ro + L*ai - L*ao] + 2*x*ai^2*
      ArcCot[(Ro*ai - Ri*ao)/(Ri*ai + Ro*ao + x*(ai^2 + ao^2))]*
      Log[Ri - Ro + L*ai - L*ao] - 2*Ri*ao*ArcCot[(Ro*ai - Ri*ao)/(Ri*ai +
      Ro*ao + x*(ai^2 + ao^2))]*Log[Ri - Ro + L*ai - L*ao] + 2*Ro*ao*
      ArcCot[(Ro*ai - Ri*ao)/(Ri*ai + Ro*ao + x*(ai^2 + ao^2))]*
      Log[Ri - Ro + L*ai - L*ao] - 4*x*ai*ao*ArcCot[(Ro*ai - Ri*ao)/(Ri*ai +
      Ro*ao + x*(ai^2 + ao^2))]*Log[Ri - Ro + L*ai - L*ao] + 2*x*ao^2*
      ArcCot[(Ro*ai - Ri*ao)/(Ri*ai + Ro*ao + x*(ai^2 + ao^2))]*
      Log[Ri - Ro + L*ai - L*ao] - 2*Ri*ai*Log[Ri + Ro]*
      Log[Ri - Ro + L*ai - L*ao] - 2*Ro*ai*Log[Ri + Ro]*
      Log[Ri - Ro + L*ai - L*ao] - 2*x*ai^2*Log[Ri + Ro]*
```

Log[Ri - Ro + L*ai - L*ao] + 2*Ri*ao*Log[Ri + Ro]*
Log[Ri - Ro + L*ai - L*ao] + 2*Ro*ao*Log[Ri + Ro]*
Log[Ri - Ro + L*ai - L*ao] + 2*x*ao^2*Log[Ri + Ro]*
Log[Ri - Ro + L*ai - L*ao] + Ri*ai*Log[Ri^2 + Ro^2]*
Log[Ri - Ro + L*ai - L*ao] + Ro*ai*Log[Ri^2 + Ro^2]*
Log[Ri - Ro + L*ai - L*ao] + x*ai^2*Log[Ri^2 + Ro^2]*
Log[Ri - Ro + L*ai - L*ao] - Ri*ao*Log[Ri^2 + Ro^2]*
Log[Ri - Ro + L*ai - L*ao] - Ro*ao*Log[Ri^2 + Ro^2]*
Log[Ri - Ro + L*ai - L*ao] - x*ao^2*Log[Ri^2 + Ro^2]*
Log[Ri - Ro + L*ai - L*ao] + 2*Ri*ai*Log[Ri + Ro]*
Log[Ri - Ro + x*ai - x*ao] - 2*Ro*ai*Log[Ri + Ro]*
Log[Ri - Ro + x*ai - x*ao] + 2*x*ai^2*Log[Ri + Ro]*
Log[Ri - Ro + x*ai - x*ao] + 2*Ri*ao*Log[Ri + Ro]*
Log[Ri - Ro + x*ai - x*ao] - 2*Ro*ao*Log[Ri + Ro]*
Log[Ri - Ro + x*ai - x*ao] - 2*x*ao^2*Log[Ri + Ro]*
Log[Ri - Ro + x*ai - x*ao] - Ri*ai*Log[Ri^2 + Ro^2]*
Log[Ri - Ro + x*ai - x*ao] + Ro*ai*Log[Ri^2 + Ro^2]*
Log[Ri - Ro + x*ai - x*ao] - x*ai^2*Log[Ri^2 + Ro^2]*
Log[Ri - Ro + x*ai - x*ao] - Ri*ao*Log[Ri^2 + Ro^2]*
Log[Ri - Ro + x*ai - x*ao] + Ro*ao*Log[Ri^2 + Ro^2]*
Log[Ri - Ro + x*ai - x*ao] + x*ao^2*Log[Ri^2 + Ro^2]*
Log[Ri - Ro + x*ai - x*ao] + 2*Ri*ai*
ArcCot[(Ro*ai - Ri*ao)/(Ri*ai + Ro*ao + x*(ai^2 + ao^2))]*
Log[Ri + Ro + L*(ai + ao)] + 2*Ro*ai*
ArcCot[(Ro*ai - Ri*ao)/(Ri*ai + Ro*ao + x*(ai^2 + ao^2))]*
Log[Ri + Ro + L*(ai + ao)] + 2*x*ai^2*
ArcCot[(Ro*ai - Ri*ao)/(Ri*ai + Ro*ao + x*(ai^2 + ao^2))]*
Log[Ri + Ro + L*(ai + ao)] + 2*Ri*ao*
ArcCot[(Ro*ai - Ri*ao)/(Ri*ai + Ro*ao + x*(ai^2 + ao^2))]*
Log[Ri + Ro + L*(ai + ao)] + 2*Ro*ao*
ArcCot[(Ro*ai - Ri*ao)/(Ri*ai + Ro*ao + x*(ai^2 + ao^2))]*
Log[Ri + Ro + L*(ai + ao)] + 4*x*ai*ao*
ArcCot[(Ro*ai - Ri*ao)/(Ri*ai + Ro*ao + x*(ai^2 + ao^2))]*
Log[Ri + Ro + L*(ai + ao)] + 2*x*ao^2*
ArcCot[(Ro*ai - Ri*ao)/(Ri*ai + Ro*ao + x*(ai^2 + ao^2))]*
Log[Ri + Ro + L*(ai + ao)] + 2*Ri*ai*Log[Ri - Ro]*
Log[Ri + Ro + L*(ai + ao)] - 2*Ro*ai*Log[Ri - Ro]*
Log[Ri + Ro + L*(ai + ao)] + 2*x*ai^2*Log[Ri - Ro]*
Log[Ri + Ro + L*(ai + ao)] + 2*Ri*ao*Log[Ri - Ro]*
Log[Ri + Ro + L*(ai + ao)] - 2*Ro*ao*Log[Ri - Ro]*
Log[Ri + Ro + L*(ai + ao)] - 2*x*ao^2*Log[Ri - Ro]*
Log[Ri + Ro + L*(ai + ao)] - Ri*ai*Log[Ri^2 + Ro^2]*
Log[Ri + Ro + L*(ai + ao)] + Ro*ai*Log[Ri^2 + Ro^2]*
Log[Ri + Ro + L*(ai + ao)] - x*ai^2*Log[Ri^2 + Ro^2]*
Log[Ri + Ro + L*(ai + ao)] - Ri*ao*Log[Ri^2 + Ro^2]*
Log[Ri + Ro + L*(ai + ao)] + Ro*ao*Log[Ri^2 + Ro^2]*
Log[Ri + Ro + L*(ai + ao)] + x*ao^2*Log[Ri^2 + Ro^2]*
Log[Ri + Ro + L*(ai + ao)] - 2*Ri*ai*Log[Ri - Ro + x*ai - x*ao]*
Log[Ri + Ro + L*(ai + ao)] + 2*Ro*ai*Log[Ri - Ro + x*ai - x*ao]*
Log[Ri + Ro + L*(ai + ao)] - 2*x*ai^2*Log[Ri - Ro + x*ai - x*ao]*
Log[Ri + Ro + L*(ai + ao)] - 2*Ri*ao*Log[Ri - Ro + x*ai - x*ao]*
Log[Ri + Ro + L*(ai + ao)] + 2*Ro*ao*Log[Ri - Ro + x*ai - x*ao]*
Log[Ri + Ro + L*(ai + ao)] + 2*x*ao^2*Log[Ri - Ro + x*ai - x*ao]*
Log[Ri + Ro + L*(ai + ao)] - 2*Ri*ai*Log[Ri - Ro]*
Log[Ri + Ro + x*(ai + ao)] - 2*Ro*ai*Log[Ri - Ro]*

Log[Ri + Ro + x*(ai + ao)] - 2*x*ai^2*Log[Ri - Ro]*
Log[Ri + Ro + x*(ai + ao)] + 2*Ri*ao*Log[Ri - Ro]*
Log[Ri + Ro + x*(ai + ao)] + 2*Ro*ao*Log[Ri - Ro]*
Log[Ri + Ro + x*(ai + ao)] + 2*x*ao^2*Log[Ri - Ro]*
Log[Ri + Ro + x*(ai + ao)] + Ri*ai*Log[Ri^2 + Ro^2]*
Log[Ri + Ro + x*(ai + ao)] + Ro*ai*Log[Ri^2 + Ro^2]*
Log[Ri + Ro + x*(ai + ao)] + x*ai^2*Log[Ri^2 + Ro^2]*
Log[Ri + Ro + x*(ai + ao)] - Ri*ao*Log[Ri^2 + Ro^2]*
Log[Ri + Ro + x*(ai + ao)] - Ro*ao*Log[Ri^2 + Ro^2]*
Log[Ri + Ro + x*(ai + ao)] - x*ao^2*Log[Ri^2 + Ro^2]*
Log[Ri + Ro + x*(ai + ao)] + 2*Ri*ai*Log[Ri - Ro + L*ai - L*ao]*
Log[Ri + Ro + x*(ai + ao)] + 2*Ro*ai*Log[Ri - Ro + L*ai - L*ao]*
Log[Ri + Ro + x*(ai + ao)] + 2*x*ai^2*Log[Ri - Ro + L*ai - L*ao]*
Log[Ri + Ro + x*(ai + ao)] - 2*Ri*ao*Log[Ri - Ro + L*ai - L*ao]*
Log[Ri + Ro + x*(ai + ao)] - 2*Ro*ao*Log[Ri - Ro + L*ai - L*ao]*
Log[Ri + Ro + x*(ai + ao)] - 2*x*ao^2*Log[Ri - Ro + L*ai - L*ao]*
Log[Ri + Ro + x*(ai + ao)] - 2*Ri*ai*
ArcCot[(Ro*ai - Ri*ao)/(Ri*ai + Ro*ao + x*(ai^2 + ao^2))]*
Log[Ri^2 + Ro^2 + 2*L*Ri*ai + 2*L*Ro*ao + L^2*(ai^2 + ao^2)] - 2*x*ai^2*
ArcCot[(Ro*ai - Ri*ao)/(Ri*ai + Ro*ao + x*(ai^2 + ao^2))]*
Log[Ri^2 + Ro^2 + 2*L*Ri*ai + 2*L*Ro*ao + L^2*(ai^2 + ao^2)] - 2*Ro*ao*
ArcCot[(Ro*ai - Ri*ao)/(Ri*ai + Ro*ao + x*(ai^2 + ao^2))]*
Log[Ri^2 + Ro^2 + 2*L*Ri*ai + 2*L*Ro*ao + L^2*(ai^2 + ao^2)] - 2*x*ao^2*
ArcCot[(Ro*ai - Ri*ao)/(Ri*ai + Ro*ao + x*(ai^2 + ao^2))]*
Log[Ri^2 + Ro^2 + 2*L*Ri*ai + 2*L*Ro*ao + L^2*(ai^2 + ao^2)] -
Ri*ai*Log[Ri - Ro]*Log[Ri^2 + Ro^2 + 2*L*Ri*ai + 2*L*Ro*ao +
L^2*(ai^2 + ao^2)] + Ro*ai*Log[Ri - Ro]*
Log[Ri^2 + Ro^2 + 2*L*Ri*ai + 2*L*Ro*ao + L^2*(ai^2 + ao^2)] -
x*ai^2*Log[Ri - Ro]*Log[Ri^2 + Ro^2 + 2*L*Ri*ai + 2*L*Ro*ao +
L^2*(ai^2 + ao^2)] - Ri*ao*Log[Ri - Ro]*
Log[Ri^2 + Ro^2 + 2*L*Ri*ai + 2*L*Ro*ao + L^2*(ai^2 + ao^2)] +
Ro*ao*Log[Ri - Ro]*Log[Ri^2 + Ro^2 + 2*L*Ri*ai + 2*L*Ro*ao +
L^2*(ai^2 + ao^2)] + x*ao^2*Log[Ri - Ro]*
Log[Ri^2 + Ro^2 + 2*L*Ri*ai + 2*L*Ro*ao + L^2*(ai^2 + ao^2)] +
Ri*ai*Log[Ri + Ro]*Log[Ri^2 + Ro^2 + 2*L*Ri*ai + 2*L*Ro*ao +
L^2*(ai^2 + ao^2)] + Ro*ai*Log[Ri + Ro]*
Log[Ri^2 + Ro^2 + 2*L*Ri*ai + 2*L*Ro*ao + L^2*(ai^2 + ao^2)] +
x*ai^2*Log[Ri + Ro]*Log[Ri^2 + Ro^2 + 2*L*Ri*ai + 2*L*Ro*ao +
L^2*(ai^2 + ao^2)] - Ri*ao*Log[Ri + Ro]*
Log[Ri^2 + Ro^2 + 2*L*Ri*ai + 2*L*Ro*ao + L^2*(ai^2 + ao^2)] -
Ro*ao*Log[Ri + Ro]*Log[Ri^2 + Ro^2 + 2*L*Ri*ai + 2*L*Ro*ao +
L^2*(ai^2 + ao^2)] - x*ao^2*Log[Ri + Ro]*
Log[Ri^2 + Ro^2 + 2*L*Ri*ai + 2*L*Ro*ao + L^2*(ai^2 + ao^2)] -
Ro*ai*Log[Ri^2 + Ro^2]*Log[Ri^2 + Ro^2 + 2*L*Ri*ai + 2*L*Ro*ao +
L^2*(ai^2 + ao^2)] + Ri*ao*Log[Ri^2 + Ro^2]*
Log[Ri^2 + Ro^2 + 2*L*Ri*ai + 2*L*Ro*ao + L^2*(ai^2 + ao^2)] +
Ri*ai*Log[Ri - Ro + x*ai - x*ao]*Log[Ri^2 + Ro^2 + 2*L*Ri*ai +
2*L*Ro*ao + L^2*(ai^2 + ao^2)] - Ro*ai*Log[Ri - Ro + x*ai - x*ao]*
Log[Ri^2 + Ro^2 + 2*L*Ri*ai + 2*L*Ro*ao + L^2*(ai^2 + ao^2)] +
x*ai^2*Log[Ri - Ro + x*ai - x*ao]*
Log[Ri^2 + Ro^2 + 2*L*Ri*ai + 2*L*Ro*ao + L^2*(ai^2 + ao^2)] +
Ri*ao*Log[Ri - Ro + x*ai - x*ao]*Log[Ri^2 + Ro^2 + 2*L*Ri*ai +
2*L*Ro*ao + L^2*(ai^2 + ao^2)] - Ro*ao*Log[Ri - Ro + x*ai - x*ao]*
Log[Ri^2 + Ro^2 + 2*L*Ri*ai + 2*L*Ro*ao + L^2*(ai^2 + ao^2)] -
x*ao^2*Log[Ri - Ro + x*ai - x*ao]*Log[Ri^2 + Ro^2 + 2*L*Ri*ai +

2*L*Ro*ao + L^2*(ai^2 + ao^2)] - Ri*ai*Log[Ri + Ro + x*(ai + ao)]*
Log[Ri^2 + Ro^2 + 2*L*Ri*ai + 2*L*Ro*ao + L^2*(ai^2 + ao^2)] -
Ro*ai*Log[Ri + Ro + x*(ai + ao)]*Log[Ri^2 + Ro^2 + 2*L*Ri*ai +
2*L*Ro*ao + L^2*(ai^2 + ao^2)] - x*ai^2*Log[Ri + Ro + x*(ai + ao)]*
Log[Ri^2 + Ro^2 + 2*L*Ri*ai + 2*L*Ro*ao + L^2*(ai^2 + ao^2)] +
Ri*ao*Log[Ri + Ro + x*(ai + ao)]*Log[Ri^2 + Ro^2 + 2*L*Ri*ai +
2*L*Ro*ao + L^2*(ai^2 + ao^2)] + Ro*ao*Log[Ri + Ro + x*(ai + ao)]*
Log[Ri^2 + Ro^2 + 2*L*Ri*ai + 2*L*Ro*ao + L^2*(ai^2 + ao^2)] +
x*ao^2*Log[Ri + Ro + x*(ai + ao)]*Log[Ri^2 + Ro^2 + 2*L*Ri*ai +
2*L*Ro*ao + L^2*(ai^2 + ao^2)] + Ri*ai*Log[Ri - Ro]*
Log[Ri^2 + Ro^2 + 2*Ri*x*ai + 2*Ro*x*ao + x^2*(ai^2 + ao^2)] +
Ro*ai*Log[Ri - Ro]*
Log[Ri^2 + Ro^2 + 2*Ri*x*ai + 2*Ro*x*ao + x^2*(ai^2 + ao^2)] +
x*ai^2*Log[Ri - Ro]*
Log[Ri^2 + Ro^2 + 2*Ri*x*ai + 2*Ro*x*ao + x^2*(ai^2 + ao^2)] -
Ri*ao*Log[Ri - Ro]*
Log[Ri^2 + Ro^2 + 2*Ri*x*ai + 2*Ro*x*ao + x^2*(ai^2 + ao^2)] -
Ro*ao*Log[Ri - Ro]*
Log[Ri^2 + Ro^2 + 2*Ri*x*ai + 2*Ro*x*ao + x^2*(ai^2 + ao^2)] -
x*ao^2*Log[Ri - Ro]*
Log[Ri^2 + Ro^2 + 2*Ri*x*ai + 2*Ro*x*ao + x^2*(ai^2 + ao^2)] -
Ri*ai*Log[Ri + Ro]*
Log[Ri^2 + Ro^2 + 2*Ri*x*ai + 2*Ro*x*ao + x^2*(ai^2 + ao^2)] +
Ro*ai*Log[Ri + Ro]*
Log[Ri^2 + Ro^2 + 2*Ri*x*ai + 2*Ro*x*ao + x^2*(ai^2 + ao^2)] -
x*ai^2*Log[Ri + Ro]*
Log[Ri^2 + Ro^2 + 2*Ri*x*ai + 2*Ro*x*ao + x^2*(ai^2 + ao^2)] -
Ri*ao*Log[Ri + Ro]*
Log[Ri^2 + Ro^2 + 2*Ri*x*ai + 2*Ro*x*ao + x^2*(ai^2 + ao^2)] +
Ro*ao*Log[Ri + Ro]*
Log[Ri^2 + Ro^2 + 2*Ri*x*ai + 2*Ro*x*ao + x^2*(ai^2 + ao^2)] +
x*ao^2*Log[Ri + Ro]*
Log[Ri^2 + Ro^2 + 2*Ri*x*ai + 2*Ro*x*ao + x^2*(ai^2 + ao^2)] -
Ro*ai*Log[Ri^2 + Ro^2]*
Log[Ri^2 + Ro^2 + 2*Ri*x*ai + 2*Ro*x*ao + x^2*(ai^2 + ao^2)] +
Ri*ao*Log[Ri^2 + Ro^2]*
Log[Ri^2 + Ro^2 + 2*Ri*x*ai + 2*Ro*x*ao + x^2*(ai^2 + ao^2)] -
Ri*ai*Log[Ri - Ro + L*ai - L*ao]*
Log[Ri^2 + Ro^2 + 2*Ri*x*ai + 2*Ro*x*ao + x^2*(ai^2 + ao^2)] -
Ro*ai*Log[Ri - Ro + L*ai - L*ao]*
Log[Ri^2 + Ro^2 + 2*Ri*x*ai + 2*Ro*x*ao + x^2*(ai^2 + ao^2)] -
x*ai^2*Log[Ri - Ro + L*ai - L*ao]*
Log[Ri^2 + Ro^2 + 2*Ri*x*ai + 2*Ro*x*ao + x^2*(ai^2 + ao^2)] +
Ri*ao*Log[Ri - Ro + L*ai - L*ao]*
Log[Ri^2 + Ro^2 + 2*Ri*x*ai + 2*Ro*x*ao + x^2*(ai^2 + ao^2)] +
Ro*ao*Log[Ri - Ro + L*ai - L*ao]*
Log[Ri^2 + Ro^2 + 2*Ri*x*ai + 2*Ro*x*ao + x^2*(ai^2 + ao^2)] +
x*ao^2*Log[Ri - Ro + L*ai - L*ao]*
Log[Ri^2 + Ro^2 + 2*Ri*x*ai + 2*Ro*x*ao + x^2*(ai^2 + ao^2)] +
Ri*ai*Log[Ri + Ro + L*(ai + ao)]*
Log[Ri^2 + Ro^2 + 2*Ri*x*ai + 2*Ro*x*ao + x^2*(ai^2 + ao^2)] -
Ro*ai*Log[Ri + Ro + L*(ai + ao)]*
Log[Ri^2 + Ro^2 + 2*Ri*x*ai + 2*Ro*x*ao + x^2*(ai^2 + ao^2)] +
x*ai^2*Log[Ri + Ro + L*(ai + ao)]*
Log[Ri^2 + Ro^2 + 2*Ri*x*ai + 2*Ro*x*ao + x^2*(ai^2 + ao^2)] +

Ri*ao*Log[Ri + Ro + L*(ai + ao)]*
Log[Ri^2 + Ro^2 + 2*Ri*x*ai + 2*Ro*x*ao + x^2*(ai^2 + ao^2)] -
Ro*ao*Log[Ri + Ro + L*(ai + ao)]*
Log[Ri^2 + Ro^2 + 2*Ri*x*ai + 2*Ro*x*ao + x^2*(ai^2 + ao^2)] -
x*ao^2*Log[Ri + Ro + L*(ai + ao)]*
Log[Ri^2 + Ro^2 + 2*Ri*x*ai + 2*Ro*x*ao + x^2*(ai^2 + ao^2)] + Ro*ai*
Log[Ri^2 + Ro^2 + 2*L*Ri*ai + 2*L*Ro*ao + L^2*(ai^2 + ao^2)]*
Log[Ri^2 + Ro^2 + 2*Ri*x*ai + 2*Ro*x*ao + x^2*(ai^2 + ao^2)] - Ri*ao*
Log[Ri^2 + Ro^2 + 2*L*Ri*ai + 2*L*Ro*ao + L^2*(ai^2 + ao^2)]*
Log[Ri^2 + Ro^2 + 2*Ri*x*ai + 2*Ro*x*ao + x^2*(ai^2 + ao^2)] +
2*ArcCot[(Ro*ai - Ri*ao)/(Ri*ai + Ro*ao + L*(ai^2 + ao^2))]*
(2*(Ro*ai - Ri*ao)*ArcCot[(Ro*ai - Ri*ao)/(Ri*ai + Ro*ao +
x*(ai^2 + ao^2))] + (ai - ao)*(Ri - Ro + x*ai - x*ao)*Log[Ri - Ro] +
Ri*ai*Log[Ri + Ro] + Ro*ai*Log[Ri + Ro] +
x*ai^2*Log[Ri + Ro] + Ri*ao*Log[Ri + Ro] + Ro*ao*Log[Ri + Ro] +
2*x*ai*ao*Log[Ri + Ro] + x*ao^2*Log[Ri + Ro] -
Ri*ai*Log[Ri^2 + Ro^2] - x*ai^2*Log[Ri^2 + Ro^2] -
Ro*ao*Log[Ri^2 + Ro^2] - x*ao^2*Log[Ri^2 + Ro^2] -
Ri*ai*Log[Ri - Ro + x*ai - x*ao] + Ro*ai*Log[Ri - Ro + x*ai - x*ao] -
x*ai^2*Log[Ri - Ro + x*ai - x*ao] + Ri*ao*Log[Ri - Ro + x*ai - x*ao] -
Ro*ao*Log[Ri - Ro + x*ai - x*ao] + 2*x*ai*ao*
Log[Ri - Ro + x*ai - x*ao] - x*ao^2*Log[Ri - Ro + x*ai - x*ao] -
Ri*ai*Log[Ri + Ro + x*(ai + ao)] - Ro*ai*Log[Ri + Ro + x*(ai + ao)] -
x*ai^2*Log[Ri + Ro + x*(ai + ao)] - Ri*ao*Log[Ri + Ro + x*(ai + ao)] -
Ro*ao*Log[Ri + Ro + x*(ai + ao)] - 2*x*ai*ao*
Log[Ri + Ro + x*(ai + ao)] - x*ao^2*Log[Ri + Ro + x*(ai + ao)] +
Ri*ai*Log[Ri^2 + Ro^2 + 2*Ri*x*ai + 2*Ro*x*ao +
x^2*(ai^2 + ao^2)] + x*ai^2*
Log[Ri^2 + Ro^2 + 2*Ri*x*ai + 2*Ro*x*ao + x^2*(ai^2 + ao^2)] + Ro*ao*
Log[Ri^2 + Ro^2 + 2*Ri*x*ai + 2*Ro*x*ao + x^2*(ai^2 + ao^2)] + x*ao^2*
Log[Ri^2 + Ro^2 + 2*Ri*x*ai + 2*Ro*x*ao +
x^2*(ai^2 + ao^2)]) - 2*ArcCot[(Ro*ai - Ri*ao)/(Ri*ai + Ro*ao)]*
(2*(Ro*ai - Ri*ao)*ArcCot[(Ro*ai - Ri*ao)/(Ri*ai +
Ro*ao + L*(ai^2 + ao^2))] + 2*(Ro*ai - Ri*ao)*
ArcCot[(Ro*ai - Ri*ao)/(Ri*ai + Ro*ao + x*(ai^2 + ao^2))] +
Ri*ai*Log[Ri - Ro + L*ai - L*ao] - Ro*ai*Log[Ri - Ro + L*ai - L*ao] +
x*ai^2*Log[Ri - Ro + L*ai - L*ao] - Ri*ao*Log[Ri - Ro + L*ai - L*ao] +
Ro*ao*Log[Ri - Ro + L*ai - L*ao] - 2*x*ai*ao*Log[Ri - Ro + L*ai - L*ao] +
x*ao^2*Log[Ri - Ro + L*ai - L*ao] - Ri*ai*Log[Ri - Ro + x*ai - x*ao] +
Ro*ai*Log[Ri - Ro + x*ai - x*ao] - x*ai^2*Log[Ri - Ro + x*ai - x*ao] +
Ri*ao*Log[Ri - Ro + x*ai - x*ao] - Ro*ao*Log[Ri - Ro + x*ai - x*ao] +
2*x*ai*ao*Log[Ri - Ro + x*ai - x*ao] - x*ao^2*Log[Ri - Ro + x*ai - x*ao] +
Ri*ai*Log[Ri + Ro + L*(ai + ao)] + Ro*ai*Log[Ri + Ro + L*(ai + ao)] +
x*ai^2*Log[Ri + Ro + L*(ai + ao)] + Ri*ao*Log[Ri + Ro + L*(ai + ao)] +
Ro*ao*Log[Ri + Ro + L*(ai + ao)] + 2*x*ai*ao*
Log[Ri + Ro + L*(ai + ao)] + x*ao^2*Log[Ri + Ro + L*(ai + ao)] -
Ri*ai*Log[Ri + Ro + x*(ai + ao)] - Ro*ai*Log[Ri + Ro + x*(ai + ao)] -
x*ai^2*Log[Ri + Ro + x*(ai + ao)] - Ri*ao*Log[Ri + Ro + x*(ai + ao)] -
Ro*ao*Log[Ri + Ro + x*(ai + ao)] - 2*x*ai*ao*
Log[Ri + Ro + x*(ai + ao)] - x*ao^2*Log[Ri + Ro + x*(ai + ao)] -
Ri*ai*Log[Ri^2 + Ro^2 + 2*L*Ri*ai + 2*L*Ro*ao +
L^2*(ai^2 + ao^2)] - x*ai^2*Log[Ri^2 + Ro^2 + 2*L*Ri*ai + 2*L*Ro*ao +
L^2*(ai^2 + ao^2)] - Ro*ao*Log[Ri^2 + Ro^2 + 2*L*Ri*ai + 2*L*Ro*ao +
L^2*(ai^2 + ao^2)] - x*ao^2*Log[Ri^2 + Ro^2 + 2*L*Ri*ai + 2*L*Ro*ao +
L^2*(ai^2 + ao^2)] + Ri*ai*Log[Ri^2 + Ro^2 + 2*Ri*x*ai + 2*Ro*x*ao +

```
x^2*(ai^2 + ao^2)] + x*ai^2*Log[Ri^2 + Ro^2 + 2*Ri*x*ai + 2*Ro*x*ao +
x^2*(ai^2 + ao^2)] + Ro*ao*Log[Ri^2 + Ro^2 + 2*Ri*x*ai + 2*Ro*x*ao +
x^2*(ai^2 + ao^2)] + x*ao^2*Log[Ri^2 + Ro^2 + 2*Ri*x*ai + 2*Ro*x*ao +
x^2*(ai^2 + ao^2)])))/(E*Pi*(Ro*ai - Ri*ao)^2*(2*(ai^2 - ao^2)*
ArcCot[(Ro*ai - Ri*ao)/(Ri*ai + Ro*ao)] - 2*(ai^2 - ao^2)*
ArcCot[(Ro*ai - Ri*ao)/(Ri*ai + Ro*ao + L*(ai^2 + ao^2))] - ai^2*
Log[Ri - Ro] + 2*ai*ao*Log[Ri - Ro] - ao^2*Log[Ri - Ro] +
ai^2*Log[Ri + Ro] + 2*ai*ao*Log[Ri + Ro] + ao^2*Log[Ri + Ro] -
2*ai*ao*Log[Ri^2 + Ro^2] + ai^2*Log[Ri - Ro + L*ai - L*ao] - 2*ai*ao*
Log[Ri - Ro + L*ai - L*ao] + ao^2*Log[Ri - Ro + L*ai - L*ao] - ai^2*
Log[Ri + Ro + L*(ai + ao)] - 2*ai*ao*Log[Ri + Ro + L*(ai + ao)] -
ao^2*Log[Ri + Ro + L*(ai + ao)] + 2*ai*ao*
Log[Ri^2 + Ro^2 + 2*L*Ri*ai + 2*L*Ro*ao + L^2*(ai^2 + ao^2)]))
```

(A.1)

Explicit solution to the system of equations formed from Equations (3.20)–(3.25) given in a format easily copied and entered into and modified for a computer function:

```
y = (1/(E*Pi*(Ro*ai - Ri*ao)^3))*(P*(-2*(Ri^2 + L*Ri*ai - Ro*(Ro + L*ao))*
ArcCot[(Ro*ai - Ri*ao)/(Ri*ai + Ro*ao)] + 2*(Ri^2 + L*Ri*ai - Ro*(Ro + L*ao))*
ArcCot[(Ro*ai - Ri*ao)/(Ri*ai + Ro*ao + x*(ai^2 + ao^2))] + 2*x*(Ri*ai - Ro*ao + L*(ai^2 - ao^2))*
ArcCot[(Ro*ai - Ri*ao)/(Ri*ai + Ro*ao + x*(ai^2 + ao^2))] + (Ri - Ro)*(Ri - Ro + L*(ai - ao))*
Log[Ri - Ro] - Ri^2*Log[Ri + Ro] - 2*Ri*Ro*Log[Ri + Ro] - Ro^2*Log[Ri + Ro] - L*Ri*ai*Log[Ri + Ro] -
L*Ro*ai*Log[Ri + Ro] - L*Ri*ao*Log[Ri + Ro] - L*Ro*ao*Log[Ri + Ro] + 2*Ri*Ro*Log[Ri^2 + Ro^2] +
L*Ro*ai*Log[Ri^2 + Ro^2] + L*Ri*ao*Log[Ri^2 + Ro^2] - x*(2*(Ri*ai + L*ai^2 - Ro*ao - L*ao^2)*
ArcCot[(Ro*ai - Ri*ao)/(Ri*ai + Ro*ao)] - (ai - ao)*(Ri - Ro + L*ai - L*ao)*Log[Ri - Ro] + Ri*ai*
Log[Ri + Ro] + Ro*ai*Log[Ri + Ro] + L*ai^2*Log[Ri + Ro] + Ri*ao*Log[Ri + Ro] + Ro*ao*
Log[Ri + Ro] + 2*L*ai*ao*Log[Ri + Ro] + L*ao^2*Log[Ri + Ro] - Ro*ai*
Log[Ri^2 + Ro^2] - Ri*ao*Log[Ri^2 + Ro^2] - 2*L*ai*ao*
Log[Ri^2 + Ro^2]) - (Ri - Ro)*(Ri - Ro + L*(ai - ao))*
Log[Ri - Ro + x*ai - x*ao] - x*(Ri - Ro + L*(ai - ao))*(ai - ao)*
Log[Ri - Ro + x*ai - x*ao] + (Ri + Ro)*(Ri + Ro + L*(ai + ao))*
Log[Ri + Ro + x*(ai + ao)] + x*(ai + ao)*(Ri + Ro + L*(ai + ao))*
Log[Ri + Ro + x*(ai + ao)] - (2*Ri*Ro + L*Ro*ai + L*Ri*ao)*
Log[Ri^2 + Ro^2 + 2*Ri*x*ai + 2*Ro*x*ao + x^2*(ai^2 + ao^2)] - x*(Ro*ai + (Ri + 2*L*ai)*ao)*
Log[Ri^2 + Ro^2 + 2*Ri*x*ai + 2*Ro*x*ao + x^2*(ai^2 + ao^2)]))
```

(A.2)

Explicit solution to the system of equations formed from Equations (3.20), (3.21), (3.26)–(3.29) given in a format easily copied and entered into and modified for a computer function:

```
y = (1/(E*Pi*(Ro*ai - Ri*ao)^3))*(M*(2*(Ri*ai + x*ai^2 - Ro*ao - x*ao^2)*
ArcCot[(Ro*ai - Ri*ao)/(Ri*ai + Ro*ao)] - 2*(Ri*ai + x*ai^2 - Ro*ao - x*ao^2)*
ArcCot[(Ro*ai - Ri*ao)/(Ri*ai + Ro*ao + x*(ai^2 + ao^2))] - Ri*ai*Log[Ri - Ro] + Ro*ai*Log[Ri - Ro] -
x*ai^2*Log[Ri - Ro] + Ri*ao*Log[Ri - Ro] - Ro*ao*Log[Ri - Ro] + 2*x*ai*ao*Log[Ri - Ro] -
x*ao^2*Log[Ri - Ro] + Ri*ai*Log[Ri + Ro] + Ro*ai*Log[Ri + Ro] +
x*ai^2*Log[Ri + Ro] + Ri*ao*Log[Ri + Ro] + Ro*ao*Log[Ri + Ro] + 2*x*ai*ao*Log[Ri + Ro] +
x*ao^2*Log[Ri + Ro] - Ro*ai*Log[Ri^2 + Ro^2] - Ri*ao*Log[Ri^2 + Ro^2] - 2*x*ai*ao*
Log[Ri^2 + Ro^2] + Ri*ai*Log[Ri - Ro + x*ai - x*ao] - Ro*ai*Log[Ri - Ro + x*ai - x*ao] +
x*ai^2*Log[Ri - Ro + x*ai - x*ao] - Ri*ao*Log[Ri - Ro + x*ai - x*ao] +
```

```
Ro*ao*Log[Ri - Ro + x*ai - x*ao] - 2*x*ai*ao*Log[Ri - Ro + x*ai - x*ao] + x*ao^2*
Log[Ri - Ro + x*ai - x*ao] - Ri*ai*Log[Ri + Ro + x*(ai + ao)] -
Ro*ai*Log[Ri + Ro + x*(ai + ao)] - x*ai^2*Log[Ri + Ro + x*(ai + ao)] -
Ri*ao*Log[Ri + Ro + x*(ai + ao)] -
Ro*ao*Log[Ri + Ro + x*(ai + ao)] - 2*x*ai*ao*
Log[Ri + Ro + x*(ai + ao)] - x*ao^2*Log[Ri + Ro + x*(ai + ao)] + Ro*ai*
Log[Ri^2 + Ro^2 + 2*Ri*x*ai + 2*Ro*x*ao + x^2*(ai^2 + ao^2)] + Ri*ao*
Log[Ri^2 + Ro^2 + 2*Ri*x*ai + 2*Ro*x*ao + x^2*(ai^2 + ao^2)] + 2*x*ai*ao*
Log[Ri^2 + Ro^2 + 2*Ri*x*ai + 2*Ro*x*ao + x^2*(ai^2 + ao^2)]))
```

(A.3)

7 REFERENCES

[1] Savia, M., and Koivo, H. N., 2009, "Contact Micromanipulation-Survey of Strategies," IEEE/ASME Transactions on Mechatronics, **14**(4) .

[2] Siciliano, B., and Khatib, O., Eds., 2008, "Springer handbook of robotics," Springer, New York, NY.

[3] Dong, L., Arai, F., and Fukuda, T., 2001, "3D nanorobotic manipulations of multi-walled carbon nanotubes," IEEE International Conference on Robotics and Automation, **1**.

[4] Dong, L., Arai, F., and Fukuda, T., 2002, "3D nanoassembly of carbon nanotubes through nanorobotic manipulations," 2002 IEEE International Conference on Robotics and Automation, May 11 - 15, 2002, **2**.

[5] Fukuda, T., Arai, F., and Dong, L., 2003, "Assembly of Nanodevices with Carbon Nanotubes through Nanorobotic Manipulations," Proceedings of the IEEE, **91**(11).

[6] Xie, H., and Regnier, S., 2009, "Three-Dimensional Automated Micromanipulation using a Nanotip Gripper with Multi-Feedback," Journal of Micromechanics and Microengineering, **19**(7).

[7] Wason, J., Gressick, W., Wen, J. T., 2007, "Multi-probe micro-assembly," 3rd IEEE International Conference on Automation Science and Engineering, IEEE CASE 2007, September 22 - 25, 2007.

[8] Murthy, R., Das, A., and Popa, D., 2006, "Multiscale robotics framework for MEMS assembly," 9th International Conference on Control, Automation, Robotics and Vision, 2006, ICARCV '06, December 5 - 8, 2006.

[9] Dechev, N., Ren, L., Liu, W., 2006, "Development of a 6 degree of freedom robotic micromanipulator for use in 3D MEMS microassembly," 2006 IEEE International Conference on Robotics and Automation, ICRA 2006, May 15 - 19, 2006.

[10] "MM3A-EM Micromanipulator," Kleindiek Nanotechnik, from http://www.nanotechnik.com/fileadmin/public/brochures/mm3a-em.pdf, (November 27, 2012).

[11] Feynman, R. P., 1992, "There's Plenty of Room at the Bottom," Journal of Microelectromechanical Systems, **1**(1).

[12] Park, F. C., and Brockett, R. W., 1994, "Kinematic Dexterity of Robotic Mechanisms," International Journal of Robotics Research, **13**(1).

[13] Arai, F., Ando, D., Fukuda, T., 1995, "Micro manipulation based on micro physics-strategy based on attractive force reduction and stress measurement," Human Robot Interaction and Cooperative Robots, **2**.

[14] Spearing, S. M., 2000, "Materials Issues in Microelectromechanical Systems (MEMS)," Acta Materialia, **48**(1).

[15] Zhou, Y., and Nelson, B. J., 1998, "Adhesion force modeling and measurement for micromanipulation," Proceedings of SPIE, **3519**.

[16] Arai, F., Andou, D., Nonoda, Y., 1998, "Integrated Microendeffector for Micromanipulation," IEEE/ASME Transactions on Mechatronics, **3**(1).

[17] Feddema, J. T., Xavier, P., and Brown, R., 1999, "Micro-assembly planning with van der Waals force," Proceedings of the 1999 IEEE International Symposium on Assembly and Task Planning (ISATP'99).

[18] Haliyo, S., Dionnet, F., and Regnier, S., 2003, "Advanced micro-manipulation applications," 2003 IEEE/RSJ International Conference on Intelligent Robots and Systems, **2**.

[19] Rabenorosoa, K., Clevy, C., Lutz, P., 2009, "Measurement of Pull-Off Force for Planar Contact at the Microscale," Micro and Nano Letters, **4**(3).

[20] Menciassi, A., Eisinberg, A., Izzo, I., 2004, "From "Macro" to "Micro" Manipulation: Models and Experiments," IEEE/ASME Transactions on Mechatronics, **9**(2).

[21] Yang, Q., and Jagannathan, S., 2008, "A Suite of Robust Controllers for the Manipulation of Microscale Objects," IEEE Transactions on Systems, Man, and Cybernetics, Part B: Cybernetics, **38**(1).

[22] Haliyo, D. S., Rollot, Y., and Regnier, S., 2002, "Manipulation of micro-objects using adhesion forces and dynamical effects," Proceedings 2002 IEEE International Conference on Robotics and Automation, **2**.

[23] Rollot, Y., Regnier, S., and Guinot, J., 1999, "Simulation of Micro-Manipulations: Adhesion Forces and Specific Dynamic Models," International Journal of Adhesion and Adhesives, **19**(1).

[24] Hashimoto, H., and Sitti, M., 1999, "Challenge to micro/nanomanipulation using atomic force microscope," International Symposium on Micromechatronics and Human Science (MHS'99) 'Towards the New Century', November 23 - 26, 1999.

[25] Yang, F., and Xiaobo, T., 2006, "A dynamic JKR model with application to vibrational release in micromanipulation," 2006 IEEE/RSJ International Conference on Intelligent Robots and Systems, IROS, October 9 - 15, 2006.

[26] Fok, L. M., Liu, Y. H., and Li, W. J., 2008, "Assembly of nano optics by an integrated probe-based system," Proceedings of the 7th IEEE International Conference on Nanotechnology.

[27] Vergeles, M., Maritan, A., Koplik, J., 1997, "Adhesion of Solids," Physical Review E, **56**(3).

[28] Saito, S., Miyazaki, H. T., Sato, T., 2002, "Kinematics of Mechanical and Adhesional Micromanipulation Under a Scanning Electron Microscope," Journal of Applied Physics, **92**(9).

[29] Rollot, Y., Regnier, S., and Guinot, J. C., 1998, "Micro-Robotics: A Dynamical Model of Micromanipulation by Adhesion," Proceedings of the 12th CISM-IFToMM symposium.

[30] Sitti, M., and Hashimoto, H., 2003, "Teleoperated Touch Feedback from the Surfaces at the Nanoscale: Modeling and Experiments," IEEE/ASME Transactions on Mechatronics, **8**(2).

[31] Sitti, M., and Hashimoto, H., 2000, "Controlled Pushing of Nanoparticles: Modeling and Experiments," IEEE/ASME Transactions on Mechatronics, **5**(2).

[32] Johnson, K. L., Kendall, K., and Roberts, A. D., 1971, "Surface Energy and the Contact of Elastic Solids," Proceedings of the Royal Society of London, Series A (Mathematical and Physical Sciences), **324**(1558).

[33] Johnson, K. L., and Greenwood, J. A., 1997, "Adhesion Map for the Contact of Elastic Spheres," Journal of Colloid and Interface Science, **192**(2).

[34] Yao, H., Ciavarella, M., and Gao, H., 2007, "Adhesion Maps of Spheres Corrected for Strength Limit," Journal of Colloid and Interface Science, **315**(2).

[35] Barquins, M., 1988, "Adherence and Rolling Kinetics of a Rigid Cylinder in Contact with a Natural Rubber Surface," The Journal of Adhesion, **26**(1).

[36] Majumdar, B. S., Ye, B., Lavan, D. A., 2005, "Contact and adhesion of curved rough surfaces with application to mems," 2005 World Tribology Congress III, September 12 - 16, 2005.

[37] Zhao, Y. -., Wang, L. S., and Yu, T. X., 2003, "Mechanics of Adhesion in MEMS - A Review," Journal of Adhesion Science and Technology, **17**(4).

[38] Gui, C., Elwenspoek, M., Tas, N., 1999, "The Effect of Surface Roughness on Direct Wafer Bonding," Journal of Applied Physics, **85**(10).

[39] Delrio, F. W., De Boer, M. P., Knapp, J. A., 2005, "The Role of Van Der Waals Forces in Adhesion of Micromachined Surfaces," Nature Materials, **4**(8).

[40] Tang, T., Jagota, A., and Hui, C., 2005, "Adhesion between Single-Walled Carbon Nanotubes," Journal of Applied Physics, **97**(7).

[41] Komvopoulos, K., 2003, "Adhesion and Friction Forces in Microelectromechanical Systems: Mechanisms, Measurement, Surface Modification Techniques, and Adhesion Theory," Journal of Adhesion Science and Technology, **17**(4).

[42] Tambe, N. S., and Bhushan, B., 2004, "Scale Dependence of micro/nano-Friction and Adhesion of MEMS/NEMS Materials, Coatings and Lubricants," Nanotechnology, **15**(11).

[43] Tas, N. R., Gui, C., and Elwenspoek, M., 2003, "Static Friction in Elastic Adhesion Contacts in MEMS," Journal of Adhesion Science and Technology, **17**(4).

[44] Timpe, S. J., and Komvopoulos, K., 2006, "The Effect of Adhesion on the Static Friction Properties of Sidewall Contact Interfaces of Microelectromechanical Devices," Journal of Microelectromechanical Systems, **15**(6).

[45] Wu, J., Wang, S., and Miao, J., 2009, "Friction Characteristics of the Curved Sidewall Surfaces of a Rotary MEMS Device in Oscillating Motion," Journal of Micromechanics and Microengineering, **19**(6).

[46] Wu, J., Wang, S., and Miao, J., 2008, "A MEMS Device for Studying the Friction Behavior of Micromachined Sidewall Surfaces," Journal of Microelectromechanical Systems, **17**(4).

[47] Falvo, M. R., Taylor II, R. M., Helser, A., 1999, "Nanometre-Scale Rolling and Sliding of Carbon Nanotubes," Nature, **397**(6716).

[48] Lu, H., Goldman, J., Ding, F., 2008, "Friction and Adhesion Properties of Vertically Aligned Multi-Walled Carbon Nanotube Arrays and Fluoro-Nanodiamond Films," Carbon, **46**(10).

[49] Suekane, O., Nagataki, A., Mori, H., 2008, "Static Friction Force of Carbon Nanotube Surfaces," Applied Physics Express, **1**(6).

[50] Landolsi, F., Ghorbel, F. H., Lou, J., 2009, "Nanoscale Friction Dynamic Modeling," Journal of Dynamic Systems, Measurement and Control, **131**(6).

[51] Bhushan, B., Galasso, B., Bignardi, C., 2008, "Adhesion, Friction and Wear on the Nanoscale of MWNT Tips and SWNT and MWNT Arrays," Nanotechnology, **19**(12).

[52] Szoszkiewicz, R., Bhushan, B., Huey, B. D., 2006, "Adhesion Hysteresis and Friction at Nanometer and Micrometer Lengths," Journal of Applied Physics, **99**(1).

[53] Bhushan B., Ling X., Jungen A., 2008, "Adhesion and Friction of a Multiwalled Carbon Nanotube Sliding Against Single-Walled Carbon Nanotube," Physical Review B - Condensed Matter and Materials Physics, **77**(16).

[54] Junno, T., Deppert, K., Montelius, L., 1995, "Controlled Manipulation of Nanoparticles with an Atomic Force Microscope," Applied Physics Letters, **66**(26).

[55] Baur, C., Bugacov, A., Koel, B. E., 1998, "Nanoparticle Manipulation by Mechanical Pushing: Underlying Phenomena and Real-Time Monitoring," Nanotechnology, **9**(4).

[56] Schaefer, D. M., Reifenberger, R., Patil, A., 1995, "Fabrication of Two-Dimensional Arrays of Nanometer-Size Clusters with the Atomic Force Microscope," Applied Physics Letters, **66**(8).

[57] Decossas, S., Patrone, L., Bonnot, A. M., 2003, "Nanomanipulation by Atomic Force Microscopy of Carbon Nanotubes on a Nanostructured Surface," Surface Science, **543**(1-3).

[58] Thelander, C., and Samuelson, L., 2002, "AFM Manipulation of Carbon Nanotubes: Realization of Ultra-Fine Nanoelectrodes," Nanotechnology, **13**(1).

[59] Nakajima, M., Arai, F., Dong, L., 2004, "A hybrid nanorobotic manipulation system integrated with nanorobotic manipulators inside scanning and transmission electron microscopes," 2004 4th IEEE Conference on Nanotechnology, August 16 - 19, 2004.

[60] Culpepper, M. L., and Anderson, G., 2004, "Design of a Low-Cost Nano-Manipulator which Utilizes a Monolithic, Spatial Compliant Mechanism," Precision Engineering, **28**(4).

[61] Chen, S., and Culpepper, M. L., 2006, "Design of a Six-Axis Micro-Scale Nanopositioner-HexFlex," Precision Engineering, **30**(3).

[62] Portman, V. T., Sandler, B., and Zahavi, E., 2001, "Rigid 6-DOF Parallel Platform for Precision 3-D Micromanipulation," International Journal of Machine Tools and Manufacture, **41**(9).

[63] Yi, B., Chung, G. B., Na, H. Y., 2003, "Design and Experiment of a 3-DOF Parallel Micromechanism Utilizing Flexure Hinges," IEEE Transactions on Robotics and Automation, **19**(4).

[64] Alici, G., Shirinzadeh, B., 2003, "Description and Kinematic Analysis of a Planar Micromanipulation System Based on Flexure Joints," Proceeding of the IEEE/ASME ICAIM, **2**.

[65] Chang, S. H., Tseng, C. K., and Chien, H. C., 1999, "Ultra-Precision XYZ Piezo-Micropositioner Part I: Design and Analysis," IEEE Transactions on Ultrasonics, Ferroelectrics, and Frequency Control, **46**(4).

[66] Chang, S. H., Tseng, C. K., and Chien, H. C., 1999, "Ultra-Precision XYZ Piezo-Micropositioner Part II: Experiment and Performance," IEEE Transactions on Ultrasonics, Ferroelectrics, and Frequency Control, **46**(4).

[67] Haddab, Y., Chaillet, N., and Bourjault, A., 2000, "A microgripper using smart piezoelectric actuators," IEEE/RSJ International Conference on Intelligent Robots and Systems, October 31 - November 5, 2000, **1**.

[68] Kohl, M., Krevet, B., and Just, E., 2002, "SMA microgripper system," Sensors and Actuators A, **97-98**.

[69] Thornell, G., Bexell, M., Schweitz, J., 1995, "Design and fabrication of a gripping tool for micromanipulation," Proceedings of the 8th International Conference on Solid-State Sensors and Actuators and Eurosensors IX, June 25 - 29, 1995, **2**.

[70] Carrozza, M. C., Menciassi, A., Tiezzi, G., 1998, "Development of a LIGA-Microfabricated Gripper for Micromanipulation Tasks," Journal of Micromechanics and Microengineering, **8**(2).

[71] Kim, P., and Lieber, C. M., 1999, "Nanotube Nanotweezers," Science, **286**(5447).

[72] Mlhave, K., Wich, T., Kortschack, A., 2006, "Pick-and-Place Nanomanipulation using Microfabricated Grippers," Nanotechnology, **17**(10).

[73] Volland, B. E., Heerlein, H., and Rangelow, I. W., 2002, "Electrostatically driven microgripper," Micro and Nano Engineering, September 16 - 19, 2001, **61-62**.

[74] Nah, S. K., and Zhong, Z. W., 2007, "A Microgripper using Piezoelectric Actuation for Micro-Object Manipulation," Sensors and Actuators, A: Physical, **133**(1).

[75] Krishnan, S., and Saggere, L., 2008, "Design and Development of a Novel Micro-clasp Gripper for Micromanipulation of Complex-shaped Objects," Sensors and Actuators A, **176**, April, 2012.

[76] Tanikawa, T., and Arai, T., 1999, "Development of a Micro-Manipulation System having a Two-Fingered Micro-Hand," IEEE Transactions on Robotics and Automation, **15**(1).

[77] Inoue, T., Hamasaki, Y., Shimoyama, I., 1996, "Micromanipulation using a microcoil array," Proceedings of the IEEE ICRA, April 22 - 28, 1996, **3**.

[78] Nakamura, T., Kogure, Y., and Shimamura, K., 2000, "Micro operation hand and its application to microdrawing," ICRA 2000: IEEE International Conference on Robotics and Automation, April 24 - 28, **2**.

[79] Ferreira, A., Agnus, J., Chaillet, N., 2004, "A Smart Microrobot on Chip: Design, Identification, and Control," IEEE/ASME Transactions on Mechatronics, **9**(3).

[80] Shimada, E., Thompson, J. A., Yan, J., 2000, "Prototyping Millirobots using Dextrous Microassembly and Folding," Proceedings of the ASME IMECE/DSCD, November 5-10, 2000.

[81] Krishnan, S., and Saggere, L., 2007, "A Multi-Fingered Micromechanism for Coordinated micro/nano Manipulation," Journal of Micromechanics and Microengineering, **17**(3).

[82] Sandeep Krishnan, 2009, "Development of strategies and advanced tools for complex micromanipulation," Ph.D. Dissertation, Department of Mechanical and Industrial Engineering, University of Illinois at Chicago, Chicago, IL.

[83] Krishnan, S., Pelzmann, C., and Saggeret, L., 2010, "Design and Development of a Chipscale Multifingered Micromanipulator System for Coordinated Microassembly," Proceedings of the ASME 2009 ASME IDETC and CIE Conference: 3rd International Conference on Micro-& Nanosystems, August 30 - September 2, 2009, San Diego, CA, USA.

[84] Pelzmann, C., and Saggere, L., 2011, "Microassembly via Coordinated Manipulation of Objects using a Multifingered Micromanipulator," Proceedings of the ASME IMECE, November 11-17, 2011, Denver, CO, USA, (54976).

[85] Gorman, J. J., Kim, Y., Vladar, A. E., 2007, "Design of an on-Chip Microscale Nanoassembly System," International Journal of Nanomanufacturing, **1**(6).

[86] DiBiasio, C. M., Culpepper, M. L., Panas, R., 2008, "Comparison of Molecular Simulation and Pseudo-Rigid-Body Model Predictions for a Carbon Nanotube-Based Compliant Parallel-Guiding Mechanism," Journal of Mechanical Design, **130**(4).

[87] Howell, L. L., Dibiasio, C. M., Cullinan, M. A., 2010, "A Pseudo-Rigid-Body Model for Large Deflections of Fixed-Clamped Carbon Nanotubes," Journal of Mechanisms and Robotics, **2**(3).

[88] Cox, D. C., Forrest, R. D., Smith, P. R., 2005, "Study of the Current Stressing in Nanomanipulated Three-Dimensional Carbon Nanotube Structures," Applied Physics Letters, **87**(3).

[89] Madsen, D. N., Molhave, K., Mateiu, R., 2003, "Soldering of Nanotubes Onto Microelectrodes," Nano Letters, **3**(1).

[90] Postma, H. W. C., de Jonge, M., and Dekker, C., 2000, "Electrical Transport through Carbon Nanotube Junctions Created by Mechanical Manipulation," Physical Review B, **62**(16).

[91] Wang, M., Wang, J., Chen, Q., 2005, "Fabrication and Electrical and Mechanical Properties of Carbon Nanotube Interconnections," Advanced Functional Materials, **15**(11).

[92] Banhart, F., 2001, "The Formation of a Connection between Carbon Nanotubes in an Electron Beam," Nano Letters, **1**(6).

[93] Bussolotti, F., D'Ortenzi, L., Grossi, V., 2007, "In Situ Manipulation and Electrical Characterization of Multiwalled Carbon Nanotubes by using Nanomanipulators Under Scanning Electron Microscopy," Physical Review B (Condensed Matter and Materials Physics), **76**(12).

[94] Fukuda, T., Liu, P., and Kantola, K., 2007, "Nanoscale cutting, bending and welding in a nanoassembly," 2007 2nd IEEE International Conference on Nano/Micro Engineered and Molecular Systems, IEEE NEMS, January 16 - 19, 2007.

[95] Kis, A., Csanyi, G., Salvetat, J. -., 2004, "Reinforcement of Single-Walled Carbon Nanotube Bundles by Intertube Bridging," Nature Materials, **3**(3).

[96] Yu, M., Lourie, O., Dyer, M. J., 2000, "Strength and Breaking Mechanism of Multiwalled Carbon Nanotubes Under Tensile Load," Science, **287**(5453).

[97] Senga, R., Hirahara, K., and Nakayama, Y., 2010, "Attachment of Carbon Nanotubes to a Substrate by Electron-Beam-Induced Structural Change of Fullerene Molecules," Applied Physics Express, **3**(2).

[98] Kashiwase, Y., Ikeda, T., Oya, T., 2008, "Manipulation and Soldering of Carbon Nanotubes using Atomic Force Microscope," Applied Surface Science, **254**(23).

[99] Dong, L., Youkey, S., Bush, J., 2007, "Effects of Local Joule Heating on the Reduction of Contact Resistance between Carbon Nanotubes and Metal Electrodes," Journal of Applied Physics, **101**(2).

[100] Du, S., and Li, Y., 2007, "Micromanipulation based on AFM: probe tip selection," Proceedings of the 7th IEEE International Conference on Nanotechnology, August 2 - 5, 2007, Hong Kong.

[101] Driesen, W., Varidel, T., Regnier, S., 2005, "Micro Manipulation by Adhesion with Two Collaborating Mobile Micro Robots," Journal of Micromechanics and Microengineering, **15**(10).

[102] Wu, L., and Xie, H., 2008, "A Large Vertical Displacement Electrothermal Bimorph Microactuator with very Small Lateral Shift," Sensors and Actuators A, **145-146**.

[103] Chen, B. K., Zhang, Y., and Sun, Y., 2009, "Novel mems grippers capable of both grasping and active release of micro objects," TRANSDUCERS 2009 - 15th International Conference on Solid-State Sensors, Actuators and Microsystems, June 21 - 25, 2009.

[104] Chen, T., Chen, L., Sun, L., 2008, "Electrostatically driven microgripper integrated piezoresistive force sensor," DTIP of MEMS and MOEMS - Symposium on Design, Test, Integration and Packaging of MEMS/MOEMS, April 9 - 11, 2008.

[105] Eichhorn, V., Fatikow, S., Wortmann, T., 2009, "NanoLab: A nanorobotic system for automated pick-and-place handling and characterization of CNTs," 2009 IEEE International Conference on Robotics and Automation, ICRA '09, May 12 - 17, 2009.

[106] Ren, L., Wang, L., Mills, J. K., 2007, "3-D automatic microassembly by vision-based control," Proceedings of the 2007 IEEE/RSJ International Conference on Intelligent Robots and Systems, IROS 2007, October 29 - November 2, 2007.

[107] Wason, J. D., Wen, J. T., Choi, Y., 2010, "Vision guided multi-probe assembly of 3D microstructures," Proceedings of the 23rd IEEE/RSJ 2010 International Conference on Intelligent Robots and Systems, IROS 2010, October 18 - 22, 2010.

[108] Rabenorosoa, K., Clevy, C., Lutz, P., 2009, "Precise motion control of a piezolelectric microgripper for microspectrometer assembly," Proceedings of the ASME IDETC and CIE Conference, August 30 - September 2, 2009, **6**.

[109] Dresselhaus, J.A., and Dresselhaus, G., Eds., 2008, "Carbon Nanotubes: Advanced Topics in the Synthesis, Structure, Properties, and Applications," Springer, New York, NY.

[110] Wildoer, J. W. G., Venema, L. C., Rinzler, A. G., 1998, "Electronic Structure of Atomically Resolved Carbon Nanotubes," Nature, **391**(6662).

[111] Meyyappan, M., Delzeit, L., Cassell, A., 2003, "Carbon Nanotube Growth by PECVD: A Review," Plasma Sources Science and Technology, **12**(2).

[112] Smith, R. C., Carey, J. D., Cox, D. C., 2006, "In Situ Electrode Manipulation for Three Terminal Field Emission Characterization of Individual Carbon Nanotubes," Applied Physics Letters, **89**(6).

[113] Novoselov, K. S., Geim, A. K., Morozov, S. V., 2004, "Electric Field in Atomically Thin Carbon Films," Science, **306**(5696).

[114] Blake, P., Hill, E. W., Castro Neto, A. H., 2007, "Making Graphene Visible," Applied Physics Letters, **91**(6).

[115] Backes, C., Englert, J. M., Bernhard, N., 2010, "Optical Visualization of Carbon Nanotubes-a Unifying Linkage between Microscopic and Spectroscopic Characterization Techniques," Small, **6**(18).

[116] Wautelet, M., 2001, "Scaling Laws in the Macro-, Micro- and Nanoworlds," European Journal of Physics, **22**(6).

[117] Maugis, D., 1992, "Adhesion of Spheres: The JKR-DMT Transition using a Dugdale Model," Journal of Colloid and Interface Science, **150**(1).

[118] Derjaguin, B. V., Muller, V. M., and Toporov, Y. P., 1975, "Effect of Contact Deformations on the Adhesion of Particles," Journal of Colloid and Interface Science, **53**(2).

[119] Tabor, D., 1977, "Surface Forces and Surface Interactions," Journal of Colloid and Interface Science, **58**(1).

[120] Mason, M.T., and Salisbury, J.K., 1985, "Robot hands and the mechanics of manipulation," MIT Press, Cambridge, MA.

[121] Israelachvili, J.N., 1991, "Intermolecular and surface forces," Elsevier Inc., San Diego, CA.

[122] Taylor, J.R., 1997, "An Introduction to Error Analysis: The Study of Uncertainties in Physical Measurements, Second Edition," University Science Books, Sausalito, CA.

[123] Huang, Y., 2006, "Thickness of Graphene and Single-Wall Carbon Nanotubes," Physical Review B, **74**(24).

[124] Qian, D., Wagner, G. J., Liu, W. K., 2002, "Mechanics of Carbon Nanotubes," Applied Mechanics Reviews, **55**(6).

[125] Salvetat, J., Bonard, J., Thomson, N. B., 1999, "Mechanical Properties of Carbon Nanotubes," Applied Physics A: Materials Science and Processing, **69**(3).

[126] Salvetat, J., Kulik, A. J., Bonard, J., 1999, "Elastic Modulus of Ordered and Disordered Multiwalled Carbon Nanotubes," Advanced Materials, **11**(2).

[127] Wei, X., Liu, Y., Chen, Q., 2008, "The very Low Shear Modulus of Multi-Walled Carbon Nanotubes Determined Simultaneously with the Axial Young's Modulus Via in Situ Experiments," Advanced Functional Materials, **18**(10).

[128] Poncharal, P., Wang, Z. L., Ugarte, D., 1999, "Electrostatic Deflections and Electromechanical Resonances of Carbon Nanotubes," Science, **283**(5407).

[129] Treacy, M. M. J., Ebbesen, T. W., and Gibson, J. M., 1996, "Exceptionally High Young's Modulus Observed for Individual Carbon Nanotubes," Nature, **381**(6584).

[130] Wong, E. W., and Sheehan, P. E., 1997, "Nanobeam Mechanics: Elasticity, Strength, and Toughness of Nanorods and Nanotubes," Science, **277**(5334).

[131] Guhados, G., Wan, W., Sun, X., 2007, "Simultaneous Measurement of Young's and Shear Moduli of Multiwalled Carbon Nanotubes using Atomic Force Microscopy," Journal of Applied Physics, **101**(3).

[132] Demczyk, B. G., Wang, Y. M., Cumings, J., 2002, "Direct Mechanical Measurement of the Tensile Strength and Elastic Modulus of Multiwalled Carbon Nanotubes," Materials Science and Engineering A, **334**(1-2).

[133] Govindjee, S., and Sackman, J. L., 1999, "On the use of Continuum Mechanics to Estimate the Properties of Nanotubes," Solid State Communications, **110**(4).

[134] Harik, V. M., 2001, "Ranges of Applicability for the Continuum Beam Model in the Mechanics of Carbon Nanotubes and Nanorods," Solid State Communications, **120**(7-8).

[135] Guan, L., Suenaga, K., and Iijima, S., 2008, "Smallest Carbon Nanotube Assigned with Atomic Resolution Accuracy," Nano Letters, **8**(2).

[136] Sader, J. E., Chon, J. W. M., and Mulvaney, P., 1999, "Calibration of Rectangular Atomic Force Microscope Cantilevers," Review of Scientific Instruments, **70**(10).

[137] Sader, J. E., 1998, "Frequency Response of Cantilever Beams Immersed in Viscous Fluids with Applications to the Atomic Force Microscope," Journal of Applied Physics, **84**(1).

[138] Shabana, A., 2001, "Computational Dynamics," John Wiley & Sons, Inc., New York, N.Y.

[139] Fabien, B., 2009, "Analytical System Dynamics, Modeling and Simulation," Springer, New York, N.Y.

[140] Saggere, L., and Kota, S., 2001, "Synthesis of Planar, Compliant Four-Bar Mechanisms for Compliant-Segment Motion Generation," Journal of Mechanical Design, Transactions of the ASME, **123**(4).

[141] Diaz, R. A., Herrera, W. J., and Martinez, R., 2006, "Moments of Inertia for Solids of Revolution and Variational Methods," European Journal of Physics, **27**(2).

[142] Royston, T. J., 2008, "Leveraging the Equivalence of Hysteresis Models from Different Fields for Analysis and Numerical Simulation of Jointed Structures," Journal of Computational and Nonlinear Dynamics, **3**(3).

Christopher Andrew Pelzmann

RESEARCH INTERESTS

- Mechanics of and tools for micro/nano-manufacturing
- fundamental study of robotic grasps in the presence of nano-scale forces
- design and fabrication of chip-scale manipulators
- construction of complex three-dimensional micro-/nano-scale structures and mechanisms

EDUCATION

- Ph.D., Mechanical Engineering, University of Illinois at Chicago, Summer 2012
    - Dissertation: "Contact-Based Assembly of Nano-scale Structures: Synthesis of Mechanics and Tools of Nanomanipulation"
    - Advisor: Dr. Laxman Saggere
- B.S., Mechanical Engineering, University of Colorado at Boulder, 2006
- B.S. (pursued), Engineering Physics, University of Northern Colorado, 2001-2002

AWARDS AND HONORS

- **First Prize**, ASME Society Wide Micro/Nano Forum Poster Competition held during the International Mechanical Engineering Congress and Exposition (IMECE), 2011, Denver, CO.
- **Student Travel Grant**, given by the National Science Foundation to attend the ASME Society Wide Micro/Nano Forum held during the International Mechanical Engineering Congress and Exposition (IMECE), 2011, Denver, CO.
- **Best Paper Award**, 3rd International Conference on Micro- and Nano-systems, at the ASME International Design Engineering and Technical Conferences (IDETC), 2009, San Diego, CA.
- **Chancellor's Student Service Award**, 2011, in recognition of outstanding volunteer service to the University of Illinois at Chicago
- **Department Scholar Award**, 2002, in recognition of outstanding scholarly activity in the Physics Department of the University of Northern Colorado.

PUBLICATIONS

Conference Publications

1. Krishnan, S., Pelzmann, C.A., and Saggere, L., "Design and development of a chipscale multifingered micromanipulator system for coordinated microassembly," Proc. *ASME 3rd International Conference on Micro- and Nanosystems*, San Diego, CA, Aug. 30 – Sept. 2, 2009, 10 pages **(Peer-reviewed). Received Best Paper Award.**
2. Pelzmann, C.A., and Saggere, L., "Measurement and characterization of stiction force in microstructures with tapered features," Proc. *ASME 5th International Conference on Micro- and Nanosystems*, Washington, D.C., Aug. 28 – 31, 2011, 10 pages **(Peer-reviewed).**
3. Pelzmann, C.A., and Saggere, L., "Microassembly via coordinated manipulation of objects using a multifingered micromanipulator," Proc. *ASME International Mechanical Engineering Congress and Exposition*, Denver, CO, Nov. 11-17, 2011, 15 pages **(Peer-reviewed).**
4. Pelzmann, C.A., Krishnan, S., and Saggere, L., "Development and operation of the Chipscale Multifingered Micromanipulator system for coordinated microassembly," Transactions on Mechatronics **(In preparation).**

5. Pelzmann, C.A., and Saggere, L., “Observation and measurement of compliant nano-scale structures under static mechanical load,” Nano Letters **(In preparation).**

LEADERSHIP ACTIVITIES

- President, MIE Department Graduate Student Association (2009-2011)
    - Gained official university recognition of the group
    - Composed the group’s official constitution
    - Organized and lead outreach activities to local high school
- Department Representative, UIC Graduate Student Council (2009-2011)
- Member, MIE Department Graduate Student Association (2008-2011)

PROFESSIONAL EXPERIENCE

RESEARCH ENGINEER **2012 – present**
Escape Dynamics, Inc., Broomfield, CO
Escape Dynamics designs, manufactures, and builds advanced aerospace propulsion and infrastructure systems in pursuit of opening space for large scale commercial, social, and scientific exploration

RESEARCH ASSISTANT **2009 – 2012**
Microsystems & Devices Laboratory at UIC, Chicago, IL
The Microsystems & Devices Lab specialized in contact-based micro-/nano-manufacturing research and mechanically inspired biomedical systems

- Conceptualized, designed, modeled, constructed, and tested various systems for investigating methods of manufacturing structures and mechanisms from micro-/nano-scale components
- Worked on macro-scale and chip-scale robotic systems in both ambient and controlled environments
- Studied the kinematic and dynamic behavior of multibody robotic systems for contact-based manipulation techniques in the presence of micro-/nano-scale forces

ENGINEERING CONSULTANT **2006 – 2009**
Arete Personified LLC, Westminster, CO – Chicago, IL
Arete Personified was a consulting company offering engineering services to multiple companies in the Denver and Chicago metro areas

MECHANICAL ENGINEER **2006 – 2006**
Aktiv-Dry LLC, Boulder, CO
Aktiv-Dry is a research and design company transferring biomedical technology from academia to the marketplace

LAB ASSISTANT **2005 – 2006**
Electronics Center, Integrated Teaching and Learning Lab, University of Colorado, Boulder, CO
The Electronics Center is a hands-on circuit design and fabrication center for the University of Colorado at Boulder’s Integrated Teaching and Learning Laboratory (ITLL).

TEACHING ASSISTANT **2004 – 2004**
University of Colorado, College of Engineering, Boulder, CO
Undergraduate teaching assistant for freshman course in engineering projects